Transverse-electric surface plasmon polaritons in homogeneous and periodic graphene systems

Zeeshan Ahmad

A thesis presented for the degree of
Doctor of Philosophy

School of Physics and Astronomy
Cardiff University
United Kingdom
December 2022

Summary

Metamaterials making use of conductors have been shown to manipulate light in ways difficult for dielectric photonic devices, owing to the dispersive conductivity response. For example, light can be "sqeezed" through subwavelength metallic apertures, which is not possible for a dielectric aperture. This allows optical metamaterial devices to be augmented by plasmon polariton devices, increasing their capability whilst minimising design complications. One particular subject matter of interest is the existence of surface plasmon polariton (SPP) in the transverse electric (TE) polarisation in graphene. The terahertz frequency range of this mode makes this mode a suitable candidate for devices operating in the infrared frequencies. The contribution of this thesis is that of showing that the TE SPP electromagnetic modes can exist outside the earlier reported range of frequency of $1.667 < \hbar\omega/\mu < 2$, where μ is the chemical potential, in graphene. We find that these electromagnetic modes may have either evanescent or exponentially growing field profile perpendicular to graphene, depending on the mode frequency. The dispersion of these TE SPP modes lies below the light cone, not allowing resonant excitation, meaning that an incident beam of light in a dielectric can not have the frequency and wavenumber matching that of the TE modes. We propose a graphene grating, in which TE SPPs can produce sharp and prominent transmission spectra resonances, showing that excitation is possible. The position of the sharp features can be tuned for desired frequency and in-plane wavenumber, by choosing the chemical potential, temperature, and period of the grating. Thus the TE SPP mode in graphene is a prospective for optical devices that would benefit from the tunability, high in-plane velocity, and terahertz frequency range of the mode.

Acknowledgements

I would like to express immense gratitude and appreciation to both my PhD supervisor Dr. Sang Soon Oh and co-supervisor Dr. Egor A. Muljarov for their continuous guidance, encouragement and support during my journey through this PhD project. I particularly appreciate Dr. Sang Soon Oh to extend to me the offer to be a PhD student in the Sêr Cymru group at Cardiff University. I would also like to say thank you to Stephan Wong, Ghada Alharbi, Haedong Park, Joe Mahoney, Ananya Ghatak, Reza Hekmati, Sam Bishop, Dhafer Alshahrani and Yongkang Gong for their useful support and feedback. Finally, I am grateful for my father, mother, sister and brother for their encouragement, support and patience toward me as a PhD student.

I would like to acknowledge and am thankful for the financial support of EPSRC under the DTP scheme.

Publications

Papers

1. Z. Ahmad, E. A. Muljarov, and S. S. Oh, "*Extended frequency range of transverse-electric surface plasmon polaritons in graphene*", **Phys. Rev. B** 104, 085426 (2021)
2. Z. Ahmad, S. S. Oh, and E. A. Muljarov, "*Tuning transverse electric surface plasmon polaritons in periodically modulated graphene*", **(will be submitted)**

Presentations

1. **(oral)** Z. Ahmad, E. A. Muljarov, and S. S. Oh, "Effects of electronic interband transition on Transverse-electric transmission in graphene grating", Cardiff University Physics Chat, 1 December 2022, Cardiff, UK
2. **(poster)** Z. Ahmad, E. A. Muljarov, and S. S. Oh, "Transverse-electric surface plasmon modes in graphene grating", META Conference on Metamaterials, Photonic Crystals and Plasmonics, 20 July 2022, Torremolinos, Spain
3. **(poster)** Z. Ahmad, E. A. Muljarov, and S. S. Oh, "Transverse-electric transmission through graphene grating", Cardiff University ECR Annual Poster Competition, 28 June 2022, Cardiff, UK
4. **(oral)** Z. Ahmad, E. A. Muljarov, and S. S. Oh, "Complex frequency analysis of Transverse electric surface plasmon polariton modes in periodic graphene-based structures", Semiconductor and Integrated Opto-electronics (SIOE) Conference, 12 April 2022, Cardiff, UK
5. **(oral)** Z. Ahmad, E. A. Muljarov, and S. S. Oh, "Complex frequency surface plasmon modes in graphene", Cardiff University Postgraduate Conference, 7 April 2021, Cardiff, UK

6. **(oral)** Z. Ahmad, E. A. Muljarov, and S. S. Oh, “Surface Plasmon Polariton modes in thin metallic films and graphene”, Cardiff University Physics Chat, 9 October 2020, Cardiff, UK
7. **(oral)** Z. Ahmad, E. A. Muljarov, and S. S. Oh, “Surface plasmon modes in thin metallic films and graphene”, Theory Seminar, 6 February 2020, Cardiff, UK

Contents

List of Figures

CHAPTER 1

Introduction

1.1 Photonics and Plasmonics

In the fields of photonics and plasmonics, the typical aim is to control the flow of light [1, 2], as desired, by means of employing appropriately designed devices. The research on plasmonics in graphene structures that will be presented in this thesis is related closely to the field of photonic devices, as devices employing the use of surface plasmons may be thought of as a subset of photonics. The main difference is that plasmonic modes are a coupling of electromagnetic solutions and charge carrier oscillations, whereas photonic modes exist without the charge carrier oscillations. Both of the fields typically feature crystal devices periodic in space namely photonic crystals [3–7] or plasmonic crystals [8–10]. It is thus imperative to start our discussion with the advent of photonics and photonic crystals, and then build upon their introduction with plasmonic aspects, leading to the aims of the thesis in Sec. 1.2.1.

1.1.1 Emergence of photonic crystals

We human beings aim to build devices that make our lives easier. Almost every person knows that electronic devices involving electronic circuits have been a key part of our advancement. As scientists look towards new fronts for development, photonic and plasmonic devices offer more flexibility in design and speed of communication [11–13] than their electronic counterparts [14]. For example, optical fibre interconnects between transistors can transfer digital information more than 1000 times faster than electronic interconnects [14]. Another example is the potential use of neuromorphic photonic processors allowing greater bandwidth than current neuromorphic electronics [15]. It is therefore important for us to be able to effectively control the flow and inherent properties of light within such devices.

Photonic crystals, periodic dielectrics [16], emerged when Yablonovitch [17] demonstrated semiconductor band structures to be analogous to photonic band structures, thus taking inspiration from naturally occurring periodic electric potentials, applying to structures with periodic permittivity [17, 18]. Specifically, there was a possibility of "photonic band gaps" analogous to the one in semiconductors, forbidding electromagnetic modes for a particular range of frequency (energy). This not only involves energy carriers of the mode (photons) having no mass, and thus moving much faster than electronics, but also provides us with the flexibility of structural tuning, so long as the structural features are of the order of the light wavelength [19]. Yablonovitch later also demonstrated a three-dimensional photonic crystal exhibiting a full photonic band gap [20]. Thus electromagnetic theory based on Maxwell's equations was developed to cater to the calculation of photonic modes [21, 22].

Photonic crystals have proven to be a useful avenue of research recently for devices that provide control over optics such as waveguide splitter, narrow-band filters, and polarisers [23, 24].

1.1.2 Plasmonic structures

The permittivity gains an optical frequency dependence when some dielectrics in these systems are replaced by conductors, with the frequency dependence coming from temporal non-locality of the conductivity. Physically, the optical modes couple to the charge oscillation waves in the conductor and a plasmonic dispersion emerges [25]. The frequency dependence of permittivity of the system, albeit computationally more tedious to deal with than a photonic system, provides the ability to confine light to subwavelength distances [26, 27]. That is, the wavelength of the surface plasmonic modes can be much smaller than the cavities or apertures in structures hosting the modes [28].

A hallmark demonstration of subwavelength confinement was given by Ebbesen [29], where an "extraordinary" transmission was observed through subwavelength structures. The "wavenumber" (inverse of size) of the holes that allow light to pass through is certainly larger than that of the incoming beam. It is the coupling to the charge carriers along the holes in metallic material that enabled light to squeeze through. Pendry referred to this phenomenon as light playing Houdini [19].

1.1.3 Excitation of propagating surface plasmon polaritons

To be able to make use of the modes we have discussed, we need to consider how these modes can experimentally come into being, in order to be used within plasmonic devices and then harnessed back into optical circuits, in a controlled manner, as needed. In fact, in 1902 surface plasmons were unintentionally already excited by Wood [30] in diffraction gratings of conducting materials, where he experienced the effects of plasmons as anomalous lines in the spectrum produced by passing incandescent light through the gratings. It turns out that the problem of "converting" a free light wave to surface plasmons is a matter of matching part of the dispersion of free light to surface plasmon dispersion. Since the dispersion of surface plasmon modes is below the light line of adjacent dielectric, we must alter the light line to shift down (increase wavenumber along surface $k_{\parallel}$) by changing materials around the conductor. Practically, we choose a frequency ω of the surface plasmon mode that we would like to excite on a conducting surface, and then make sure that the wavenumber of the exciting light wave along the surface $k_{||}$ is the same as in the surface plasmon dispersion [31]. This is called wavenumber matching.

Dielectric gratings can be used as couplers [31] to surface plasmons as they can alter $k_{||}$ next to conducting surfaces. Furthermore, attenuated total reflection (ATR) couplers [32] can also excite surface plasmons. The structure usually consists of a high-refractive index material, in where light is incident toward a metal placed immediately next to it, of a certain thickness. The sought after surface plasmon mode is then excited on the surface of metal that is not adjacent to the high-refractive index material. Another way for exciting surface plasmons is the use of Otto-Kretschmann configuration [33] by the means of frustrated total internal reflection. That is, an evanescent wave produced by total internal reflection due to light incident toward a lower refractive index surface, can excite a surface plasmon in a nearby metallic surface.

Devices that make use of propagating surface plasmon polaritons are designed so that these modes are eigenmodes of the system. And evidence of resulting surface plasmon resonance can be found by examination of transmission [34, 35] and reflection spectra [36]. It is obvious that when electrons respond to incoming oscillations in the electric field, some energies of input beam must be passed on to the electrons.

1.2 Graphene as a platform for propagating surface plasmon polaritons

Graphene has been a popular 2D material with electronic properties that certainly attracts the field of plasmonics. It usually occurs in graphite which is sliding layers of graphene held together by van der Waal forces. In 2004, Geim and Novoselov were first able to experimentally isolate a single graphene layer earning them a Nobel prize in 2010 [37]. This discovery made possible the implementation of devices that were theorised to utilise the motion of electrons as massless particles moving at approximately $10^6\,\mathrm{ms}^{-1}$ [38] in graphene. Graphene is certainly an insightful conductor for the investigation of surface plasmons due to its linear electronic dispersion [39–43] and lack of density of states at the K-point. Graphene is known for its tunability of optical conductivity by application of suitable gate voltage [44], inducing sufficiently low but finite chemical potential. Devices like optical modulators [45], polarisers [46] and absorption enhancement devices benefit from this tunability. Surface plasmons in graphene would be important for practical applications such as waveguide polarisers [47] and graphene plasmonic waveguides which can be useful for photonic integrated circuits[48].

1.2.1 Research on transverse electric surface plasmon polaritons in graphene

In the area of propagating surface modes, there are two polarisations, transverse magnetic (TM) and transverse electric (TE) which are independent surface solutions to Maxwell's equations. TM SPPs, generally found in noble metals [49] are well confined. That is, the electromagnetic fields for the said modes are decaying fast as we move away from interface. The TM mode requires the imaginary part of conductivity of the material to be positive. On the other hand the TE mode exists in materials for which the imaginary part of the surface conductivity [50] can be negative, for example graphene. The negative imaginary part constitutes a necessary condition for TE mode. It involves in-plane electric field oscillations, and corresponding current density oscillations, both that are perpendicular to surface mode propagation direction, unlike TM mode. However, the charge density is neutral. TE mode is less confined in graphene due to small value of fine-structure constant being a factor in the optical conductivity of graphene. Although high confinement favours TM SPPs for plasmonic devices, note that the frequency of the TE mode is in the midinfrared and terahertz range in graphene, and not bounded by plasma frequency (effective in the case of graphene) like TM SPPs. Despite efforts made to increase SPP confinement in graphene based plasmonic structures [51], the lack of confinement can also be useful for other devices, where a higher sensitivity to the refractive index of surrounding dielectrics [52] could be utilised. Structures for excitation and the detection of TE mode in graphene have already been proposed [53–55]. It is the aim of this thesis to provide clarification regarding the qualitative features of complex frequency dispersion of TE mode in homogeneous and one-dimensionally periodic graphene. This provides a starting platform for plasmonic devices [56] intending to utilise tunable TE mode in graphene.

1.3 Thesis outline

Ch. 2 gives a theoretical background containing the use of Maxwell's equations and complex frequency formalism used to acquire surface plasmon dispersion. Ch. 3 provides a discussion on surface plasmons on conducting surfaces. Ch. 4 aims to provide us with an expression for graphene conductivity, and discusses key details of the conductivity spectrum of graphene in preparation for later chapters where graphene-based structures are considered. Ch. 5 provides an analysis of the surface plasmon modes that can be found in a homogeneous infinite sheet of graphene, and how the frequency range of the TE polarisation of the mode is extended when we consider frequency to have an imaginary part and allow non-zero temperatures. Ch. 6 extends the analysis to one-dimensional graphene grating. Ch. 7 concludes the thesis and presents possible future investigations.

CHAPTER 2

Electrodynamics of bounded media and materials

Propagating SPPs are eigenmodes of the interface between two materials with permittivity of opposite signs, e.g. a conductor and a dielectric [31, 57]. This interesting phenomenon that confines light to interfaces can be used for applications with tunability. There is potential in investigating SPPs in graphene [58] and other 2D materials [59] as they can be doped or gated with voltage to tune the Fermi-level thus impacting their conductivity spectrum. Investigation of surface plasmons in any system is an electromagnetic problem, and the equations that govern such problems are the Maxwell's equations. The matter equations are written in Sec. 2.1.

So this chapter will introduce fundamental formalisms and concepts involving Maxwell's equations required to perform analysis on surface plasmon modes.

As the name implies, surface plasmons are modes that are found at "surfaces", or interfaces between different materials. Here we will establish the relevant definitions to tackle electromagnetic field solutions at interfaces.

2.1 Maxwell’s equations

Surface plasmon polaritons are electromagnetic modes and to deal with them we must introduce Maxwell’s equations which govern electric and magnetic fields. In differential formulation, in Gaussian units, they are [60, 61]

$$\nabla \times \mathbf{E} = -\frac{1}{c}\partial_t \mathbf{H}, \qquad \text{(Faraday's law)} \tag{2.1}$$

$$\nabla \times \mathbf{H} = \frac{4\pi}{c}\mathbf{J} + \frac{1}{c}\partial_t(\varepsilon \mathbf{E}), \qquad \text{(Ampère 's law)} \tag{2.2}$$

$$\nabla \cdot (\varepsilon \mathbf{E}) = 4\pi\rho, \qquad \text{(Gauss's law)} \tag{2.3}$$

$$\nabla \cdot \mathbf{H} = 0, \qquad \text{(Gauss's magnetism law)} \tag{2.4}$$

where $\mathbf{E}$ is the electric field, $\mathbf{H}$ is the magnetic field, c is the speed of light in vacuum, t is time, $\nabla\times$ is the curl operator, ε is permittivity, $\nabla\cdot$ is the divergence operator, and magnetic permeability is 1. The quantities $\mathbf{J}$ and ρ are free current and charge densities, respectively.

Eqs. (2.1)–(2.4) are differential equations with the quantities $\mathbf{E}, \mathbf{H}, \mathbf{J}, \rho$ being functions of a point in space $\mathbf{r}$ and time t, and so we will discuss their meaning at a point in space and time. In 1826, Ampère published a theoretical summary of his experiments including the interaction between electric fields and magnets [62]. The law named after him, in its modern form Eq. (2.2), means that a flow of charges through a point, or a change in the electric field induces a magnetic flux around the point. Similarly, Faraday’s law Eq. (2.1) means that a change in the magnetic flux at a point induces an electric field around that point, describing the phenomenon of electromagnetic induction discovered by Faraday in 1831 [62]. We use the word “around” instead of “at” since we are taking curl of a continuous vector field, indicating a local rotation. The remaining two Eqs. (2.3) and (2.4) describe the relation of charges to electromagnetic fields. According to the differential form of Gauss’s law in Eq. (2.3), an existence of an electric charge at a point corresponds to a “source” or a “sink” in the electric field. A magnetic field on the other hand cannot have any sources or sinks due to the fact that there can be no magnetic charges, at least not that we know of [63, 64]. When we break a magnet half-way between its north and south poles, we get two smaller magnets each with their respective poles, instead of a magnetic monopole.

For materials linearly susceptible to electric polarisation, one conventionally uses the electric displacement field,

$$\mathbf{D} \equiv \varepsilon \mathbf{E} \equiv (1 + 4\pi\chi_e)\mathbf{E} = \mathbf{E} + 4\pi\mathbf{P}, \tag{2.5}$$

where

$$\mathbf{P} \equiv \chi_e \mathbf{E} \tag{2.6}$$

is the polarisation density, and χ_e is electric susceptibility [60, 61]. We aim to obtain eigensolutions to electromagnetic systems in terms of the **E** and **H** electromagnetic field strengths.

2.2 Permittivity and conductivity: material response functions

Surface plasmons are modes where electromagnetic fields interact with the charge carriers, electrons, in the conductor materials of the structure. It is important to identify the terms that describe this interaction in Maxwell's equations. Whilst **H** and **E** fields describe the electromagnetic participants, we identify the current density **J** and electric displacement field **D** as description of the dynamics of electrons.

Eq. (2.5) is a constitutive equation that describes the effect of an applied electric field **E** on the charge carriers that respond to it, in doing so, displacing the electric field into **D**. The coefficient ε, the permittivity of the material, is then a response function between the input **E** and response **D**. In fact, ε, χ_e and σ are all response functions that are related to each other. We thus identify permittivity, a characteristic coefficient of the material, as a response function to an electric field

E, producing an electric displacement field **D** [65],

$$\mathbf{D}(\mathbf{r},t) = \int_{-\infty}^{\infty}\int_{-\infty}^{\infty} \varepsilon(\mathbf{r}-\mathbf{r}',t-t')\,\mathbf{E}(\mathbf{r}',t')\,dt'd\mathbf{r}'. \tag{2.7}$$

The response at $(\mathbf{r},t)$ is therefore a weighted accumulation of **E** spanning space and time (using integrals over $\mathbf{r}'$ and t'), meaning that **E** at $(\mathbf{r}',t')$ contributes to **D** at $(\mathbf{r},t)$. Note that the spatial and temporal dependence of permittivity ε is translationally invariant in position and time, in homogeneous systems,

$$\varepsilon(\mathbf{r},\mathbf{r}',t,t') = \varepsilon(\mathbf{r}-\mathbf{r}',t-t'), \tag{2.8}$$

so that by Fourier transforming, we obtain,

$$\mathbf{D}(\mathbf{k},\omega) = \varepsilon(\mathbf{k},\omega)\mathbf{E}(\mathbf{k},\omega), \tag{2.9}$$

where the dependence on the wavenumber **k**, and frequency ω is emphasised.

Now we wish to elaborate how the conductivity is linked to Maxwell's equations. In the most straightforward approach, we can use the constitutive equation Eq. (2.9), together with the time-Fourier transform of Ampère's law Eq. (2.2) to get,

$$\begin{aligned} \nabla\times\mathbf{H} &= \frac{4\pi}{c}\mathbf{J} + \frac{1}{c}(-i\omega)\mathbf{E}, & (2.10)\\ &= \frac{1}{c}[4\pi\sigma + (-i\omega)]\mathbf{E}. & (2.11)\end{aligned}$$

It is convenient to use the conventional constitutive equation Eq. (2.5) together with Ampère's law as in Eq. (2.2), so that the conductivity is part of the polarisation density **P**. The connection between χ_e and σ can be seen by imposing that there is no free current since the conductivity effects are accounted for in the polarisation current,

$$\mathbf{J} = 0. \tag{2.12}$$

Surface plasmon modes are plane electromagnetic waves of the form (we can always Fourier expand a general solution)

$$e^{i\mathbf{k}\cdot\mathbf{r}-i\omega t}, \tag{2.13}$$

where **r** is three-dimensional position in space and **k** is three-dimensional wavenumber. By assuming time-invariance of χ_e, we obtain the permittivity in terms of conductivity,

$$\varepsilon(\mathbf{k},\omega) \equiv 1 + 4\pi\chi_e = 1 + \frac{4\pi i\sigma(\mathbf{k},\omega)}{\omega}. \tag{2.14}$$

We aim to define our structures of various materials by defining ε as piecewise functions of spatial coordinates.

2.3 Polarisation relative to planar interfaces

As we will deal with modes that occur at interfaces between different media, we can use the orientation of the surface to formalise a convention to obtain solutions of such systems. It turns out that the plane-wave solution can be broken down into two parts according to their orientation relative to a chosen interface. These parts are conventionally known as the transverse magnetic (TM) or transverse electric (TE) polarisations. The component normal to the interface of the magnetic field **H** (electric field **E**) is zero in the TM (TE) polarisation [66]. We will make use of this convention because it makes solution finding easier and organized. Throughout this work, relevant interfaces will be oriented parallel to the xy-plane in the Cartesian coordinate system so that the normal to interfaces will be the z direction, and propagation of mode along interface will be along x direction, unless otherwise stated.

Fig. 2.1 shows both polarisations relative to an interface between two media,

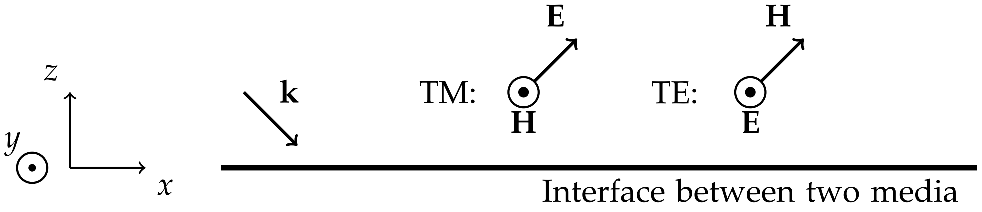

Figure 2.1: Depiction of TM and TE polarisations of **E** and **H** fields for an arbitrary wavenumber direction given by **k**, oriented relative to an interface (horizontal solid line) between two media.

with the following nonzero field components emerging for each polarisation,

$$\begin{pmatrix} E_x \\ H_y \\ E_z \end{pmatrix} : \text{TM} \qquad \begin{pmatrix} H_x \\ E_y \\ H_z \end{pmatrix} : \text{TE} \tag{2.15}$$

The decomposition of solutions to Maxwell's equations into TM and TE polarisations should be easy to see when we decompose the **E**, **H** fields into components parallel and perpendicular to the interface, that is,

$$\mathbf{E} = \mathbf{E}_{\|} + \mathbf{E}_{\perp} \quad \text{and} \quad \mathbf{H} = \mathbf{H}_{\|} + \mathbf{H}_{\perp}. \tag{2.16}$$

Due to propagation phasor dependence of a general electromagnetic solution $e^{i\mathbf{k}\cdot\mathbf{r}}$, where **r** and **k** are three-dimensional vectors, we may make the substitution $\nabla\times \rightarrow i\mathbf{k}\times$ in Eqs. (2.1) and (2.2) to get

$$i\mathbf{k} \times \mathbf{E} = -\frac{1}{c}\partial_t \mathbf{H}, \tag{2.17}$$

$$i\mathbf{k} \times \mathbf{H} = \frac{1}{c}\partial_t[\varepsilon \mathbf{E}]. \tag{2.18}$$

Assuming monochromatic waves and finding dot and cross product of Eqs. (2.17) and (2.18) with $\hat{\mathbf{n}}$ leads to

$$\hat{\mathbf{n}} \cdot i\mathbf{k} \times \mathbf{E}_{||} = -\frac{1}{c}\partial_t \hat{\mathbf{n}} \cdot \mathbf{H}_{\perp}, \tag{2.19}$$

$$\hat{\mathbf{n}} \times (i\mathbf{k} \times \mathbf{E}) = -\frac{1}{c}\partial_t[\hat{\mathbf{n}} \times \mathbf{H}_{||}], \tag{2.20}$$

$$\hat{\mathbf{n}} \cdot i\mathbf{k} \times \mathbf{H}_{||} = \frac{1}{c}\partial_t[\varepsilon \hat{\mathbf{n}} \cdot \mathbf{E}_{\perp}], \tag{2.21}$$

$$\hat{\mathbf{n}} \times (i\mathbf{k} \times \mathbf{H}) = \frac{1}{c}\partial_t[\varepsilon \hat{\mathbf{n}} \times \mathbf{E}_{||}], \tag{2.22}$$

where $\hat{\mathbf{n}}$ is the unit vector normal to interface. We find that Eq. (2.19) and Eq. (2.22) can be solved independently for $\mathbf{H}$ and $\mathbf{E}_{||}$ regardless of the value of $\mathbf{E}_{\perp}$ forming TE solutions. Similarly, the TM solutions are found using Eqs. (2.20) and (2.21).

2.4 Boundary conditions at an interface

The Maxwell's equations, Eqs. (2.1)–(2.4), in their differential form are made to hold true for electromagnetic fields in continuous media, meaning that material properties like permittivity and permeability that are usually found in constitutive relations, are continuous functions in space. This can be intuitively seen by considering the fact that the differential operators in the equations require continuity of electromagnetic fields. Practically, however, we must deal with discontinuities in material properties across space, at macroscopic levels. The way we deal with this conundrum is quite simple. We simply integrate the differential equations for a chosen infinitesimal volume or area in space. The area or volume is typically chosen to be across interfaces that produce discontinuities, providing us with boundary conditions. We integrate Eqs. (2.1)–(2.4) to find,

$$\oint_{\partial\mathcal{A}} \mathbf{E}\cdot d\mathbf{l} = -\frac{1}{c}\iint_{\mathcal{A}} \partial_t \mathbf{H}\cdot d\mathbf{A}, \tag{2.23}$$

$$\oint_{\partial\mathcal{A}} \mathbf{H}\cdot d\mathbf{l} = \frac{1}{c}\iint_{\mathcal{A}} (4\pi\mathbf{J} + \partial_t[\varepsilon\mathbf{E}])\cdot d\mathbf{A}, \tag{2.24}$$

$$\oiint_{\partial\mathcal{V}} \varepsilon\mathbf{E}\cdot d\mathbf{A} = \iiint_{\mathcal{V}} 4\pi\rho\, dV, \tag{2.25}$$

$$\oiint_{\partial\mathcal{V}} \mathbf{H}\cdot d\mathbf{A} = 0. \tag{2.26}$$

Please be reminded that by defining interfaces in forthcoming structures using permittivity (instead of conductivity), we are choosing $\mathbf{J} = 0$. We have made use of Stoke's theorem [67],

$$\iint_{\mathcal{A}} \nabla \times \mathbf{F} \cdot d\mathbf{A} = \oint_{\partial\mathcal{A}} \mathbf{F} \cdot d\mathbf{l}, \tag{2.27}$$

for a smooth vector field $\mathbf{F}$, a bounded surface $\mathcal{A}$ with boundary $\partial\mathcal{A}$ to get Eqs. (2.23) and (2.24), and also made use of Gauss's theorem [67],

$$\iiint_{\mathcal{V}} \nabla \cdot \mathbf{F} dV = \oiint_{\partial\mathcal{V}} \mathbf{F} \cdot d\mathbf{A}, \tag{2.28}$$

for a bounded solid region $\mathcal{V}$ with bounding area $\partial\mathcal{V}$ to get Eqs. (2.25) and (2.26).

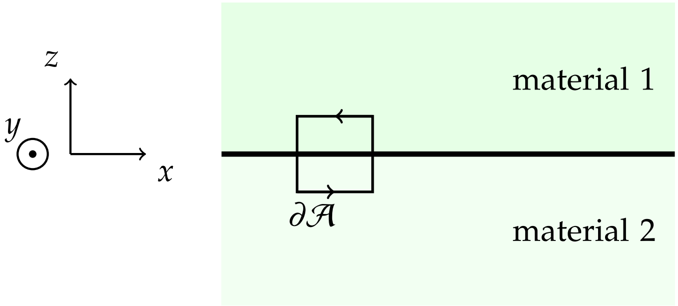

Figure 2.2: Interface between two materials with a loop crossing the interface at $z = 0$. The boundary of the loop is $\partial\mathcal{A}$, and its enclosed area is $\mathcal{A}$.

In general, for an interface between two materials 1 and 2 as shown in Fig. 2.2, we find by using Eqs. (2.23) and (2.24) on the loop bounded by $\partial\mathcal{A}$ with shrinking height along z so that $\mathcal{A}$ is infinitesimal, that [61],

$$\hat{\mathbf{n}}_{12} \times (\mathbf{E}_2 - \mathbf{E}_1) = 0, \tag{2.29}$$

$$\hat{\mathbf{n}}_{12} \times (\mathbf{H}_2 - \mathbf{H}_1) = c\mathbf{K}_f, \tag{2.30}$$

where $\hat{\mathbf{n}}_{12}$ is the normal vector pointing away from medium 1, and $\mathbf{K}$ is the free surface current. Eqs. (2.29) and (2.30) apply to both TM and TE polarisations. That is, the tangential component of $\mathbf{E}$ is continuous, and $\mathbf{H}$ differs by $\mathbf{K}_f$, across the interface. Note that when we move to structures with infinitesimally thin conductors, the current is a surface current $\mathbf{K}_f$ that is physically the response via conductivity, i.e. $\mathbf{K}_f = \sigma_{\text{surf}}\mathbf{E}$ where σ_{surf} is surface conductivity. However, again we can absorb the effect of this conductivity into the permittivity of the overall structure with the use of Dirac delta function $\delta(z)$ which satisfies the property [68],

$$\int_{-\infty}^{\infty} \delta(z)\, dz = 1. \tag{2.31}$$

2.5 Poynting vector for measurement

The Poynting vector of an electromagnetic mode is [61]

$$\mathbf{S} = \frac{c}{4\pi}\mathbf{E} \times \mathbf{H}, \tag{2.32}$$

describing the energy flux. We may thus calculate the flow of energy across an interface of an incident plane wave. It turns out that the component of $\mathbf{S}$ across the interface is proportional to $c|E|^2$, which will be used to discuss transmission spectra in Chs. 5 and 6.

2.6 Example with two semi-infinite dielectrics

We provide an example of solving Maxwell's equations for two non-dispersive dielectric materials separated by a planar interface (see Fig. 2.3). This serves as a simplified (compared to dispersive structures) demonstration of the boundary conditions, obtaining of secular equations for the modes and in general formalising a process for electromagnetic mode analysis. It will also serve to help us to concretely understand the challenge in exciting surface plasmon modes mentioned in Sec. 1.1.3. In a uniform non-dispersive dielectric material of constant permittivity, the dispersion of light, easily obtained from Maxwell's equations, is linear,

$$\omega = \frac{c}{\sqrt{\varepsilon_j}}|\mathbf{k}_j| \tag{2.33}$$

where c is the speed of light in vacuum, ε is the permittivity of the dielectric material, $\mathbf{k}$ is the wavenumber.

Figure 2.3: Interface between two semi-infinite dielectric materials.

Now consider the simple setup of an interface between two dielectrics that is shown in Fig. 2.3, with permittivities $\varepsilon_1 \neq \varepsilon_2$, with $k_y = 0$,

$$\varepsilon(z) = \begin{cases} \varepsilon_1 & z > 0, \\ \varepsilon_2 & z < 0. \end{cases} \tag{2.34}$$

We can start with the Maxwell's equations - specifically Ampère 's Law and Faraday's Law - to observe that the solution of the electric (and magnetic) fields is a combination of plane wave with ω and $\mathbf{k}$. The solution is characterised by the frequency ω, and the wavenumber $\mathbf{k}$. Therefore we have the ansatz

$$H_y = e^{iqx} \times \begin{cases} Ae^{ik_1 z} + Be^{-ik_1 z} & z > 0, \\ Ce^{ik_2 z} + De^{-ik_2 z} & z < 0, \end{cases} \tag{2.35}$$

for magnetic field, in the TM polarisation, defined above and below the interface at $z = 0$, where q is the component of wavenumber $\mathbf{k}$ in x direction, k is component of wavenumber $\mathbf{k}$ along y direction, the number in the subscript refers to the medium above or below the interface, and

$$k_n = \sqrt{\varepsilon_n \omega^2/c^2 - q^2} \tag{2.36}$$

follows from Eq. (2.33). The E_x field can then be found by substituting Eq. (2.35) into Eq. (2.2) as

$$E_x = \frac{c}{\omega} e^{iqx} \times \begin{cases} \frac{k_1}{\varepsilon_1}\left[Ae^{ik_1 z} - Be^{-ik_1 z}\right] & z > 0, \\ \frac{k_2}{\varepsilon_2}\left[Ce^{ik_2 z} - De^{-ik_2 z}\right] & z < 0. \end{cases} \tag{2.37}$$

The continuity conditions Eqs. (2.29) and (2.30) imply that Eqs. (2.35) and (2.37) are continuous across the interface as $\mathbf{K}_f = 0$ (no surface current density) giving

$$A + B = C + D, \tag{2.38}$$

$$\frac{k_1}{\varepsilon_1}(A - B) = \frac{k_2}{\varepsilon_2}(C - D). \tag{2.39}$$

For outgoing boundary conditions and vanishing field $H_y(|z| \to \infty) = 0$ far away from the interface, we get $A = D = 0$, and along with Eqs. (2.38) and (2.39), this yields the dispersion relation [31]

$$\varepsilon_1 k_2 + \varepsilon_2 k_1 = 0. \tag{2.40}$$

From Eqs. (2.40) and (2.36) we obtain

$$\omega = c\sqrt{\frac{1}{\varepsilon_1} + \frac{1}{\varepsilon_2}}\, q, \tag{2.41}$$

which is the dispersion of light for the given mode. This dispersion is linear, and additionally, light propagates into both dielectrics from the interface (see Fig. 2.4).

The permittivities of the two materials can be chosen, for example, as $\varepsilon_1 = 2$, $\varepsilon_2 = 4$ simulating the dispersion in Fig. 2.4. For dielectrics, Eq. (2.40) implies that $k_1 k_2 < 0$.

As shown in Fig. 2.4, by plotting the electric field profile at $\omega = 0.7953$Hz in the

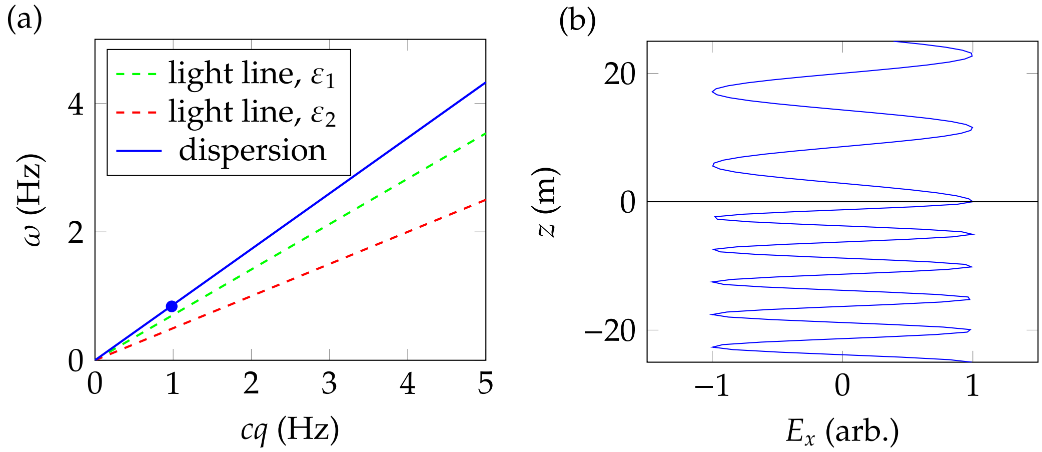

Figure 2.4: Dispersion at the interface (a) of two uniform dielectrics. Electric field (b) simulated at $x = 0$, $cq = 0.9814$Hz, and $\omega = 0.7953$Hz (blue dot in (a)); Note in (a) that the dispersion is above the light line in both dielectric materials.

dispersion, the wave propagates freely through the interface. Thus all solutions in this dispersion satisfy transparent boundary conditions. Essentially, there are no surface modes for two dielectrics. As we will see, surface plasmons are bound to the interface which produces a different field profile.

2.7 Example with Drude metal surface

One of the most intriguing collection of materials has been metallic conductors due to their obvious role in technological advancements [69, 70]. In 1900 in his "Zur Elektronentheorie der Metalle" [71], Drude proposed his classical theory of metals. The electrons in the Drude model are free to roam the metal classically, much like an ideal gas, but under the influence of an external electric field and collisions with surrounding electrons and fixed positive ions [72, 73]. The conductivity of the metal is given by Drude model as [61, 72],

$$\sigma(\omega) = \frac{i n_s e^2}{4\pi m(\omega + i\gamma)} = \frac{i\omega_p^2}{\omega + i\gamma} \tag{2.42}$$

where n_s, m, and e are the electrons' density, mass, and charge respectively. The relaxation time is $\tau \equiv 1/\gamma$, that is, the average "free" time an electron is assumed to spend between collisions [72], so that the damping γ accounts for losses. $\omega_p =$

$\sqrt{n_s e^2/4\pi m}$ is defined as the plasma frequency of the metal. Although Eq. (2.42) was derived using classical modelling of electrons with various simplifications, it is a good representation of metallic behaviour in response to the electromagnetic spectrum for low frequencies.

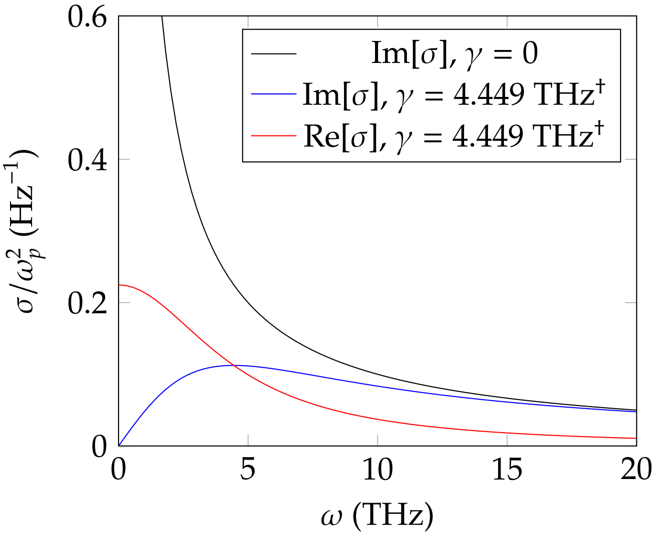

Figure 2.5: Drude model conductivity as given in Eq. (2.42) with damping (gray and blue), and without (black) for gold. † Drude damping for gold is provided in Ref. [74]

Here, we change one of the materials from Sec. 2.6 to a metal, employing the Drude model for frequency dependent conductivity. The permittivity for such a system as depicted in Fig. 2.6 (a), can be derived from Eq. (2.14) and can be written

$$\varepsilon(z;\omega) = \begin{cases} \varepsilon_1 & z > 0 \\ 1 - \frac{\omega_p^2}{\omega(\omega+i\gamma)} & z < 0. \end{cases} \tag{2.43}$$

One can immediately note that this permittivity is negative for $\omega^2 < \omega_p^2$ (ignoring γ which is usually very small compared to the frequency) and for $z < 0$. It can be seen in Sec. 2.8 that this determines the surface plasmonic modes. For Au, $\omega_p = 9.6\,eV$ and $\gamma = 0.0228\,eV$ [74].

Substituting Eq. (2.43) into Eq. (2.40), and solving for the frequency yields the following dispersion shown in Fig. 2.6(b), with $\varepsilon_1 = 1$ for a vacuum-gold interface.

At frequencies above ω_p in Fig. 2.6(b) (light blue solid line), the permittivity

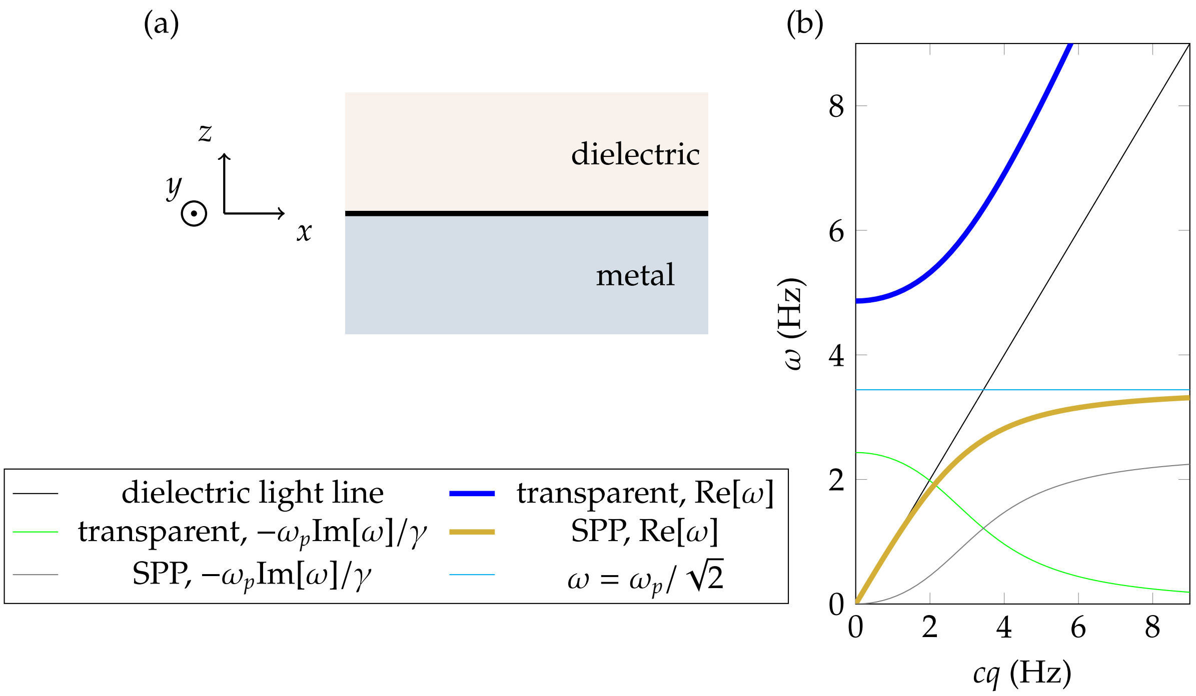

Figure 2.6: (a) Dielectric-metal interface. (b) Dispersion of vacuum-*Au* interface for transparent and SPP modes. Imaginary values are scaled up by $\frac{\omega_p}{\gamma}$. Yellow branch corresponds to the SPP mode when the field decays away (see Fig. 2.7) from the interface (right).

is positive and we observe transparent solutions as demonstrated by the field profile in Fig. 2.7(b). This solution has frequency large enough so that k_1, k_2 have large real part and very small imaginary part so that the field profile is oscillatory close to the interface. Since the (real part of) permittivity for metal in Eq. (2.43) is positive when $\omega \geq \omega_p$, the metal becomes transparent to the electromagnetic field which propagates through it. According to Eq. (2.40), the frequency of SPP ω is complex, since q is real and the permittivity given by Eq. (2.43) is complex. The imaginary part of ω is due to loss of field amplitude over time. This is due to $\exp(-i\omega t)$ dependence of the fields. We can observe in Fig. 2.6(b) that the transparent modes (dark blue solid line) that propagate through the interface have decreasing temporal loss (green solid line) with increasing wavenumber.

SPP mode exists when $\varepsilon_2 < 0$ below $\omega_p/\sqrt{2}$. At these frequencies, the charge carriers in the metal respond to the electric field, and their oscillation waves travel at the surface [31] along with this mode. The field profile can be seen to decay away from the interface in Fig. 2.7(a). The mode frequency Re[ω] has an asymptote at $\omega_P/\sqrt{2}$ as shown in Fig. 2.6, thus the group velocity decreases and tends to zero for increasing wavenumber. In Fig. 2.6(b) the SPP modes (gold solid line) that are confined to the interface have gradually increasing damping Im[ω] (gray solid line), with increasing wavenumber, also having a different asymptote. This is in agreement with the fact that the damping is proportional to the group velocity of the mode [31]. As the x-component of SPP wavelength becomes shorter (increasing in-plane wavenumber), the SPP is forced to travel at decreased group velocity as the polariton cannot oscillate faster than $\omega_P/\sqrt{2}$.

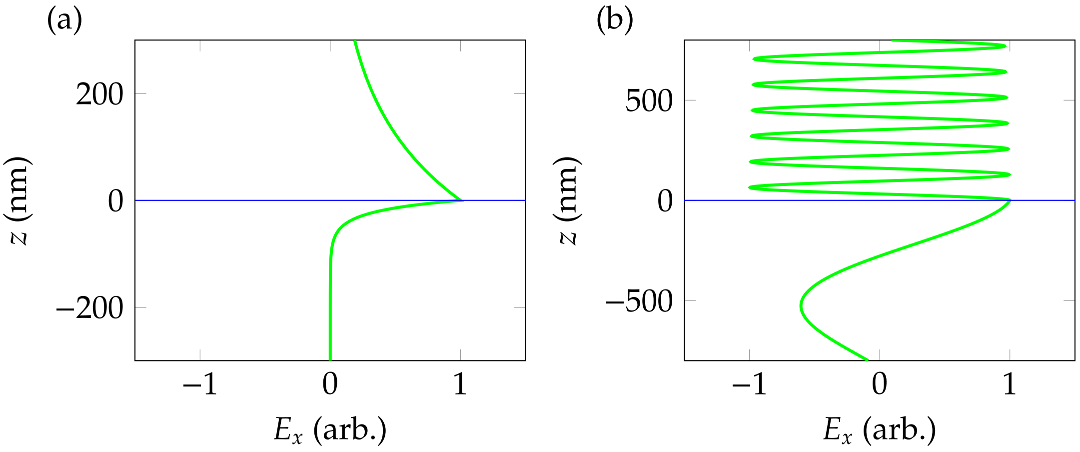

Figure 2.7: Electric field simulated for the dispersion at the interface. $q = 1.65 \times 10^7 m^{-1}$. (a) SPP mode ($Re(\omega)/c = 1.56 \times 10^7 m^{-1}$). (b) transparent mode ($Re(\omega)/c = 5.16 \times 10^7 m^{-1}$).

2.8 Electromagnetic eigenmodes

In the literature, most of work approaches surface plasmons by considering the in-plane wavenumber q to be complex and frequency to be real [25, 75–82]. This is usually for focusing on the spatial decay of surface modes calculating their propagation length along the interface. Whilst this is of immediate importance when designing plasmonic devices, it contains limited information on the spectral features of the mode. Moreover, the conventional plasmonic modes present a "closed" system over time, meaning that energy is not modelled to leak away from the surface plasmon mode as time passes. Here, we intend to do the alternative, that is, focus instead on complex frequency and real wavenumber as the imaginary part of the frequency can be related to a phenomenological loss arising partly from material loss. Then we find that the imaginary part of frequency $\mathrm{Im}[\omega]$ is representing spectral linewidths of surface plasmon polaritons resonance peaks in transmission spectra, which is measured as the energy ratio of outgoing to incoming beam intensities. Furthermore, $\mathrm{Im}[\omega] < 0$ would represent the temporal decay of electromagnetic eigenmodes as the phasor of the eigenmodes has a factor of

$$\exp\left(-i(\mathrm{Re}[\omega] + i\mathrm{Im}[\omega])t\right) \propto \exp(\mathrm{Im}[\omega]t). \tag{2.44}$$

Thus $\mathrm{Im}[\omega] < 0$ would represent the temporal decay rate of the eigenmode, providing information on the lifetime of the mode after excitation. It turns out further that temporal loss of mode also has dependence on the real part of conductivity spectrum related to absorption losses within the conductor. In summary, by allowing frequency to have an imaginary part, we gather information on temporal loss of the modes otherwise hidden by the alternative approach of real frequency and complex in-plane wavenumber.

CHAPTER 3

SPPs on homogeneous conductor surfaces

Now that the formalisms and theory of surface plasmons as electromagnetic modes has been established, in this chapter we will study surface plasmons modes in structures involving Drude metals. The piecewise permittivity will now gain frequency dependence. We will gradually progress from an example of semi-infinite metal structure considered in Ch. 2, to an infinitesimally thin film homogeneous conductor structure. These examples and their SPP dispersion results are already established in the literature, although we will present them in the unusual format of complex frequency $\omega = \omega' + i\omega'' \in \mathbb{C}$ but real in-plane wavenumber $q \in \mathbb{R}$. This implies that the out-of-plane component of the wavenumber $k \in \mathbb{C}$ is complex in general.

3.1 Finite thickness metal sheet

With the result in Fig. 2.7 in mind, and before moving on to graphene sheet, we consider a sheet of metal of a finite thickness d, enclosed in a dielectric as depicted in Fig. 3.1.

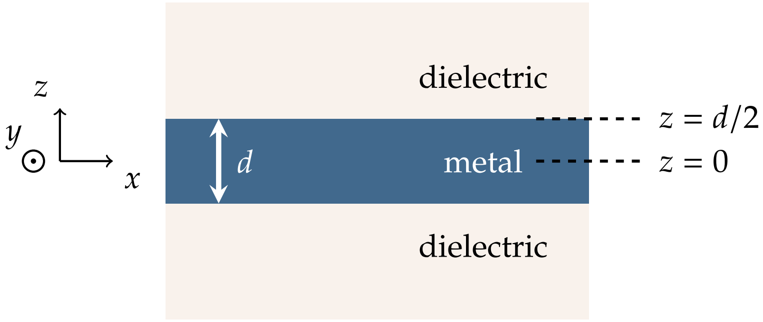

Figure 3.1: Metal of thickness d sandwiched between two semi-infinite dielectric insulators producing two dielectric-metal interfaces, each a distance of $d/2$ away from $z = 0$.

The permittivity defining this structure is

$$\varepsilon = \begin{cases} \varepsilon_1 = 1 & |z| > d/2, \\ \varepsilon_2 = 1 - \frac{\omega_p^2}{\omega(\omega + i\gamma)} & \text{otherwise}, \end{cases} \tag{3.1}$$

where d is the thickness of the metal in z-direction, we have employed Drude model Eq. (2.42) for the conductivity, ε_1 is the permittivity of the dielectric, and ε_2 is the permittivity of the metal.

We begin the analysis in the TM polarisation. This time there are two dielectric-metal interfaces. We use the boundary conditions Eqs. (2.29) and (2.30) to find two dispersion relations (see Appendix A) for the SPP modes [31],

$$\varepsilon_2 k_1 + \varepsilon_1 k_2 \tanh \frac{dk_2}{2i} = 0 \quad (H\text{-symmetric}), \tag{3.2}$$

$$\varepsilon_2 k_1 \tanh \frac{dk_2}{2i} + \varepsilon_1 k_2 = 0 \quad (H\text{-antisymmetric}), \tag{3.3}$$

where k_1 is the out-of-plane wavenumber in the dielectric, k_2 is the out-of-plane wavenumber in the metal, k_n are given by Eq. (2.36), and q is the in-plane wavenumber.

The result of two dielectric-metal interfaces is that the system has two types of SPP modes, one with symmetric (corresponding to Eq. (3.2)) and the other with anti-symmetric (corresponding to Eq. (3.3)) magnetic field H_y with respect to z-direction. Note that this seperation of SPP modes into symmetric and anti-

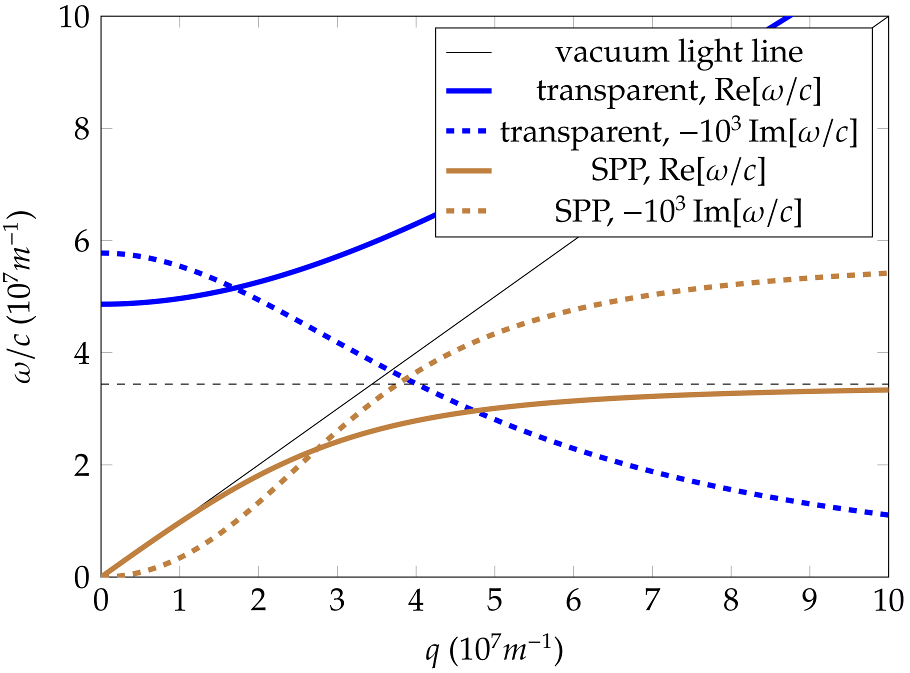

Figure 3.2: Dispersion for the H-antisymmetric mode for the double interface setup of gold sandwiched between dielectric. $d = 70nm$. Imaginary values are scaled up by $\times - 10^3$. The SPP mode is in brown line, with solid (dashed) for real (imaginary) part of frequency. The transparent mode (non-SPP) is in blue, and solid (dashed) for real (imaginary) part of freqeuncy. The black dashed line indicates the value of $\sqrt{\omega_p}/2$ the real frequency of SPP mode approaches for large q.

symmetric types is not derived from the conductivity of the metal since Eqs. (3.2) and (3.3) are obtained using general expressions of permittivity ε_2 sandwiched between ε_1. The separation is reflected in the tanh $\frac{dk_1}{2i}$ term in the equations, since it is the only term dependent on d which is the distance between the interfaces. To get the modes of the system in Fig. 3.2, we substitute the constant positive real permittivity of the dielectric and frequency-dependent Drude permittivity, Eq. (3.1), into secular Eqs. (3.2) and (3.3), as we did in the single interface case.

Note that there are the square-roots $k_n = \sqrt{\varepsilon_n \omega^2/c^2 - q^2}$ (see Eq. (2.36)) occuring in Eqs. (3.2) and (3.3). Each square-root has not just one but two possible results in the complex plane that differ by a factor of -1. For example, the square-root of $2i$ has two possible results $\sqrt{2i} = \pm(1 + i)$. Therefore, to find all mathematical solutions to Eqs. (3.2) and (3.3) for $\omega \in \mathbb{C}$, we must consider the equations with both possible signs of all the square-roots. Mathematical theorem to aid in numerical implementation of considering all possibilities can be found in [83]. It turns out that the SPP mode solutions require both the square-roots in Eqs. (3.2) and (3.3) to have positive signs.

Fig. 3.2 shows the resulting H-antisymmetric dispersion, Eq. (3.2), for a $70nm$ thick sheet of gold. The surface plasmon dispersion (brown solid line) has a shape similar to the single interface case (see Fig. 2.6). The frequency is still less than that of the light line in vacuum, indicating the confinement of the mode to the interfaces. Again, the frequency of the dispersion has an asymptote at $\mathrm{Re}[\omega] = \omega_p/\sqrt{2}$.

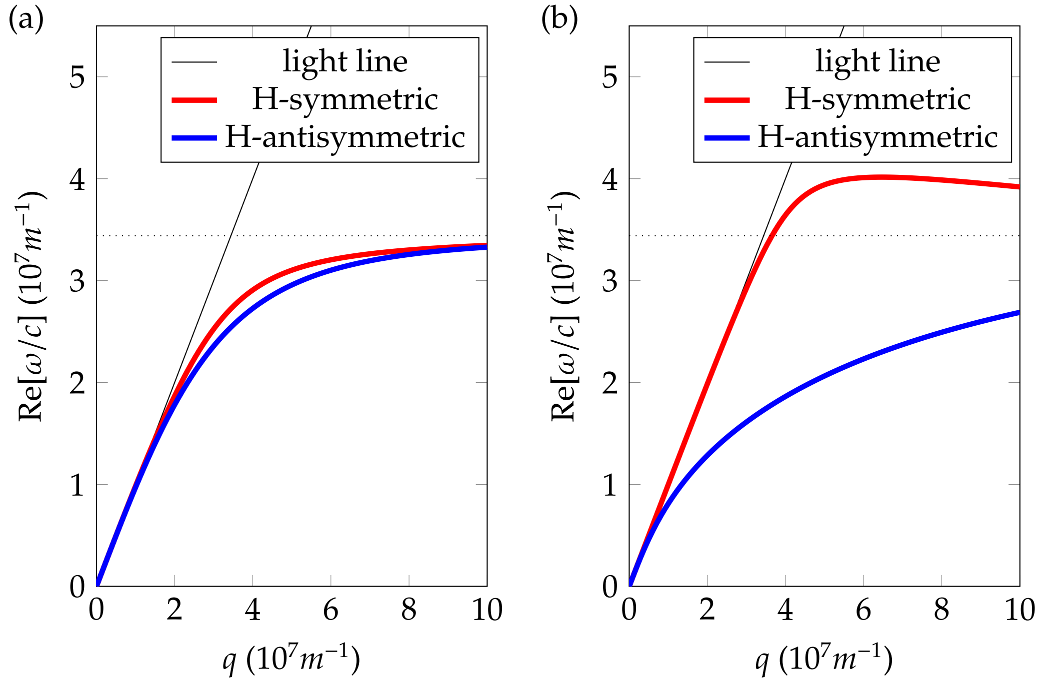

Figure 3.3: Both H-symmetric and H-anti-symmetric modes for the SPP. Thickness of metal film decreases from $50nm$ (a) to $10nm$ (b).

Now, we discuss the overlap of electromagnetic fields between the interfaces. It is instructive to view the effect of metal thickness d on the H-symmetric and H-antisymmetric modes. As Fig. 3.3 demonstrates, the $\mathrm{Re}[\omega]$ for the two modes gets far apart as the thickness d decreases i.e. the two boundaries at the metal-dielectric interface come closer. This will be an important factor when considering the atomically thin graphene layer. As the two interfaces are moved closer or farther, the overlap of the evanescent fields from the interfaces changes, causing

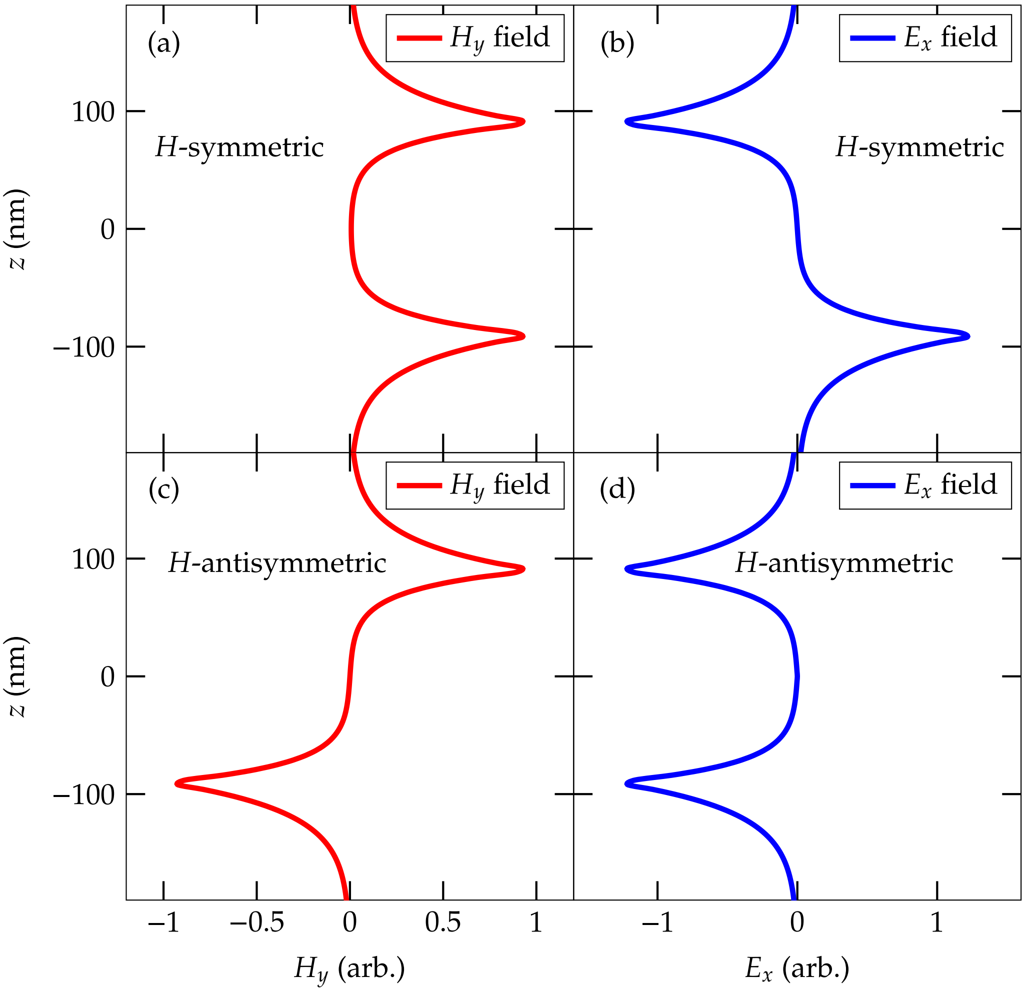

Figure 3.4: Electric and magnetic field profiles across the double interface setup. d is $180nm$, and the in-plane wavenumber q is chosen to be $5 \times 10^7 m^{-1}$. The modes plotted are chosen so that $\omega < cq$.

a change in the wavenumber of the eigenmode of the system. For a constant wavenumber, this effect presents itself as the change in frequency separation of the H-symmetric and H-antisymmetric modes. For near zero thickness, the H-symmetric mode tends closer to the light line(see Fig. 3.3 red curve), gradually losing its evanescent nature. The H-anti-symmetric mode, on the other hand, moves further away from light line (see Fig. 3.3 blue curve), tending to zero frequency. The H-antisymmetric mode survives the reduction of thickness up to an atomically thin layer of metal, which will also be evident when we look at infinitesimally thin metallic sheet. The SPP mode field profiles are plotted for a q value for the different modes in Fig. 3.4. As expected, the fields decay away from

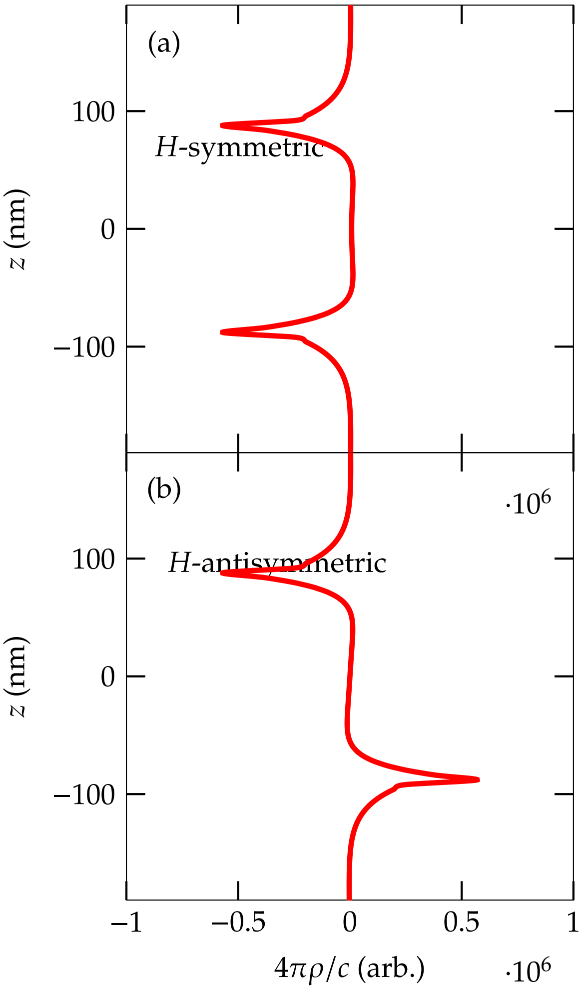

Figure 3.5: Charge density for the case of Fig. 3.4. d is $180nm$, and the in-plane wavenumber q is chosen to be $5 \times 10^7 m^{-1}$. The modes plotted are chosen so that $\omega < cq$.

boundaries for the SPP modes in the dispersion. The charge density profile (see Appendix A) calculated using

$$4\pi\rho = \frac{c}{i\omega}(\varepsilon_n \frac{\omega^2}{c^2} - 2q^2)H_y \tag{3.4}$$

is shown in Fig. 3.5 and can be seen to follow the profile of and proportional to H_y field.

It is useful to look at how the frequencies ω of H-symmetric and H-antisymmetric modes changes with d for a fixed in-plane wavenumber q as shown in Fig. 3.6. At very large thickness of metal film, the two SPP dispersion curves merge into the same dispersion frequency and wavenumber, close to the dispersion of the semi-infinite metal case in Fig. 2.6. As d increases, $\tanh \frac{dk_1}{2i}$ is close to 1 and the overlap of evanescent fields at two interfaces decreases.

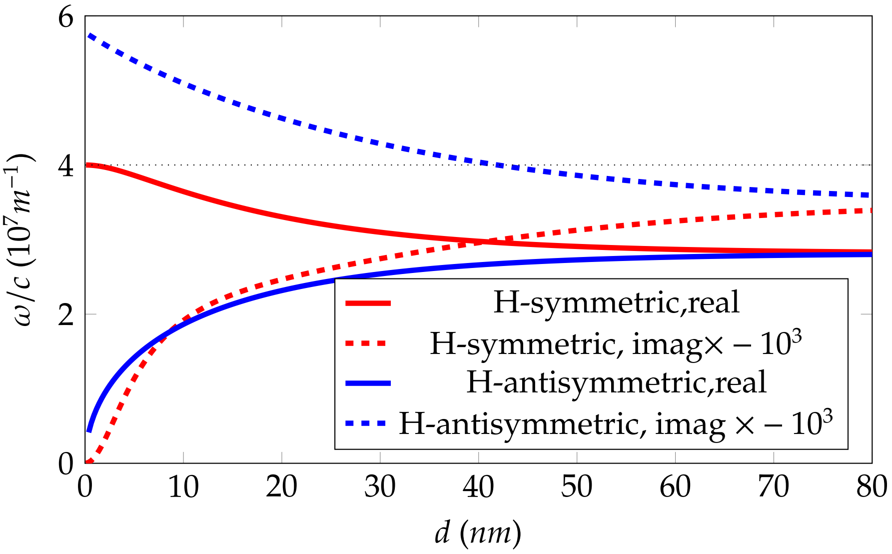

Figure 3.6: For a fixed value of $q = 4\times10^7 m^{-1}$, ω/c is plotted for changing thickness d for both the H-symmetric and H-anti-symmetric mode. The light line is black dotted.

We now move our attention to transparent modes (solid blue line in Fig. 3.2) with $\text{Re}[\omega] \geq \omega_p$. As the electromagnetic waves oscillate at high frequencies $\text{Re}[\omega] \geq \omega_p$, the free electrons do not engage with them and light simply passes through interface. In addition to the transparent mode shown in Fig. 3.2, there are an infinite more of transparent modes for the structure (not shown in figure), arising due to Fabry-Pèrot interference, a series of transmission and reflection at the interfaces. The coupling is controlled by the $\tanh \frac{dk_1}{2i}$ term, so that decreasing thickness sets the discrete frequencies further apart tending to the case of a single interface. Fig. 3.7 shows that the field propagates away from the boundaries when the frequency is chosen from the non-SPP branches of the dispersion.

3.2 Infinitesimally thin layer

Graphene is an atomically thin layer as a material. Therefore it is instructive to first formulate on SPP in an infinitesimally thin layer of conductor. Mathematically, there are two ways to approach this and we will look at both approaches for their

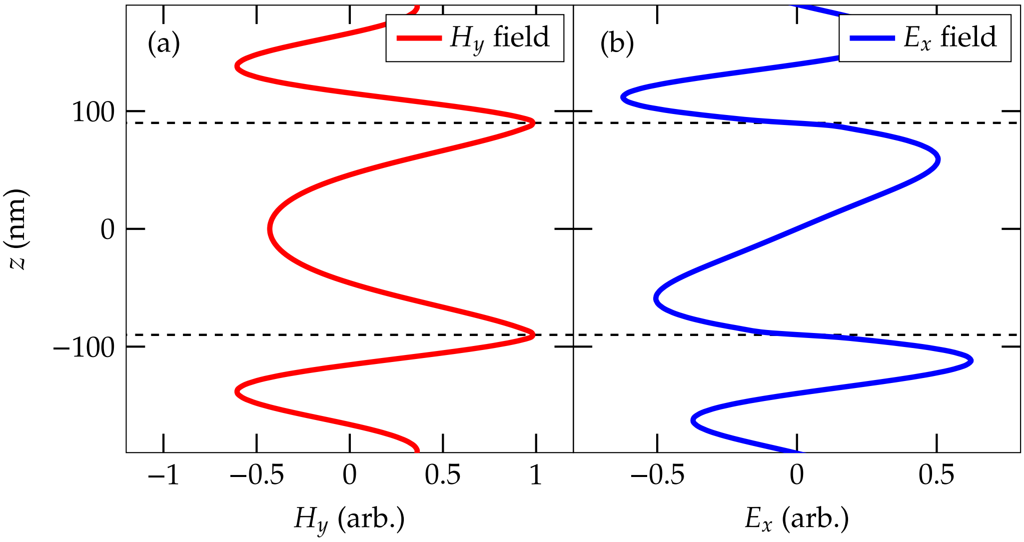

Figure 3.7: Field profiles across the double interface setup. d is $180nm$, and the wave-vector k_x is chosen to be $5 \times 10^7 m^{-1}$. This time, the frequency is chosen from the transparent mode of the dispersion. Horizontal dashed lines are at the interfaces $z = \pm d/2$.

different qualitative understanding.

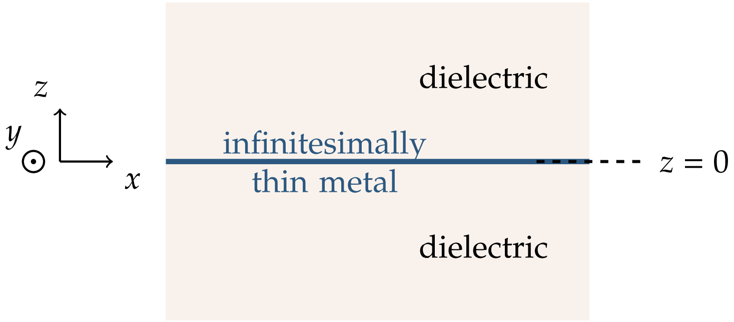

Figure 3.8: Infinitesimally thin metallic layer sandwiched between two semi-infinite dielectric materials.

3.2.1 Surface conductivity

The first method to move to the infinitesimally thin structure, as depicted in Fig. 3.8, involves analytically transforming the secular Eqs. (3.2) and (3.3) by mathematically taking the limit $d \to 0$. This method brings to light the difference between a bulk conductivity σ (which we have used so far for metals) and a surface conductivity σ_{surf}, analogous to the connection between the free current density $\mathbf{J}_f$ and surface free current density $\mathbf{K}_f$ appearing in the boundary condition Eq. (2.30).

We can also calculate the modes of the infinitesimally thin metal structure Fig. 3.8 by considering the permittivity of the structure itself in terms of a Dirac delta function $\delta(z)$ like so

$$\varepsilon(\omega; z) = \begin{pmatrix} \varepsilon_{\|} & 0 & 0 \\ 0 & \varepsilon_{\|} & 0 \\ 0 & 0 & 1 \end{pmatrix}, \tag{3.5}$$

where

$$\varepsilon_{\|} \equiv 1 + \delta(z) \frac{4\pi i \sigma_{\mathrm{surf}}(\omega)}{\omega} \tag{3.6}$$

is the permittivity in planar directions, and the permittivity of background dielectric is $\varepsilon = 1$ (vacuum). Note that due to the property of $\delta(z)$ function as described by Eq. (2.31) implies that its units in Eq. (3.5) are that of z^{-1}. This is consistent with the fact that the surface conductivity is related to the bulk conductivity, assuming homogeneity of metal in z direction, by a phenomenological thickness of sheet d_0 as

$$\sigma_{\mathrm{surf}} = d_0 \sigma. \tag{3.7}$$

In the TM polarisation, the Maxwell's equations for a plane wave solution ansatz given by Eq. (2.35) with $k_y = 0$ become,

$$i\omega H_y - \partial_z E_x + iqE_z = 0\,, \tag{3.8}$$

$$i\partial_z H_y + \omega \varepsilon_{\|} E_x = 0\,, \tag{3.9}$$

$$qH_y + \omega E_z = 0\,. \tag{3.10}$$

In the dielectric regions ($z \neq 0$), we find the wave equation for H_y and the dependent field components E_x, E_z:

$$\partial_z^2 H_y + (\omega^2 - q^2) H_y = 0, \tag{3.11}$$

$$E_x = -\frac{i}{\omega}\partial_z H_y, \tag{3.12}$$

$$E_z = -\frac{q}{\omega} H_y\,. \tag{3.13}$$

We obtain continuity of field across the interface by integrating Maxwell's equations, in this case specifically Eqs. (3.8), (3.9), and (3.10), across the interface for a vanishing interval $\int_{0_-}^{0_+} \cdot\, dz$, obtaining,

$$E_x(0_+) - E_x(0_-) = 0\,, \tag{3.14}$$

$$-H_y(0_+) + H_y(0_-) - 4\pi\sigma_{\text{surf}} E_x(0) = 0\,, \tag{3.15}$$

where 0_+ (0_-) is a positive (negative) infinitesimal. Thus tangential electric field is continuous, conforming to Eq. (2.29), but tangential magnetic field has a step given by a surface current, conforming to Eq. (2.30). Evidently, we find that $K_{f,x} = \sigma_{\text{surf}} E_x(0)$, so that in this polarisation, the current density oscillates in a longitudinal orientation within the conductor surface. From both conditions given by equations (3.14) – (3.15) we find the field components in all space as,

$$H_y = A\,\text{sgn}(z) e^{ik|z|}\,, \tag{3.16}$$

$$E_x = A\frac{k}{\omega} e^{ik|z|}\,, \tag{3.17}$$

$$E_z = -A\frac{q}{\omega}\text{sgn}(z) e^{ik|z|}\,, \tag{3.18}$$

corresponding to outgoing wave boundary conditions. Here, A is a normalization constant,

$$\text{sgn}(z) = z/|z| \tag{3.19}$$

and k is the normal component of the wave number in vacuum satisfying the relation

$$\omega^2 = k^2 + q^2\,. \tag{3.20}$$

Finally, using Eq. (3.15), we obtain a secular equation for the TM SPP mode as,

$$4\pi k\sigma_{\text{surf}}(\omega) + 2\omega = 0\,. \tag{3.21}$$

The complex frequency solutions are presented in Figs. 3.9 and 3.10 for a gold sheet with $d_0 = 3.4\text{Å}$, close to a monoatomic gold layer. The approximate interlayer distance of graphite [84] is also $d_0 = 3.4\text{Å}$. For Drude metal surfaces, we find TM SPPs that are guided modes, meaning that the real part of their frequency is nonzero, since they require that the permittivity of structure change sign across the dielectric-metal interface. We find, after solving Eq. (3.21) considering both signs of square-root in k, that solutions are found only for $\text{Re}[k] > 0$ or $\text{Im}[k] < 0$. In addition we find modes with zero real frequency $\text{Re}[\omega] = 0$ which we refer to as **anti-waveguide (anti-WG)** modes, alluding to references [85, 86]. The condition $\text{Re}[\omega] = 0$ results in purely imaginary out-of-plane wavenumber $\text{Re}[k] = 0$ for these modes in this system.

The secular equation for TE polarisation is obtained in a similar way using an ansatz for the electric field

$$E_y = e^{iqx} \times \begin{cases} Ae^{ikz} + Be^{-ikz} & z > 0, \\ Ce^{ikz} + De^{-ikz} & z < 0. \end{cases} \tag{3.22}$$

The Maxwell's equations in this case reduce to

$$\omega\varepsilon_{\|}E_y - i\partial_z H_x - qH_z = 0\,, \tag{3.23}$$

$$\partial_z E_y + i\omega H_x = 0\,, \tag{3.24}$$

$$-qE_y + \omega H_z = 0\,. \tag{3.25}$$

For this polarisation, we may write the wave equation for E_y and dependent

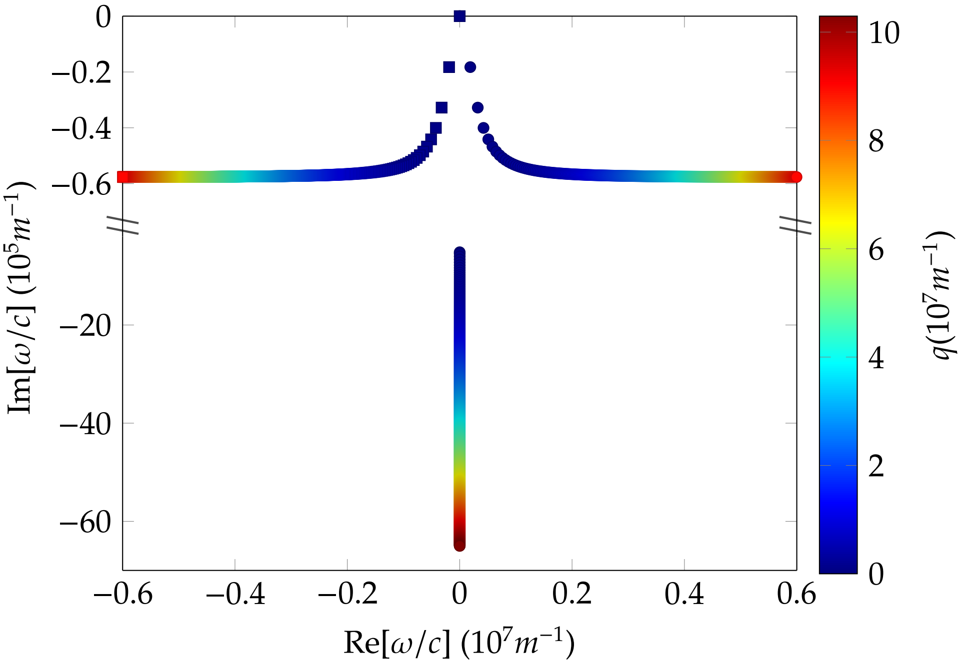

Figure 3.9: TM SPP dispersion for a thin infinitesimal sheet of gold with d_0 = 3.4Å suspended in vacuum, depicted in the complex ω-plane.

components H_x, H_z for all space as

$$\partial_z^2 E_y + (\varepsilon_{\|}\omega^2 - q^2)E_y = 0\,, \tag{3.26}$$

$$H_x = \frac{i}{\omega}\partial_z E_y\,, \tag{3.27}$$

$$H_z = \frac{q}{\omega}E_y\,. \tag{3.28}$$

Similarly to what we did before, we integrate Eqs. (3.23) and (3.24) across the conductor, obtaining

$$H_x(0_+) - H_x(0_-) = \sigma_{\text{surf}} E_y(0)\,, \tag{3.29}$$

$$E_y(0_+) - E_y(0_-) = 0 \tag{3.30}$$

conforming the tangential discontinuity of magnetic field Eq. (2.30) and continuity of electric field Eq. (2.29), respectively. A solution satisfying outgoing or incoming

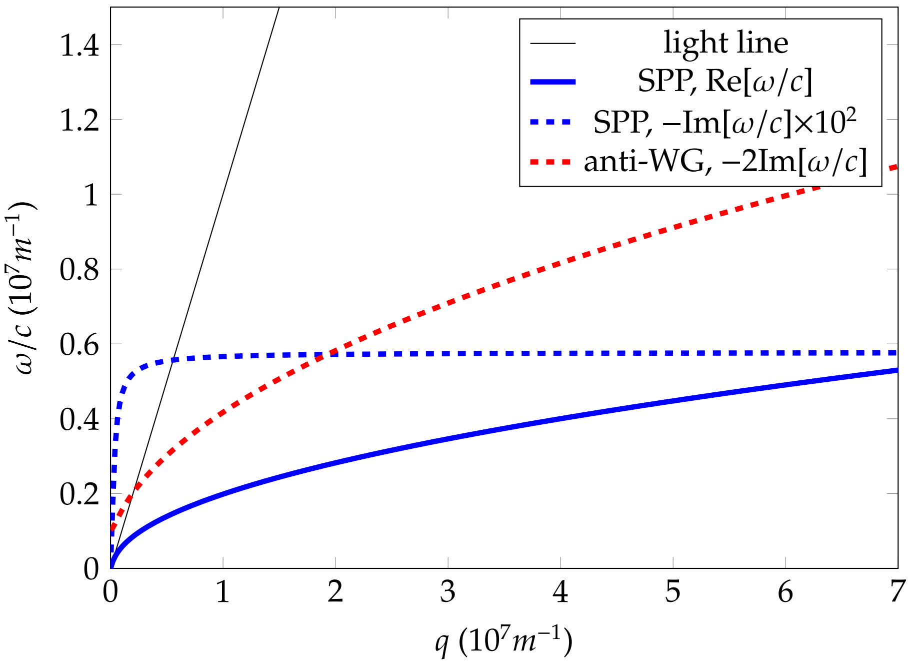

Figure 3.10: TM SPP dispersion for a thin infinitesimal sheet of gold with d_0 = 3.4Å.

wave boundary conditions then takes the form:

$$E_y(z) = Ae^{ik|z|}, \tag{3.31}$$

$$H_x(z) = -A\frac{k}{\omega}\text{sgn}(z)e^{ik|z|}, \tag{3.32}$$

$$H_z(z) = \frac{q}{\omega}Ae^{ik|z|}, \tag{3.33}$$

and Eq. (3.29) provides a secular equation for the TE mode:

$$2k + 4\pi\omega\sigma_{\text{surf}}(\omega) = 0, \tag{3.34}$$

allowing only for anti-WG solutions shown in complex frequency plane in Fig. 3.11, where the solutions are found for Im[ω] < 0 and Re[ω] = 0. Please note that if $\sigma_{\text{surf}} \in \mathbb{R}$ with $q \in \mathbb{R}$ then we have using Eq. (3.20)

$$\omega = \frac{q}{\sqrt{1 - 2\pi^2\sigma_{\text{surf}}(\omega)^2}}, \tag{3.35}$$

implying that $ik, \omega \in \mathbb{R}$ and $\omega < q$ if σ_{surf} is sufficiently small. This means that the mode is evanescent ($ik \in \mathbb{R}$) but not temporaly decaying ($\omega \in \mathbb{R}$) for a real $\sigma_{\text{surf}} \in \mathbb{R}$.

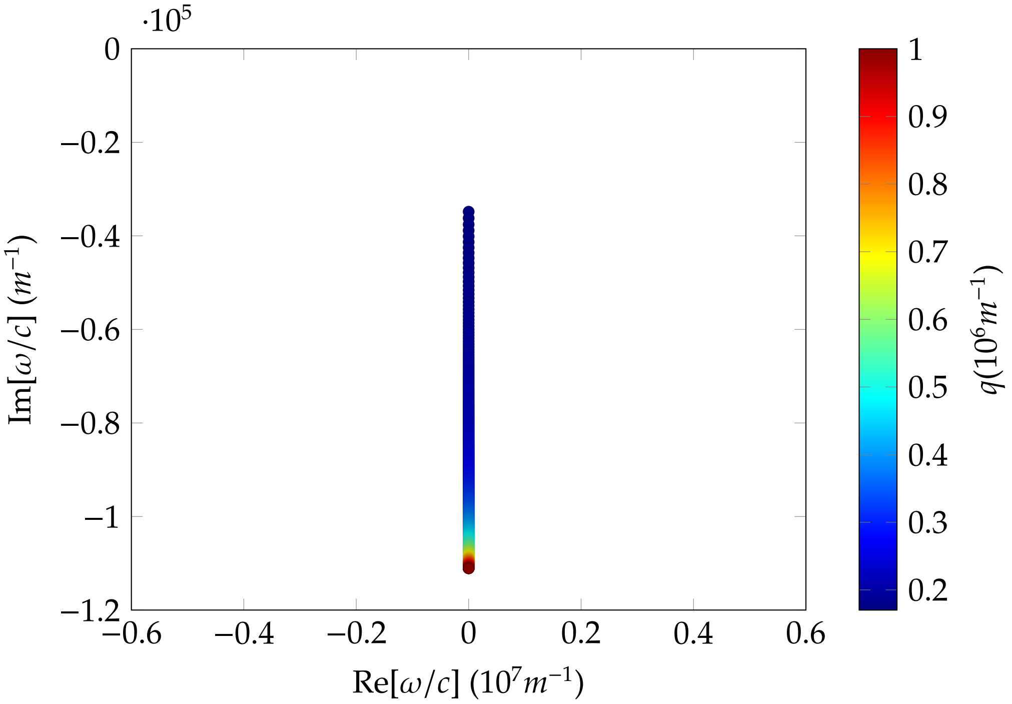

Figure 3.11: TE mode dispersion for a thin infinitesimal sheet of gold with $d_0 = 3.4\text{Å}$ suspended in vacuum.

In summary, we have found that TM SPPs in an infinitesimally thin Drude metal sheet have their frequency dispersion very similar to the case of a Drude metal slab of finite thickness. This SPP mode is H-antisymmetric (E-symmetric) in its field profile. By allowing complex frequency we show that an additional, anti-WG mode ($\text{Re}[\omega] = 0, \text{Im}[\omega] \neq 0$) exists in this structure, purely evanescent in time. We will make use of Eqs. (3.21) and (3.34) in the Ch. 5 to investigate the modes in these polarisations in a homogeneous graphene sheet.

CHAPTER 4

Graphene conductivity

So far we have explored SPP modes using Drude model, which has certainly provided us with an understanding of the SPPs close to plasma frequency. To be able to utilize SPP modes for plasmonic devices involving graphene for a larger range of frequencies, we must equip ourselves with a wider frequency-range model. The Drude model assumes that conduction electrons in a metallic structure of immobile positive ions behave like a gas of particles with only the forces associated with collisions affecting motion [72]. In reality, at certain frequencies, conductors typically experience a deviation from this kinetic theory model for electrons. An improved model is needed, and this is where quantum theory can step in to the rescue, and so that is what we will mostly focus on in this chapter. Conductivity of graphene in literature is typically a sum of two well known parts: the interband and the intraband [41, 50, 58, 87, 88]. Although the conductivity spectrum can be acquired by self-consistent field theory [89], we will present a quantum theory model of conductivity. We will find in this better model, the features of conductivity already accounted for in the Drude model, along with improvements in addition to it. The contents of this chapter have been amalgamated and adapted from different sources [65, 87, 88, 90–99] to fit into the context of SPPs in graphene in preparation of later chapters.

Note that this chapter deals with the electronic response in graphene, as such for this chapter the expression $\hbar\mathbf{k}$ is representing two dimensional **crystal momentum** in graphene, and the symbol $\mathbf{q}$ is the **wavenumber of photons**.

4.1 Electronic structure of Graphene

Graphene is an atomically thin semimetal made of carbon atoms arranged in a honeycomb lattice [41], which is depicted in Fig. 4.1. A carbon atom on its own has 4 valence electrons in the outer shell in s, p_x, p_y, p_z orbitals [100]. In graphene, each carbon atoms bonds to its three neighbouring atoms using an electron each from s, p_x, p_y orbitals which hybridise into the sp^2 orbital forming 3 σ-bonds [101]. The remaining 4th electron per atom remains in the p_z orbital oriented normal to the graphene's plane. Hopping of electrons among the p_z orbitals forms π-bonds provides graphene with its conducting properties [102].

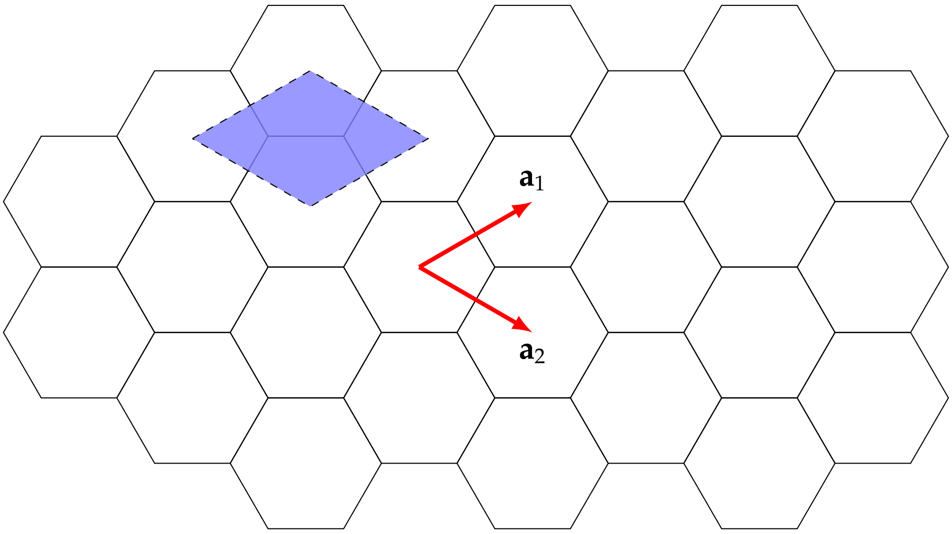

Figure 4.1: Honeycomb lattice of carbon atoms (vertices) in graphene. The blue rhombus represents the primitive cell containing two carbon atoms.

The appropriate unit cell for such a periodic arrangement contains two neighbouring carbon atoms forming a triangular lattice. The lattice vectors are [41]

$$\mathbf{a}_1 = \left(\frac{\sqrt{3}}{2}, \frac{1}{2}\right)a, \tag{4.1}$$

$$\mathbf{a}_2 = \left(\frac{\sqrt{3}}{2}, \frac{-1}{2}\right)a, \tag{4.2}$$

where $a = |\mathbf{a}_1| = |\mathbf{a}_2|$ is the lattice constant. The reciprocal lattice vectors are [41]

$$\mathbf{b}_1 = \left(\frac{2\pi}{\sqrt{3}a}, \frac{2\pi}{a}\right), \tag{4.3}$$

$$\mathbf{b}_2 = \left(\frac{2\pi}{\sqrt{3}a}, \frac{-2\pi}{a}\right), \tag{4.4}$$

which form the reciprocal lattice. The first Brillouin zone in the reciprocal lattice is hexagonal with high-symmetry K points at its vertices, one of which is at $\mathbf{K} = (0, 4\pi/3a)^T$.

By considering hopping of the π electrons only between nearest neighbouring carbon atoms, one may write a tight-binding model for the Hamiltonian of the quantum electronic system [41, 103].

For small doping near $E = 0$, the electronic dispersion is near the K point in the Brillouin zone and the effective Hamiltonian is [50, 104]

$$H = \hbar v_0 \begin{pmatrix} 0 & k_x - ik_y \\ k_x + ik_y & 0 \end{pmatrix}, \tag{4.5}$$

where $v_0 = \sqrt{3}\gamma a/2\hbar$ is the band velocity, γ is the transfer integral which is of the order of $3eV$ [104], and $\hbar$ is reduced Plank's constant.

The effective Hamiltonian for carriers in graphene Eq. (4.5) can be written in terms of Pauli matrices as

$$H = v_0 \sum_{\alpha} \sigma_\alpha \hat{p}_\alpha \tag{4.6}$$

where σ_α are Pauli matrices, $\hat{p}_\alpha$ is the $\alpha = x, y$ cartesian coordinate of momentum operator.

The energy eigenvalues of the Hamiltonian Eq. (4.6) are

$$E_{\mathbf{k}j} = (-1)^j \hbar v_0 k, \tag{4.7}$$

giving the associated eigenstates as

$$|\mathbf{k}1\rangle = \frac{1}{\sqrt{2}k}\begin{pmatrix} k \\ k_x + ik_y \end{pmatrix}, \tag{4.8}$$

$$|\mathbf{k}2\rangle = \frac{1}{\sqrt{2}k}\begin{pmatrix} k_x - ik_y \\ -k \end{pmatrix}, \tag{4.9}$$

where $\mathbf{k} = (k_x, k_y)$ is a vector in Brillouin zone with $k \equiv |\mathbf{k}|$. Conducting electrons near K point thus move through graphene with linear dispersion with velocities of $v_0 \approx 10^6 m/s$ [38].

The chemical potential of graphene can be changed by application of gate voltage. By keeping the chemical potential near zero, we can have crystal momentum without moving into non-linear electronic dispersion.

4.2 The Kubo formula for conductivity

One of the major principles of quantum mechanics is the distinction between state and measurement [105]. Having chosen an appropriate representation, observable quantities like energy can be represented using quantum operators which contain information on what we can measure for that observable. A quantum system is defined by its Hamiltonian operator along with the state of the system with probabilistic information on measurements. To get insightful intuition of values of a desired observable, we take a statistical expectation value of its quantum operator. The problem of modelling response in constitutive equations is not specific to conductivity. Indeed, it is a more general problem where a response of a system is to be determined under external influences. Kubo [90, 91] presented a formalism addressing this general problem using statistical mechanics theory, illustrating the method with an example of finding magnetic susceptibility under an external magnetic field. Specifically, a Kubo formula considers a perturbation of the Hamiltonian at a point in time, due to some external force, and then enquires on the change in the expectation of a chosen observable as a response to the force. If the perturbation can be written in terms of an external electric field, and the observable chosen to be the current, then the conductivity tensor can be obtained by using Kubo formula [65].

Using the Kubo formula [65, 92], one can obtain a well known result [65, 87, 104] for the conductivity of band metals which can be applied to graphene

$$\sigma_{\alpha\beta}(\mathbf{q},\omega) = i\frac{e^2}{S^2}\sum_{\mathbf{k}}\sum_{i,j=1}^{2}\frac{v_{ij}^{\alpha}v_{ji}^{\beta}(n_{\mathbf{k},i} - n_{\tilde{\mathbf{k}},j})}{(E_{\mathbf{k},i} - E_{\tilde{\mathbf{k}},j})(E_{\mathbf{k},i} - E_{\tilde{\mathbf{k}},j} + \hbar\omega + i0_+)} \tag{4.10}$$

where v_{ij}^{α} is the ij-th band component of the velocity operator $\hat{v}_{\alpha}$ along $\alpha = x, y$ cartesian component, $\hbar\mathbf{k}$ is the two-dimensional quasimomentum in graphene, $\tilde{\mathbf{k}} = \mathbf{k} + \mathbf{q}$, n_q is the Fermi occupation number

$$n_{\mathbf{k}} = f(E_{\mathbf{k}}; \mu), \tag{4.11}$$

given by the Fermi function

$$f(\varepsilon; \mu) \equiv \frac{1}{\exp\frac{\varepsilon-\mu}{k_B T} + 1}, \tag{4.12}$$

k_B is the Boltzmann constant, and S is the sample size.

The conductivity formula Eq. (4.10) is the response function on a monochromatic wave in terms of the frequency ω and wavenumber $\mathbf{q}$ of the applied monochromatic electric field. From the quantum mechanical point of view, for an incoming photon of energy $\hbar\omega$ and momentum $\hbar\mathbf{q}$, determined by the factor $(E_{\mathbf{k},i} - E_{\tilde{\mathbf{k}},j} + \hbar\omega + i0_+)$ in Eq. (4.10), we are counting electron transitions from an occupied state to an unoccupied state in the electronic band structure such that the destination is at an energy above the Fermi level, which is determined by the factor $(n_{\mathbf{k},i} - n_{\tilde{\mathbf{q}},j})$.

4.3 Long-wavelength conductivity of graphene

For numerical purposes the formula Eq. (4.10) is computationally intensive, so we apply further approximation. We will assume that the momentum of incoming photons that provoke electronic transition is small compared to that of the electrons. This assumption is called the long-wavelength limit meaning that the wavenumber $\mathbf{q}$ of the applied electromagnetic field is small. We may split the summation $\sum_{i,j}$ in Eq. (4.10) into "intraband" $\sum_{i=j}$ and "interband" $\sum_{i\neq j}$ parts, that is

$$\sum_{i,j=1}^{2} \cdots = \sum_{i=j} \cdots + \sum_{i\neq j} \cdots \tag{4.13}$$

respectively, for ease in derivations later. We use Eq. (4.10) for graphene by substituting the velocity operator components from graphene's hamiltonian Eq. (4.6).

4.3.1 Intraband conductivity

Considering only the intraband terms in Eq. (4.10), where for small $\mathbf{p}$ the fraction $(n_{q,i} - n_{\tilde{q},j})/(E_{q,i} - E_{\tilde{q},j})$ is the derivative of the Fermi function, we find the conductivity to be [50]

$$\sigma_{\alpha\beta}^{\text{intra}}(\omega) = \frac{-ie^2}{\hbar^2(\omega + i0)S} \sum_{\mathbf{k}l} \frac{\partial E_{\mathbf{k}l}}{\partial k_\alpha} \frac{\partial f(E_{\mathbf{k}l};\mu)}{\partial E_{\mathbf{k}l}} \frac{\partial E_{\mathbf{k}l}}{\partial k_\beta} \tag{4.14}$$

where S is the sample area, and $E_{\mathbf{k}l} = (-1)^l \hbar V k = (-1)^l \hbar V \sqrt{k_x^2 + k_y^2}$. It is sufficient to calculate the longitudinal conductivity, due to Eqs. (4.48) and (4.50) namely $\sigma \equiv \sigma_{xx}$, and so

$$\sigma_{xx}^{\text{intra}}(\omega) = \frac{-ie^2}{\hbar^2(\omega + i0)S} \sum_{\mathbf{k}l} \left(\frac{\partial E_{\mathbf{k}l}}{\partial k_x}\right)^2 \frac{\partial f(E_{\mathbf{k}l})}{\partial E_{\mathbf{k}l}} \tag{4.15}$$

Then the expressions for the partial derivatives in terms of k and its components are

$$\begin{aligned}\left(\frac{\partial E_{\mathbf{k}l}}{\partial k_x}\right)^2 &= \hbar^2 v_0^2 \frac{k_x^2}{k^2} \\ \frac{\partial f(E_{\mathbf{k}l})}{\partial E_{\mathbf{k}l}} &= \frac{-\beta e^{\beta[(-1)^l \hbar v_0 k - \mu]}}{(1 + e^{\beta[(-1)^l \hbar v_0 k - \mu]})^2}\end{aligned}$$

which we substitute into Eq. (4.15) to get

$$\begin{aligned}\sigma_{xx}^{\text{intra}}(\omega) &= \frac{-ie^2}{\hbar^2(\omega + i0)S} \sum_{\mathbf{k}l} \hbar^2 v_0^2 \frac{k_x^2}{k^2} \frac{-\beta e^{\beta[(-1)^l \hbar v_0 k - \mu]}}{(1 + e^{\beta[(-1)^l \hbar v_0 k - \mu]})^2} \\ &= \frac{ie^2 v_0^2 \beta}{(\omega + i0)S} \sum_{\mathbf{k}l} \frac{k_x^2}{k^2} \frac{e^{\beta[(-1)^l \hbar v_0 k - \mu]}}{(1 + e^{\beta[(-1)^l \hbar v_0 k - \mu]})^2}\end{aligned}$$

For a large sample, we have high number of states in k-space, so the summation can be changed to an integral,

$$\sum_{\mathbf{k}} \rightarrow \frac{S}{(2\pi)^2} \int dk_x dk_y, \tag{4.16}$$

over k-space.

$$\sigma^{\text{intra}} = \frac{ie^2 v_0^2 \beta}{(2\pi)^2 (w + i0)} \sum_l I_l \tag{4.17}$$

where

$$I_l = \iint dk_x dk_y \frac{k_x^2}{k^2} \frac{e^{\beta[(-1)^l \hbar v_0 k - \mu]}}{(1 + e^{\beta[(-1)^l \hbar v_0 k - \mu]})^2}$$

The two dimensional integral can be converted from Cartesian to polar differential elements, i.e. $dk_x dk_y \rightarrow k\, dk\, d\phi$, where ϕ is polar angle in k-space, and $k_x = k\cos(\phi)$.

$$I_l = \int_0^{2\pi} \int_0^{\infty} k\, dk\, d\phi \cos^2(\phi) \frac{e^{\beta[(-1)^l \hbar v_0 k - \mu]}}{(1 + e^{\beta[(-1)^l \hbar v_0 k - \mu]})^2} \tag{4.18}$$

The integral in ϕ is equal to π, so we are left with

$$I_l = \pi \int_0^\infty dk \frac{k e^{Ak+B}}{(e^{Ak+B}+1)^2} \tag{4.19}$$

where $A \equiv (-1)^l \beta \hbar v_0$, $B \equiv -\mu\beta$.

The integral Eq. (4.19) can be solved by first integrating by parts and then integrating the Fermi-distribution.

$$I_l = \pi \left[\frac{k}{A} \frac{e^{Ak+B}}{e^{Ak+B}+1} - \frac{1}{A^2} \ln\left(e^{Ak+B}+1\right) \right]_0^\infty \tag{4.20}$$

For the case $l = 1$, $A < 0$, and so the exponential terms disappear as $k \to \infty$, and the only terms remaining for this case are

$$\begin{aligned} I_{l=1} &= \pi \left[0 - \left(-\frac{1}{A^2} \ln\left(e^B + 1\right) \right) \right] \\ &= \frac{\pi}{\beta^2 \hbar^2 v_0^2} \ln\left(e^{-\mu\beta}+1\right) \end{aligned} \tag{4.21}$$

For the case $l = 2$, $A > 0$ and Eq. (4.20) can be rearranged to see which terms vanish for $k \to \infty$,

$$I_l = -\pi \left[\frac{k}{A} \frac{e^{-Ak-B}}{(1+e^{-Ak-B})} + \frac{1}{A^2} \ln\left(1+e^{-Ak-B}\right) \right]_0^\infty, \tag{4.22}$$

where the identities

$$\left[\ln\left(e^{Ak+B}+1\right) + (Ak+B-Ak-B) \right]_0^\infty \equiv \left[\ln\left(e^{-Ak-B}+1\right) + Ak \right]_0^\infty \tag{4.23}$$

and

$$\frac{e^P}{e^P+1} - 1 \equiv -\frac{e^{-P}}{1+e^{-P}} \tag{4.24}$$

were used. So for this case,

$$
\begin{aligned}
I_{l=2} &= -\pi\left(0-\left(\frac{1}{A^2}\ln\left(1+e^{-B}\right)\right)\right) &(4.25)\\
&= \frac{\pi}{\beta^2\hbar^2v_0^2}\ln\left(1+e^{\mu\beta}\right) &(4.26)
\end{aligned}
$$

The sum of Eq. (4.21) and Eq. (4.26) is

$$\sum_l I_l = \frac{\pi}{\beta^2\hbar^2v_0^2}\ln\left(2+2\cosh\mu\beta\right)$$

which can be substituted back into Eq. (4.17) giving

$$
\begin{aligned}
\sigma^{\text{intra}} &= \frac{ie^2v_0^2\beta}{(2\pi)^2(\omega+i0)}\frac{\pi}{\beta^2\hbar^2v_0^2}\ln\left(2+2\cosh\mu\beta\right) &(4.27)\\
&= \frac{ie^2\mu}{4\pi(\omega+i0)\hbar^2}\frac{\ln\left(2+2\cosh\mu\beta\right)}{\mu\beta}. &(4.28)
\end{aligned}
$$

The intraband part of conductivity Eq. (4.28) can be observed to have the same form as Drude conductivity Eq. (2.42). Therefore, it is the interband part which is discussed in Sec. 4.3.2 that mathematically improves on the Drude model. Note that in Eq. (4.28) μ and β play the role of plasma frequency ω_P in Drude model conductivity Eq. (2.42). The intraband conductivity Eq. (4.28) is nonzero even at $\mu = 0$ because of the linear dispersion of charge carriers allows intraband transitions near Fermi level, see Eq. (4.14).

4.3.2 Interband conductivity

Now choosing the interband terms from Eq. (4.10) for the interband conductivity we get [50],

$$\sigma_{\alpha\beta}^{\text{inter}}(\omega) = \frac{ie^2\hbar}{S}\sum_{\mathbf{k},l\neq l'}\frac{f(E_{\mathbf{k}l'};\mu)-f(E_{\mathbf{k}l};\mu)}{E_{\mathbf{k}l'}-E_{\mathbf{k}l}-\hbar(\omega+i0)}\times\frac{\langle\mathbf{k}l|\hat{v}_\alpha|\mathbf{k}l'\rangle\langle\mathbf{k}l'|\hat{v}_\beta|\mathbf{k}l\rangle}{E_{\mathbf{k}l'}-E_{\mathbf{k}l}}, \tag{4.29}$$

where using Eq. (4.6) and the canonical commutations between position and momentum operators

$$[\hat{x}, \hat{p}_x] = [\hat{y}, \hat{p}_y] = i\hbar, \tag{4.30}$$

$$[\hat{x}, \hat{p}_y] = [\hat{y}, \hat{p}_x] = 0, \tag{4.31}$$

the velocity operator is obtained as

$$\hat{v}_\alpha = \frac{1}{i\hbar}[\hat{\alpha}, H], \tag{4.32}$$

$$= \frac{v_0}{i\hbar}\left[\sigma_x[\hat{\alpha}, \hat{p}_x] + \sigma_y[\hat{\alpha}, \hat{p}_y]\right], \tag{4.33}$$

$$= v_0\sigma_\alpha, \tag{4.34}$$

and $\hat{\alpha} = \hat{x}$ or $\hat{\alpha} = \hat{y}$ is position operator. We only require the x component due to Eqs. (4.48) and (4.50)thus we only need to calculate σ_{xx}, see Sec. 4.3.3. Note that the summation in Eq. (4.29) imposes due to interband terms that

$$l \neq l' \implies E_{\mathbf{k}l'} = -E_{\mathbf{k}l},$$

meaning that the energy in band 1 is negative of that in band 2 for the same electron crystal momentum, which is henceforth assumed in calculating the terms within the summation in (4.29).

Using the eigenvectors Eqs. (4.8) and (4.9) for the Hamiltonian Eq. (4.6), we get the conjugate brakets

$$\langle \mathbf{k}l' | \hat{v}_x | \mathbf{k}l \rangle = -1^{l} i v_0 k_y / k,$$

$$\langle \mathbf{k}l | \hat{v}_x | \mathbf{k}l' \rangle = -1^{l'} i v_0 k_y / k,$$

the product of whom is

$$\langle \mathbf{k}l | \hat{v}_x | \mathbf{k}l' \rangle \langle \mathbf{k}l' | \hat{v}_x | \mathbf{k}l \rangle = v_0^2 \frac{k_y^2}{k^2} \tag{4.35}$$

Also note that

$$f(-(-1)^l X\,;\mu) - f((-1)^l X\,;\mu) = (-1)^l[f(-X\,;\mu) - f(X\,;\mu)] \tag{4.36}$$

for $l = 1, 2$.

Substituting Eq. (4.35) and Eq. (4.36) into Eq. (4.29) and expanding the sum over l gives

$$\sigma^{\text{inter}} = \frac{ie^2\hbar}{S}\sum_{\mathbf{k}l}\frac{f(-E_{\mathbf{k}l}\,;\mu) - f(E_{\mathbf{k}l}\,;\mu)}{-2E_{\mathbf{k}l} - \hbar(\omega + i0)}\cdot v_0^2\frac{k_y^2}{k^2}\cdot\frac{1}{-2E_{\mathbf{k}l}} \tag{4.37}$$

$$= \frac{ie^2\hbar}{S}\sum_{\mathbf{k}l}\frac{f(-(-1)^l\hbar v_0 k\,;\mu) - f((-1)^l\hbar v_0 k\,;\mu)}{-2(-1)^l\hbar v_0 k - \hbar(\omega + i0)}\cdot v_0^2\frac{k_y^2}{k^2}\cdot\frac{1}{-2(-1)^l\hbar v_0 k} \tag{4.38}$$

$$= \frac{ie^2\hbar}{S}\sum_{\mathbf{k}l}\frac{f(-\hbar v_0 k\,;\mu) - f(\hbar v_0 k\,;\mu)}{2(-1)^l\hbar v_0 k + \hbar(\omega + i0)}\cdot v_0^2\frac{k_y^2}{k^2}\cdot\frac{1}{2\hbar v_0 k} \tag{4.39}$$

$$= \frac{ie^2\hbar}{S}\sum_{\mathbf{k}} v_0^2\frac{k_y^2}{k^2}\cdot\frac{f(-\hbar v_0 k\,;\mu) - f(\hbar v_0 k\,;\mu)}{2\hbar v_0 k}\left\{\frac{1}{2\hbar v_0 k + \hbar(\omega + i0)} + \frac{1}{-2\hbar v_0 k + \hbar(\omega + i0)}\right\} \tag{4.40}$$

The summation can be changed to an integral $\sum_{\mathbf{k}} \to \frac{S}{(2\pi)^2}\int dk_x dk_y$ over k-space. Then integrating in polar form using $\mathbf{dk} = kdkd\phi$, and then using $\int_0^{2\pi}\sin^2(\phi)d\phi = \pi$, we have

$$\sigma^{\text{inter}} = \frac{ie^2\hbar}{4\pi}\int_0^\infty kdkv_0^2\cdot\frac{f(-\hbar v_0 k\,;\mu) - f(\hbar v_0 k\,;\mu)}{2\hbar Vk}\left\{\frac{1}{2\hbar v_0 k + \hbar(\omega + i0)} + \frac{1}{-2\hbar v_0 k + \hbar(\omega + i0)}\right\}$$

Let us define unitless energy $K \equiv \hbar v_0 k/\mu$, the Fermi-Dirac distribution function of unitless energy

$$N(K) \equiv f(\mu K;\mu) = \{1 + e^{\mu\beta(K-1)}\}^{-1}, \tag{4.41}$$

and unitless frequency $\Omega \equiv \hbar\omega/\mu$. Then

$$\sigma^{\text{inter}} = \frac{ie^2}{4\pi\hbar}\int_0^\infty KdK \cdot \frac{N(-K) - N(K)}{2K}\left\{\frac{1}{\Omega - 2K} + \frac{1}{\Omega + 2K}\right\} \tag{4.42}$$

$$= \frac{ie^2}{8\pi\hbar}\int_0^\infty dK[N(-K) - N(K)]\left\{\frac{1}{\Omega - 2K} + \frac{1}{\Omega + 2K}\right\} \tag{4.43}$$

The integral is difficult to numerically calculate for due to pole at $K = \Omega/2$ in the integrand, so we may split the integral into a sum of two integrals, one which with pole at $K = \Omega/2$ but analytically simplifiable, and another without the pole which cannot be simplified analytically. We can subtract and add a factor $G(\Omega/2)$ in the integrand [40] to write

$$\sigma^{\text{inter}} = \frac{ie^2}{8\pi\hbar}\int_0^\infty dKG(K)\left\{\frac{1}{\Omega - 2K} + \frac{1}{\Omega + 2K}\right\} \tag{4.44}$$

$$= \frac{ie^2}{8\pi\hbar}\int_0^\infty dK[G(K) - G(\Omega/2)]\frac{2\Omega}{\Omega^2 - 4K^2} + \frac{ie^2}{8\pi\hbar}G(\Omega/2)\int_0^\infty dK\frac{2\Omega}{\Omega^2 - 4K^2}, \tag{4.45}$$

where

$$G(K) = N(-K) - N(K) = \frac{\sinh K}{\cosh \mu\beta + \cosh K}. \tag{4.46}$$

is the difference of Fermi-functions. The first integrand in Eq. (4.45) has no pole for $K \in [0, \infty)$. The second integral in Eq. (4.45) can be analytically evaluated to give $-i\pi/2$, simplifying Eq. (4.45) to

$$\sigma^{inter}(\Omega) = \frac{e^2}{4\hbar}\left[G(\Omega/2) - \frac{4\Omega}{i\pi}\int_0^\infty dK\frac{G(\varepsilon) - G(\Omega/2)}{\Omega^2 - 4K^2}\right]. \tag{4.47}$$

4.3.3 Conductivity tensor components

Note that we have in the long-wavelength limit $\mathbf{q} \to 0$ that

$$\sigma_{yy} = \sigma_{xx}, \tag{4.48}$$

due to the fact that

$$\int_0^{2\pi} \sin^2(\phi)d\phi = \int_0^{2\pi} \cos^2(\phi)d\phi \tag{4.49}$$

holds true in Eq. (4.18) for intraband term, and in Eq. (4.40) for interband term, making the expression for σ_{xx} identical to that of σ_{yy}.

We also find that

$$\sigma_{xy} = \sigma_{yx} = 0, \tag{4.50}$$

due to the fact that the factor

$$\int_0^{2\pi} \sin(\phi)\cos(\phi)d\phi = 0 \tag{4.51}$$

would occur in Eqs. (4.14) and (4.29) for the offdiagonal components of conductivity.

4.4 Parameters controlling conductivity

The parameters in our conductivity model are chemical potential μ and temperature T affecting the optical properties of graphene, independent of the shape and size of graphene sample. The conductivity formula can be written so that these two parameters appear only as the quotient $\mu\beta = \mu/k_BT$, where k_B is the Boltzmann constant. For practicality reasons, the chemical potential $\mu(n_0, T)$ can be written as a function of charge carrier concentration n_0, and temperature T, that is, we have for the electron density[87],

$$n_0 = \frac{2}{\pi(\hbar v_0)^2} \int_0^{\infty} \varepsilon[f_0(\varepsilon - \mu) - f_0(\varepsilon + \mu)]d\varepsilon, \tag{4.52}$$

where

$$f_0(\varepsilon) = f(\varepsilon; 0). \tag{4.53}$$

The charge carrier density n_0 can be controlled by doping and gating [58, 87] graphene. One experimental way of doping electrons into the graphene is by hot electron plasmons near the graphene [106].

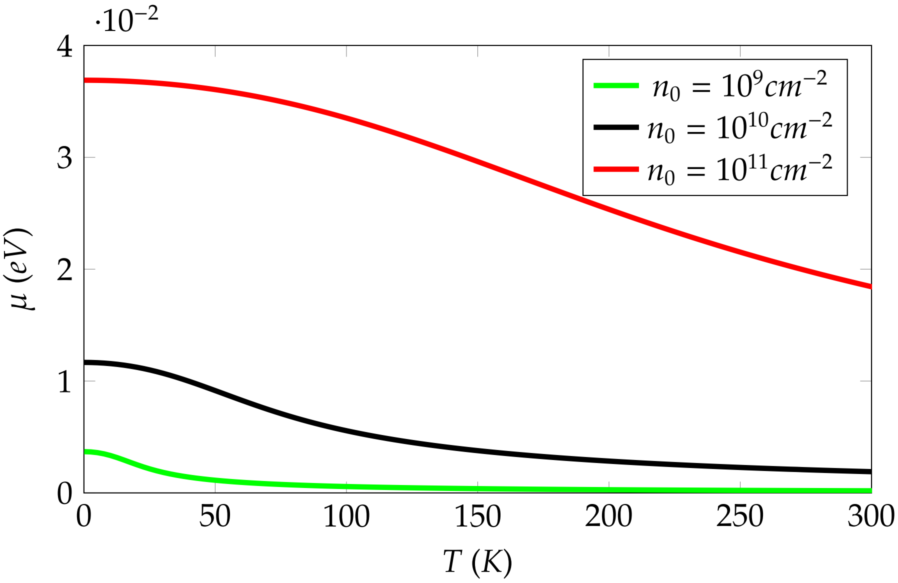

Figure 4.2: Chemical potential of graphene modelled as a function of temperature at different carrier densities.

In Fig. 4.2 we show the temperature dependence of chemical potential of graphene for various charge carrier concentrations. Chemical potential increases with charge carrier concentration n_0 as more electronic states are filled up for lower energies. On the other hand chemical potential decreases with temperature, since charge carriers near Fermi-level are lifted to higher energies and the energy of the lowest unoccupied state decreases.

Fig. 4.3 shows the conductivity spectrum of graphene for various temperatures.

For numerical purposes, the Newton-Raphson method can be employed using Eq. (4.52) to acquire a function for chemical potential $\mu(T)$ Fig. 4.3 at a particular n_0. This can then be used with the sum of Eq. (4.28) and Eq. (4.47) to calculate conductivity $\sigma(\omega)$.

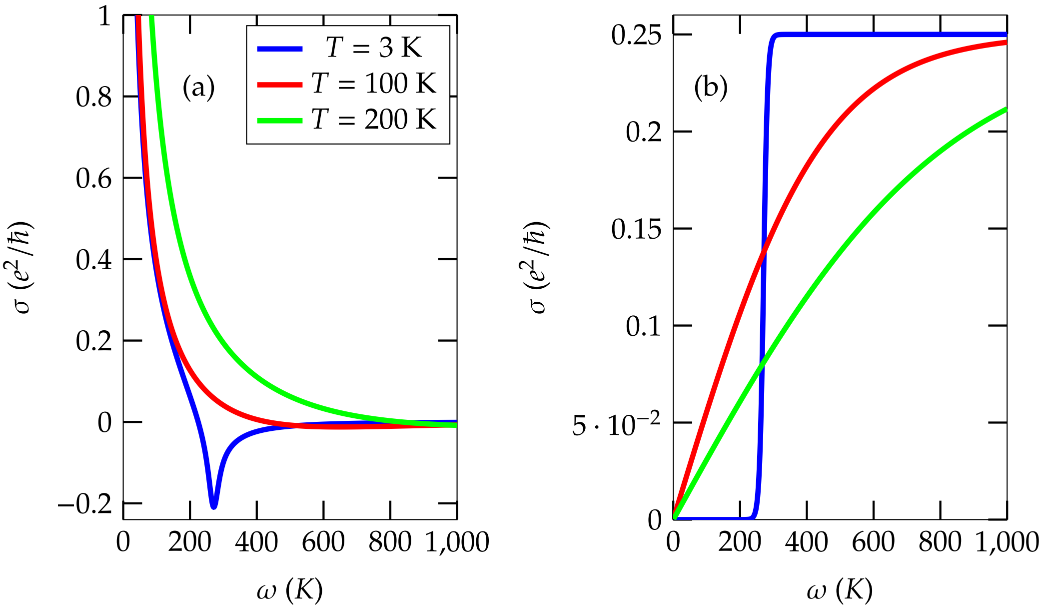

Figure 4.3: Dynamical frequency-dependent conductivity of graphene at different temperatures (right).

4.5 Conductivity at zero temperature

At zero temperature $T/\mu \to 0$, so that the product $\mu\beta$ becomes infinitely large. The second fraction of intraband conductivity in Eq. (4.28) becomes unity so that

$$\sigma^{\text{intra}} = \frac{ie^2}{4\pi(\Omega + i0)\hbar}. \tag{4.54}$$

The difference of Fermi-function becomes a Heaviside step function, that is

$$f(-K) - f(K) \xrightarrow{\mu\beta \longrightarrow \infty} \Theta(K), \tag{4.55}$$

so that the integral for interband conductivity in Eq. (4.47) can be readily analytically evaluated for zero temperature. The interband conductivity becomes [50],

$$\sigma^{\text{inter}} = \frac{e^2}{4\hbar}\left(\Theta\left(|\Omega| - 2\right) - \frac{i}{\pi}\ln\left|\frac{2+\Omega}{2-\Omega}\right|\right). \tag{4.56}$$

At zero temperature, the real part of conductivity is a step function centred at $\hbar\omega = 2\mu$. The chemical potential lies exactly at the Fermi level at this temperature and no charge carriers occupy energy states above the Fermi level. As the real part of conductivity is what makes the imaginary part of permittivity, the losses appear due to interband transition of charge carriers caused by photons with frequencies satisfying $\hbar\omega > 2\mu$. We will see in Chapter 4 this interband loss feature manifests as temporal loss in the dispersion relation of TE mode in graphene.

CHAPTER 5

SPPs in graphene in the long-wavelength limit

This chapter has been adapted from the published paper in Phys. Rev. B [107].

After acquiring a long-wavelength ($q \to 0$) formula for the optical conductivity as function for optical frequency ω, we are now in a position to employ it to present an analysis of the electromagnetic modes along an infinite homogeneous graphene sheet.

The dispersion results of SPP in the two polarisations have qualitatively different features so they will be presented in different sections. TM SPP results, which will be presented in Sec. 5.2 are not new with features similar to the case of an infinitesimally thin metallic sheet. TE mode presented in Sec. 5.3, however, are not restricted in the range of real frequency due to the interband conductivity of graphene, as opposed to what was reported earlier in the literature [50], and shows features deriving from the conductivity spectrum. As we will discover, in the case of TE polarisation, the electromagnetic modes have a lower frequency threshold, below which we find solutions that decay exponentially toward the graphene sheet. Above this frequency threshold, the modes are decaying as we go away and are evanescent. Since the long-wavelength conductivity can be written as a function of the frequency and temperature expressions $\hbar\omega/\mu$ and $\mu\beta$ respectively, we may define unitless frequency, normalised with respect to chemical potential μ as,

$$\Omega \equiv \frac{\hbar}{\mu}\omega, \tag{5.1}$$

same as introduced in Sec. 4.3.2. Similarly we may also normalise other variables such as normal and in-plane wavenumbers of light respectively,

$$K \equiv \frac{\hbar}{\mu}ck, \quad \mathbf{Q} \equiv \frac{\hbar}{\mu}c\mathbf{q} \tag{5.2}$$

and temperature as

$$\mu\beta \equiv \frac{\mu}{k_B T}. \tag{5.3}$$

These unitless variables will allow us a qualitative examination of the electromagnetic modes in the system, whilst accounting for the change in the chemical potential and temperature simultaneously in the combined parameter $\mu\beta$.

Please also note that the graphene structures will conventionally lie in xy-plane so that z direction is normal to graphene surface, with no propagation of electromagnetic solution along y-direction, meaning that

$$\mathbf{Q} = \begin{pmatrix} Q \\ 0 \\ 0 \end{pmatrix}, \tag{5.4}$$

and the total wavenumber of light is

$$\begin{pmatrix} Q \\ 0 \\ K \end{pmatrix}. \tag{5.5}$$

We would further like to remind the reader that in our analysis we treat the in-plane wavenumber to be real $Q \in \mathbb{R}$, whilst the frequency is complex $\Omega \in \mathbb{C}$, as already mentioned at the begining of Ch. 3.

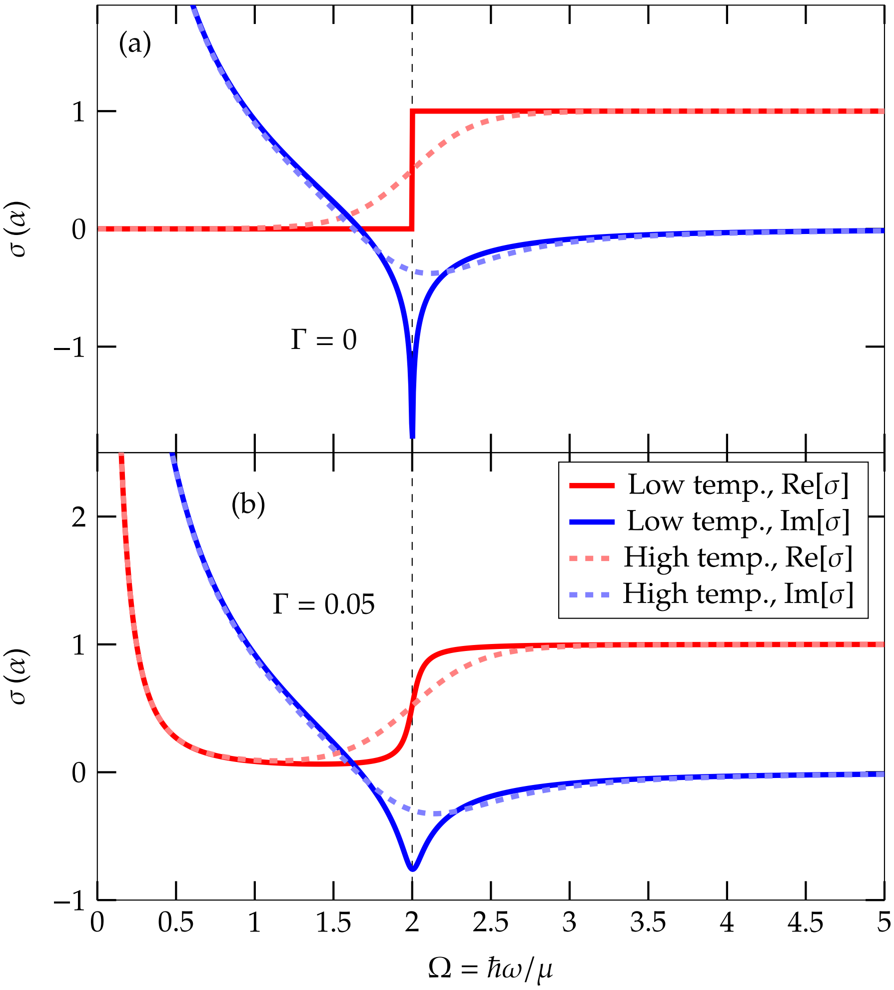

Figure 5.1: Dependence of Re[σ] and Im[σ] on frequency Ω (a) with and (b) without phenomenological damping Γ, for low temperature $\mu\beta = 10^5$ and high temperature $\mu\beta = 10$. Vertical black dashed line is at frequency twice the chemical potential, $\Omega = 2$. The conductivity axes are plotted in units of the fine-structure constant α.

The conductivity can be thus written in terms of Ω and $\mu\beta$ as

$$\begin{aligned}\sigma_{\text{surf}} &= \sigma\left(\frac{\hbar\omega}{\mu}, q \to 0; \mu\beta\right)\\ &= i\alpha\left\{\frac{2\ln(2+2\cosh\mu\beta)}{\mu\beta(\Omega+i\Gamma)} + \int_0^\infty dE\,[N(-E)-N(E)]\left(\frac{1}{\Omega+i\Gamma-2E}+\frac{1}{\Omega+i\Gamma+2E}\right)\right\},\end{aligned} \tag{5.6}$$

where Γ is a phenomenological damping, and $\alpha = e^2/\hbar$ is the fine-structure constant. Fig. 5.1 illustrates the conductivity spectrum in the long-wavelength limit.

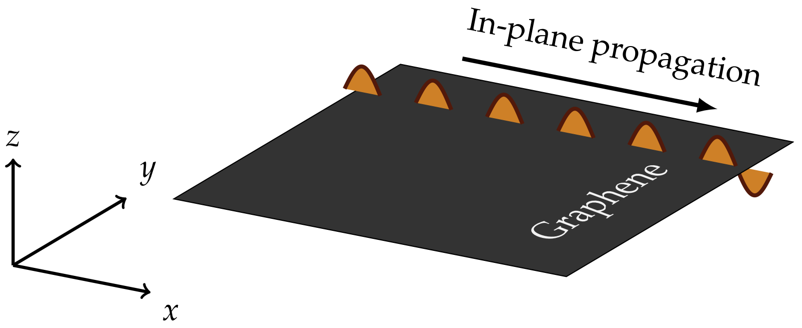

Figure 5.2: Schematic of an infinite homogeneous graphene sheet in vacuum showing direction of SPP propagation projected along graphene surface.

Note that for $\Omega \in \mathbb{R}$ and $\Gamma = 0$, there is a dip in $\mathrm{Im}[\sigma]$ at $\Omega = 2$ for low temperature $\mu\beta = 10^5$.

5.1 Structure and secular equations for SPP modes

The structure, depicted in Fig. 5.2, similar to the metallic sheet in Ch. 3, is given by

$$\varepsilon(\Omega; z) = \begin{pmatrix} \varepsilon_{\|}(\Omega; z) & 0 & 0 \\ 0 & \varepsilon_{\|}(\Omega; z) & 0 \\ 0 & 0 & 1 \end{pmatrix}, \tag{5.7}$$

where the in-plane permittivity is

$$\varepsilon_{\|}(\Omega; z) = 1 + \frac{i2\sigma(\Omega)}{\Omega}\delta(z), \tag{5.8}$$

we are using the normalised variables, and the long-wavelength conductivity $\sigma(\Omega)$ of graphene as discussed in Ch. 4, and we have absorbed a factor of 4π into the conductivity expression Eq. (5.6).

The secular equations for TM and TE polarisations of the planar graphene structure modelled by Eq. (5.8) can be written using Eq. (3.21) and Eq. (3.34), respectively, in terms of normalised variables as

$$\Omega + K\,\sigma(\Omega) = 0 \quad \text{(TM)}, \tag{5.9}$$

$$K + \Omega\,\sigma(\Omega) = 0 \quad \text{(TE)}, \tag{5.10}$$

where $K = \sqrt{\Omega^2 - Q^2}$ is component of the wavenumber normal to the graphene surface and is a function of both Ω and Q.

In the following sections, the system is examined at **low temperature** $\mu\beta = 10^5$, and **high temperature** $\mu\beta = 10$ setting. For example, a chemical potential of $\mu = 0.2eV$ which is a realistic chemical potential [108], the low temperature setting corresponds to $\frac{\mu}{10^5 k_B} \approx 0.02K$, and the high temperature setting corresponds to $\frac{\mu}{10 k_B} \approx 232K$.

5.2 SPP in TM polarisation

The dispersion result of the transverse magnetic polarisation in planar graphene is similar to the result for Drude metal (see Fig. 3.2). The real frequency lies well below the light line $\Omega = Q$, as shown in Fig. 5.3(a)(b). Graphene conductivity is dominated by the Drude-like part for smaller (than interband) optical frequencies. For small temperatures, both $|\mathrm{Im}[\Omega]|$ and $\mathrm{Re}[K]$ are proportional to $e^{-\mu\beta}$. For increasing temperature, $|\mathrm{Im}[\Omega]|$ increases due to charge carrier holes forming below the Fermi level as some charge carrers are given energy above Fermi level. Thus the count of interband absorbtions is altered within the conduction band, increasing losses. Note that the Drude model is not an accurate model for very small frequencies, and along with the secular equation Eq. (5.9) it results a superluminal dispersion for Q very close to zero which is not discernable in Fig. 5.3(a)(b).

The real part of frequency approaches an asymptote for large Q, which is dependent on $\mu\beta$ and can be analytically obtained from Eq. (5.9) in the limit $Q \to \infty$ as the real part of solution to the equation $\sigma(\Omega) = 0$. This asymptote is similar to the one for the dispersion of dielectric-metal interface with Drude conductivity in Sec. 2.7.

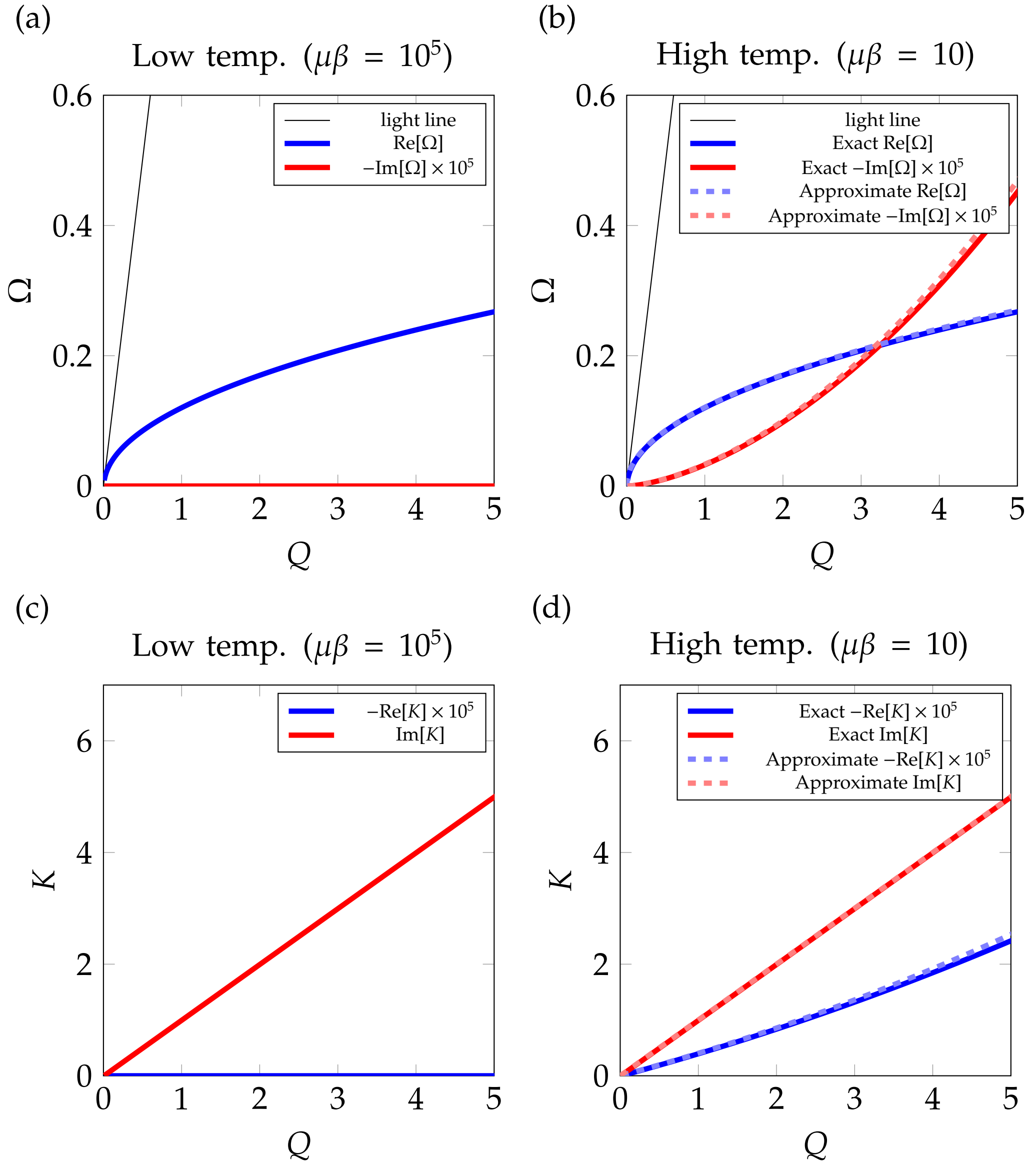

Figure 5.3: Solutions to TM secular equation as real and imaginary Ω (a), (b) as a function of real in-plane wavenumber Q, without phenomenological damping $\Gamma = 0$. The normal component of wavenumber K (c), (d) vs Q. Left column (a), (c) are for low temperature setting, and right column (b), (d) are for high temperature setting. Im[Ω] and Re[K] are scaled by $\times 10^5$ as stated in the legend. Exact curves are calculated using Eq. (5.9), and approximate curves are calculated using Eqs. (5.13) and (5.14).

For the low temperature case, the propagation of light is parallel to the graphene surface since Re[K] ≈ 0 as shown in Fig. 5.3(c). When the temperature is increased, we have Re[K] ≤ 0 as shown in Fig. 5.3(d), meaning that propagation is slightly towards but mostly parallel to the conducting graphene surface. This slightly slanted propagation due to the increase in interband absorption loss increasing for frequencies lower than Re[Ω] = 2 corresponding to increase in real part of the conductivity as shown in Fig. 5.1(a) at high temperature. Change in $\mu\beta$ does not affect real frequency for the low temperature and high temperature settings chosen in Fig. 5.3(a) and Fig. 5.3(b). However, for higher temperatures ($\mu\beta < 10$) as shown in Fig. 5.4, the real part of frequency shows increase determined by the temperature dependent factor Ω_0 in the intraband term of conductivity in Eq. (5.6), where

$$\Omega_0 = 2\alpha \ln(2 + 2\cosh \mu\beta)/(\hbar\beta). \tag{5.11}$$

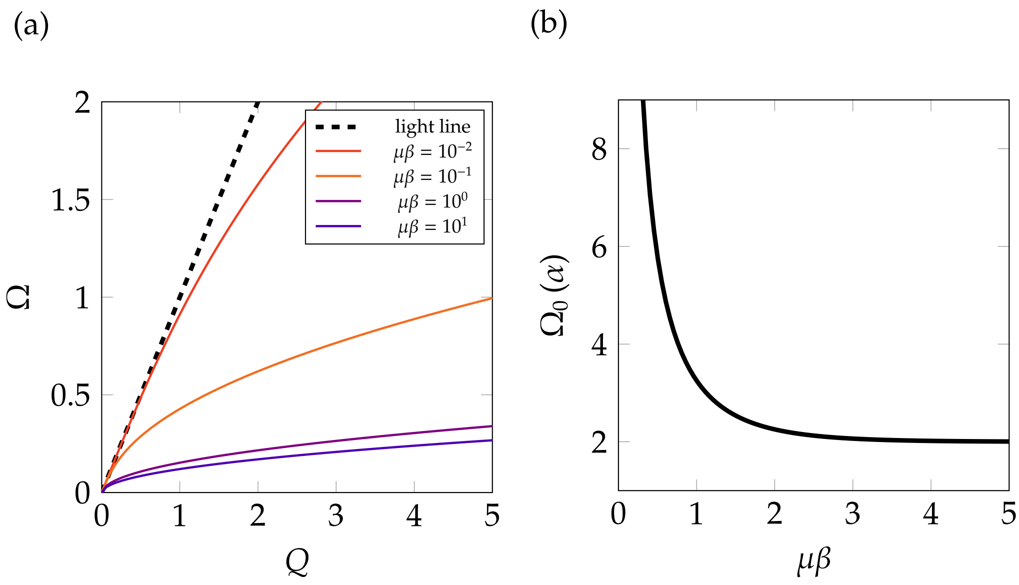

Figure 5.4: (a) Real part of the frequency dispersion of TM SPP mode for different temperatures. (b) Dependence of Ω_0 factor in intraband term on $\mu\beta$ showing that significant change occurs for high temperatures ($\mu\beta \to 0$).

5.2.1 Approximation from dominance of intraband conductivity

Since the conductivity is dominated by its intraband term in the frequency range of the TM mode, that is

$$\sigma \approx \frac{i\Omega_0}{\Omega}, \tag{5.12}$$

where Ω_0 is given in Eq. (5.11), $\Gamma = 0$, we may obtain an insightful, approximate, but explicit expression for the dispersion relation for complex frequency,

$$\Omega(Q) \approx \sqrt{\Omega_0 Q} - iQ\sigma'/2, \tag{5.13}$$

$$K(Q) \approx -\sqrt{\Omega_0 Q}\sigma'/2 + iQ, \tag{5.14}$$

where σ' (σ'') is the real (imaginary) part of the conductivity and $Q >> \Omega_0$ (see Appendix B for details). Thus, the real part of frequency has square-root dependence for frequencies smaller than interband $\Omega = 2$ but also larger and away from pole in Drude conductivity at $\Omega = 0$.

5.2.2 Mode field profile

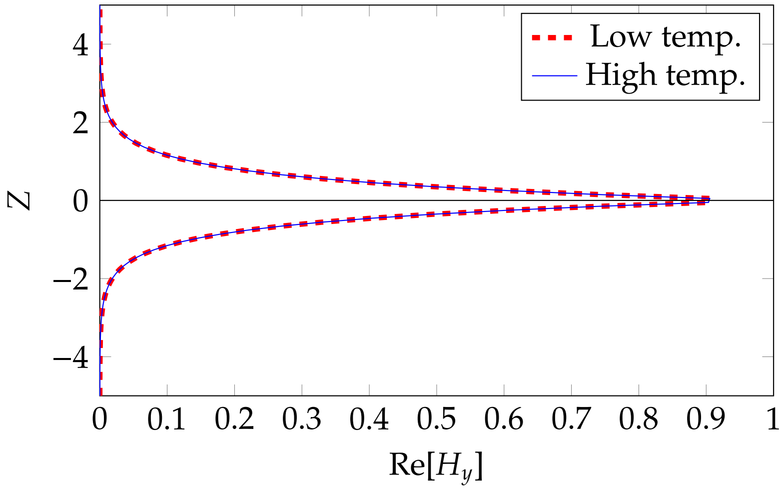

Figure 5.5: Mode field profile across the graphene interface for TM SPP mode for $Q = 2$, for low temperature ($\mu\beta = 10^5$) and high temperature ($\mu\beta = 10^5$) settings.

The plot of normal wavenumber K in Fig. 5.3(c)(d), of its real and imaginary components, shows that the field profile of the SPP mode is decaying away from the graphene as $\mathrm{Im}[K] > 0$, but propagating along and slightly toward the graphene sheet since $-Q \ll \mathrm{Re}[K] < 0$.

The TM SPP mode field profile decays away from the graphene sheet as shown in Fig. 5.5 by the amplitude of the H_y component of the magnetic field strength as a function of normalised z-component of position Z, defined using $kz \equiv KZ$.

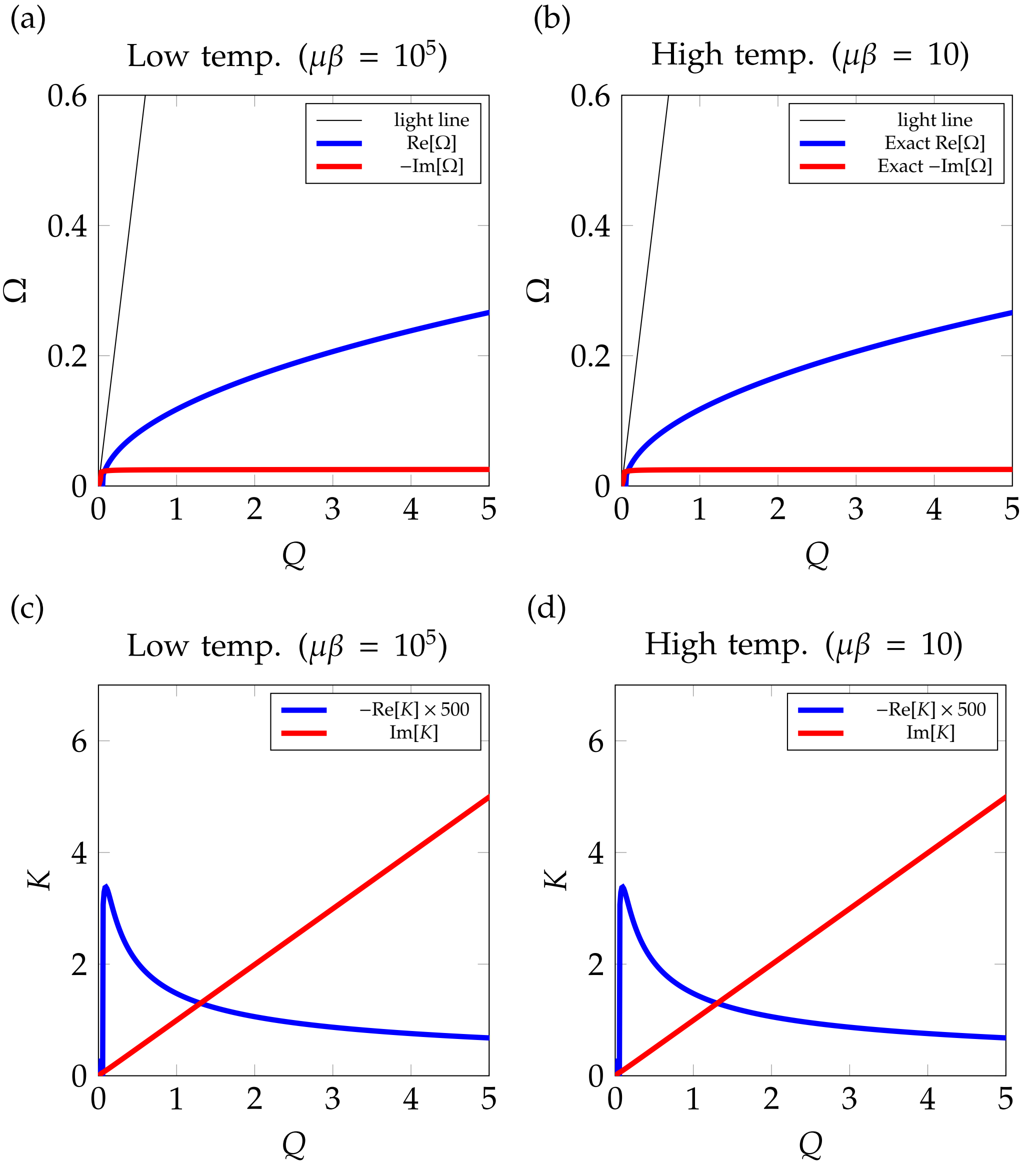

Figure 5.6: Solutions to TM secular equation as real and imaginary Ω (a), (b) as a function of real in-plane wavenumber Q, with non-zero phenomenological damping $\Gamma = 0.05$. The normal component of wavenumber K (c), (d) vs Q with $\Gamma = 0.05$. Left column panels (a), (c) are for low temperature setting, and right column panels (b), (d) are for high temperature setting. Re[K] is scaled by ×500 as stated in the legend. Curves are calculated using Eq. (5.9).

Change in temperature does not have a noticeable effect on the profile between Fig. 5.5(a) and Fig. 5.5(b) which is understandable from Fig. 5.3(c) and Fig. 5.3(d) where the spatial decay rate Im[K], is unaffected by temperature, and Re[K], is comparatively five orders of magnitude smaller.

5.2.3 SPP with phenomenological damping included

We show the SPP dispersion relation with a nonzero phenomenological damping $\Gamma \neq 0$. Although the value chosen here is $\Gamma = 0.05$ to illustrate the qualitative effect on SPP dispersion, the actual value for damping for graphene has been reported in [109] to be about $\mu\Gamma_{\text{intra}} = 0.0658eV$ for intraband conductivity and $\mu\Gamma_{\text{inter}} = 0.00054851eV$ for interband.

Figures 5.6(a) and 5.6(b) show the dispersion of TM SPP mode for $\Gamma = 0.05$. In this case, we observe that, compared to the case of $\Gamma = 0$, $-\text{Im}[\Omega]$ is mainly lifted up by $\Gamma/2$ throughout the range of Q. Whereas $\text{Im}[K]$, shown as red curves in Figs. 5.6(e) and 5.6(f), is unchanged compared to the case of $\Gamma = 0$ (Fig. 5.3), $\text{Re}[K]$, shown as blue curves in the same figures, changes its behaviour and its values significantly, increasing fast around $Q = 0$ and then gradually decreasing with Q. Overall, the phenomenological damping introducing proportional temporal damping in the SPP mode, whilst reducing wavelength normal to graphene (increasing $\text{Re}[K]$), meaning that SPP wavefronts are more parallel to the sheet for fixed Q.

5.3 SPP in TE polarisation

This polarisation provides a more interesting dispersion in graphene. In the TE polarisation, the only nonzero component of electric field is transverse to the propagation direction but parallel to graphene plane, and the dispersion curve is certainly dissimilar from the TM case. Although this mode is an electromagnetic mode in graphene [50], we refrain from referring to this as a “surface plasmon polariton” as there are no charge density oscillations since

$$\nabla \times \begin{pmatrix} 0 \\ E_y \\ 0 \end{pmatrix} = 0, \tag{5.15}$$

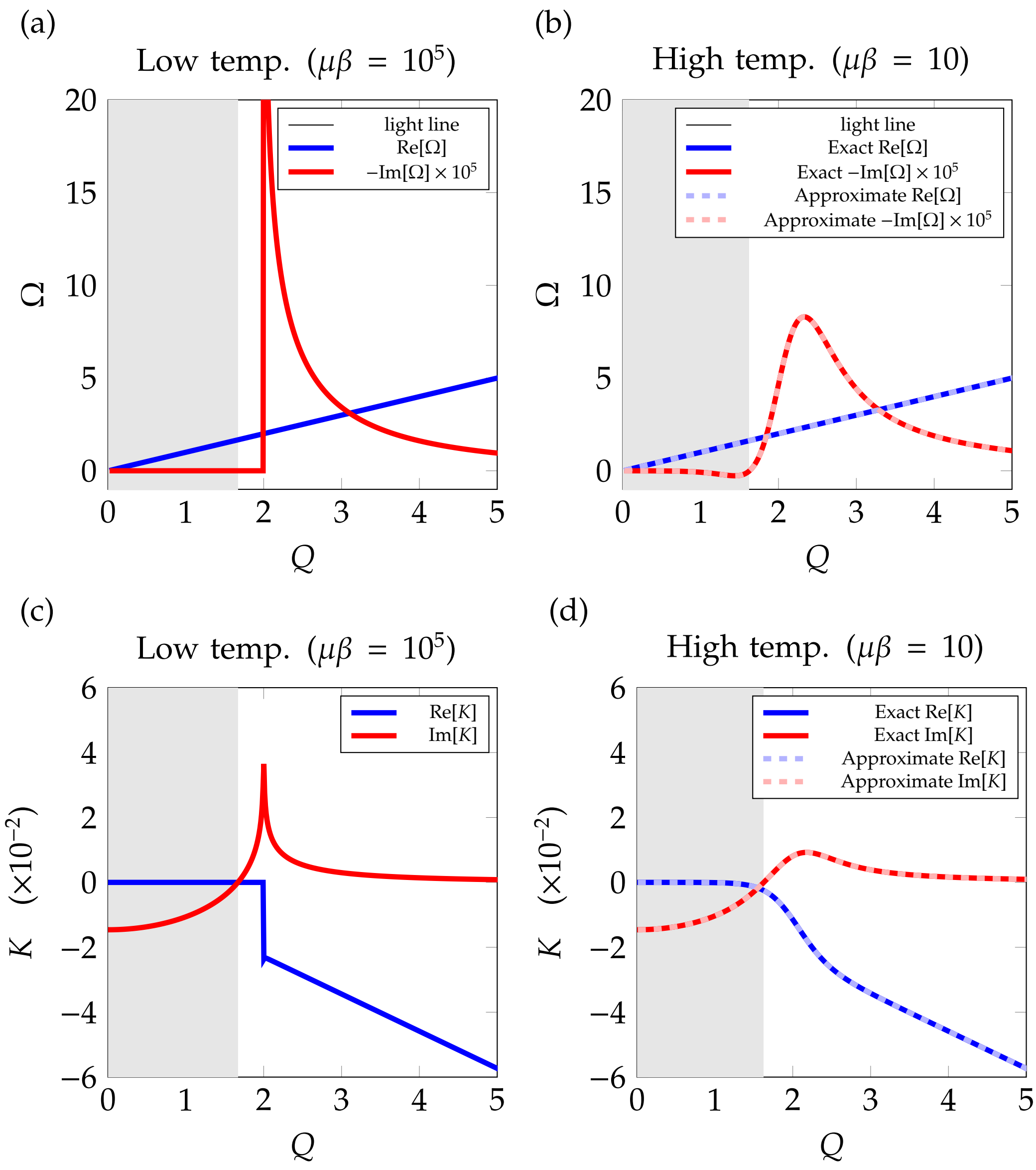

Figure 5.7: Solutions to TE secular equation as real and imaginary Ω (a), (b) as a function of real in-plane wavenumber Q, without phenomenological damping $\Gamma = 0$. The normal component of wavenumber K (c), (d) vs Q. Left column panels (a), (c) are for low temperature setting, and right column panels (b), (d) are for high temperature setting. Im[Ω] is scaled by $\times 10^5$ as stated in the legend. Exact curves are calculated using Eq. (5.10), and approximate curves are calculated using Eqs. (5.17) and (5.17). Grey regions represent positive Im[Ω] > 0.

in this polarisation. We instead refer to the mode as just TE electromagnetic mode. Please note that non-zero current density is possible along y-direction (see Fig. 5.2) with a zero charge density. Note also that σ is not real for $\Omega > 2$.

The real part of frequency of the mode is not asymptotically restricted, but is close to the light line $\Omega = Q$, appearing identical to it in with respect to the scale of vertical axes in Fig. 5.7(a)(b). In order to exaggerate features in real part of frequency, which cannot be seen in Fig. 5.7(a)(b) due to real part of frequency being very close to the light line, $\mathrm{Re}[\Omega - Q]$ has also been calculated in Fig. 5.8. Although $\mathrm{Re}[\Omega] - Q > 0$ in Fig. 5.8 for $Q \gtrapprox 2$, so that the real part of the frequency is above the light line, this is not unphysical. To understand why, please be reminded that $\Omega, K \in \mathbb{C}$ and $Q \in \mathbb{R}$ in Eq. (5.10). To determine physicality of TE mode in this region, we observe that the mode can be an evanescent profile with respect to normal direction. Observe that the expression for the out-of-plane wavenumber can be written in terms of the real and imaginary parts of frequency,

$$K = \sqrt{\Omega^2 - Q^2} = \sqrt{\mathrm{Re}[\Omega]^2 - \mathrm{Im}[\Omega]^2 - Q^2 + 2i\mathrm{Re}[\Omega]\mathrm{Im}[\Omega]}, \tag{5.16}$$

implying that we ought to look for $\mathrm{Im}[K] > 0$ in Fig. 5.7(c)(d) as evidence to the evanescent nature of this mode. (Note that the evanescent nature in the TM case is obvious because in that case the real part of frequency is sufficiently and well below from the frequency of the light line.)

$|\mathrm{Im}[\Omega]|$ is around 5 orders of magnitude smaller than real frequency $\mathrm{Re}[\Omega]$, but in this polarisation, 3 to 4 orders of magnitude smaller than $|\mathrm{Re}[K]|$. The solutions with $\mathrm{Im}[\Omega] > 0$ shown in Fig. 5.7 and Fig. 5.8 are actually physical because their exponential growth with respect to time is compensated with the decaying field profile with respect to normal direction in space toward the graphene, noting the wavefront is slightly tilted toward the graphene.

5.3.1 Small conductivity approximation

Using the fact that conductivity is small $|\sigma| \ll 1$ (as it has a factor of fine-structure constant α) for frequencies away from $\mathrm{Re}[\Omega] = 0$ due to a factor of small fine-structure constant, we obtain the following approximation

$$\Omega(Q) \approx Q + iQ\sigma'\sigma'', \tag{5.17}$$

$$K(Q) \approx -Q\sigma' - iQ\sigma'', \tag{5.18}$$

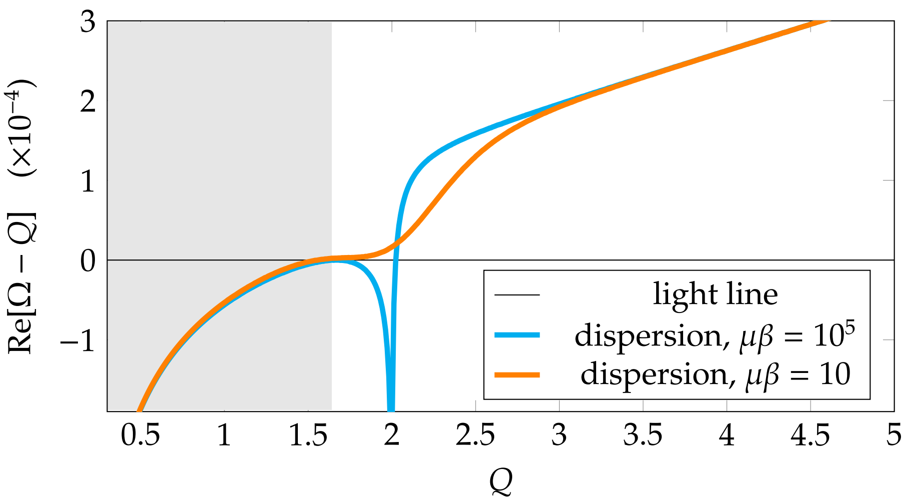

Figure 5.8: Dispersion of the TE mode in a homogeneous graphene with real frequency plotted as a difference from in-plane wavenumber to demonstrate that dispersion is below the light line for $Q < 2$ but above the light line for $Q \gtrsim 2$. Grey region approximately (since it changes slightly with temperature) indicates solutions where $\mathrm{Im}[\Omega] > 0$.

assuming the frequency is away from the Drude pole in conductivity at $\Omega = 0$ (see Appendix B for details). The approximations for explicit Q-dependence of Ω and K in Eqs. (5.17) and (5.18) are plotted as dashed lines in Fig. 5.7(b) and Fig. 5.7(d), respectively, evidently close to the exact dispersion curves. $\mathrm{Re}[\Omega]$ is simply approximated as the light line, but $\mathrm{Im}[\Omega]$ is proportional to $\sigma'\sigma''$ making the peak at $\Omega = 2$ asymmetric. The electronic dynamics related to this asymmetry are discussed in Sec. 5.4. The fact that $\mathrm{Re}[K] \propto \sigma'$ means that the direction of the wavefront around graphene directly depends on its optical absorption. Since K is two orders of magnitude smaller than Q, the wavefront is close to being normal to graphene plane. The spatial decay of field profile in normal direction, however, is $\mathrm{Im}[K] \propto \sigma''$ meaning that the decay is determined by the competition between the intraband and interband electronic transitions in the graphene.

5.3.2 Mode field profile

The mode field profile for the TE polarisation has more variety as parameters are changed, compared to the TM polarisation. Let us define $\Omega^{\mathrm{TE}}_{\mathrm{low}} \in \mathbb{R}$ as

$$K + \Omega^{\mathrm{TE}}_{\mathrm{low}}\, \sigma(\Omega^{\mathrm{TE}}_{\mathrm{low}}) = 0, \tag{5.19}$$

that is, the frequency when $\mathrm{Im}[\Omega] = 0$ in the dispersion Eq. (5.10) of TE mode. For frequencies below the $\Omega^{\mathrm{TE}}_{\mathrm{low}}$, the field is exponentially growing away from graphene as shown in Fig. 5.9(a) for $Q = 1$, where temperature seems to have little effect on the spatial dependence, also shown by the lack of difference in $\mathrm{Im}[K]$ between Fig. 5.7(c) and Fig. 5.7(d) at $Q = 1$.

The insensitivity to change in temperature is also present above frequency $\Omega^{\mathrm{TE}}_{\mathrm{low}}$ for solutions, for example in Fig. 5.9(b) for $Q = 1.8$, although the field profile is spatially decaying as $\mathrm{Im}[K]$ has become positive at this Q. The effect of temperature on the spatial field profile becomes pronounced near $\Omega = 2$, as shown in Fig. 5.9(c) for $Q = 2.002$ as the spatial decay of mode normal to graphene is stronger for low temperature than for higher temperature. The mode is spatially more confined to graphene for lower temperatures. Generally, however, the TE mode is much less confined than the TM mode.

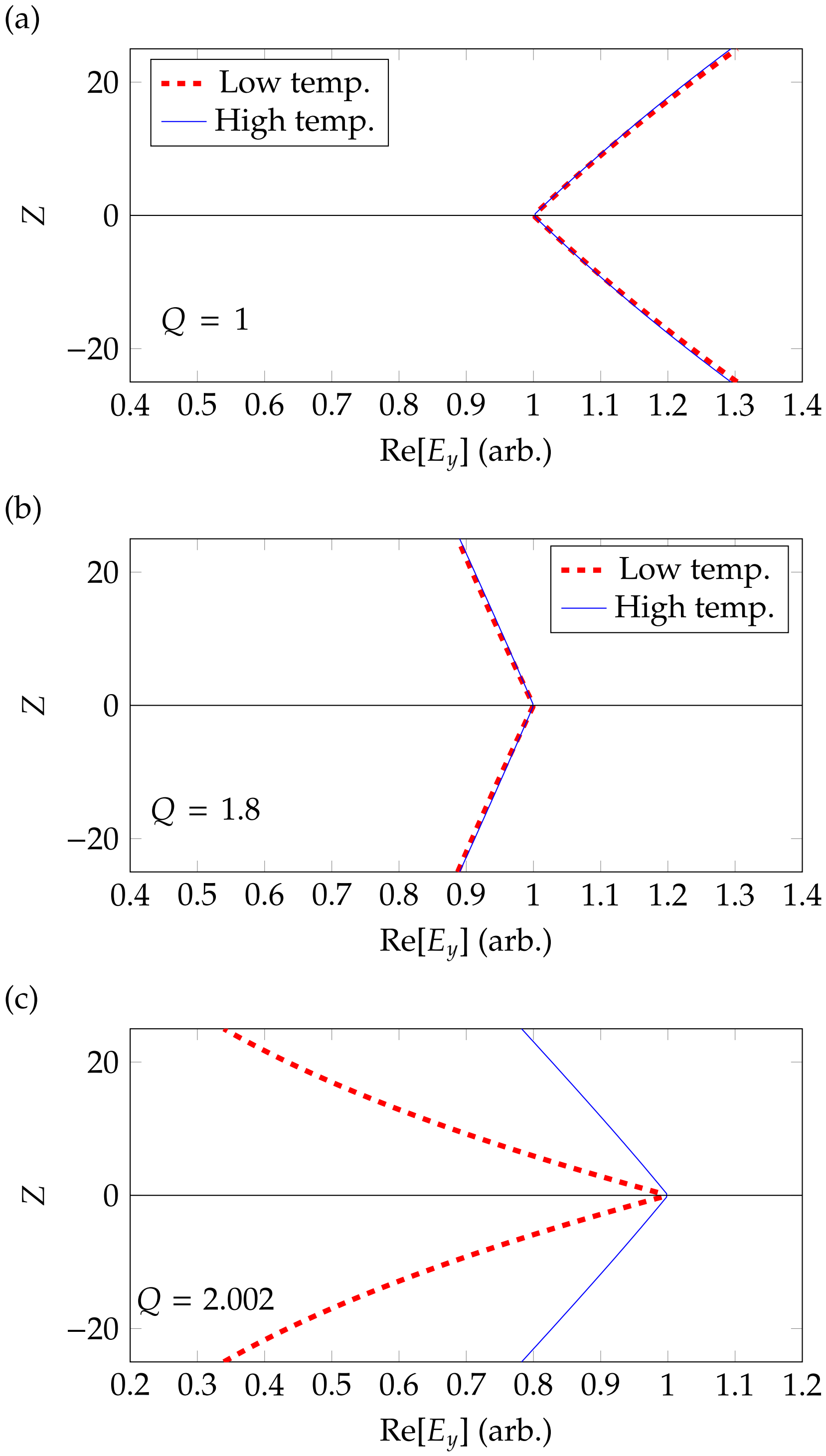

Figure 5.9: Mode field profile across the graphene interface for TE mode for (a) $Q = 1$, (b) $Q = 1.8$, and (c) $Q = 2.002$, for both low temperature ($\mu\beta = 10^5$) and high temperature ($\mu\beta = 10$) settings.

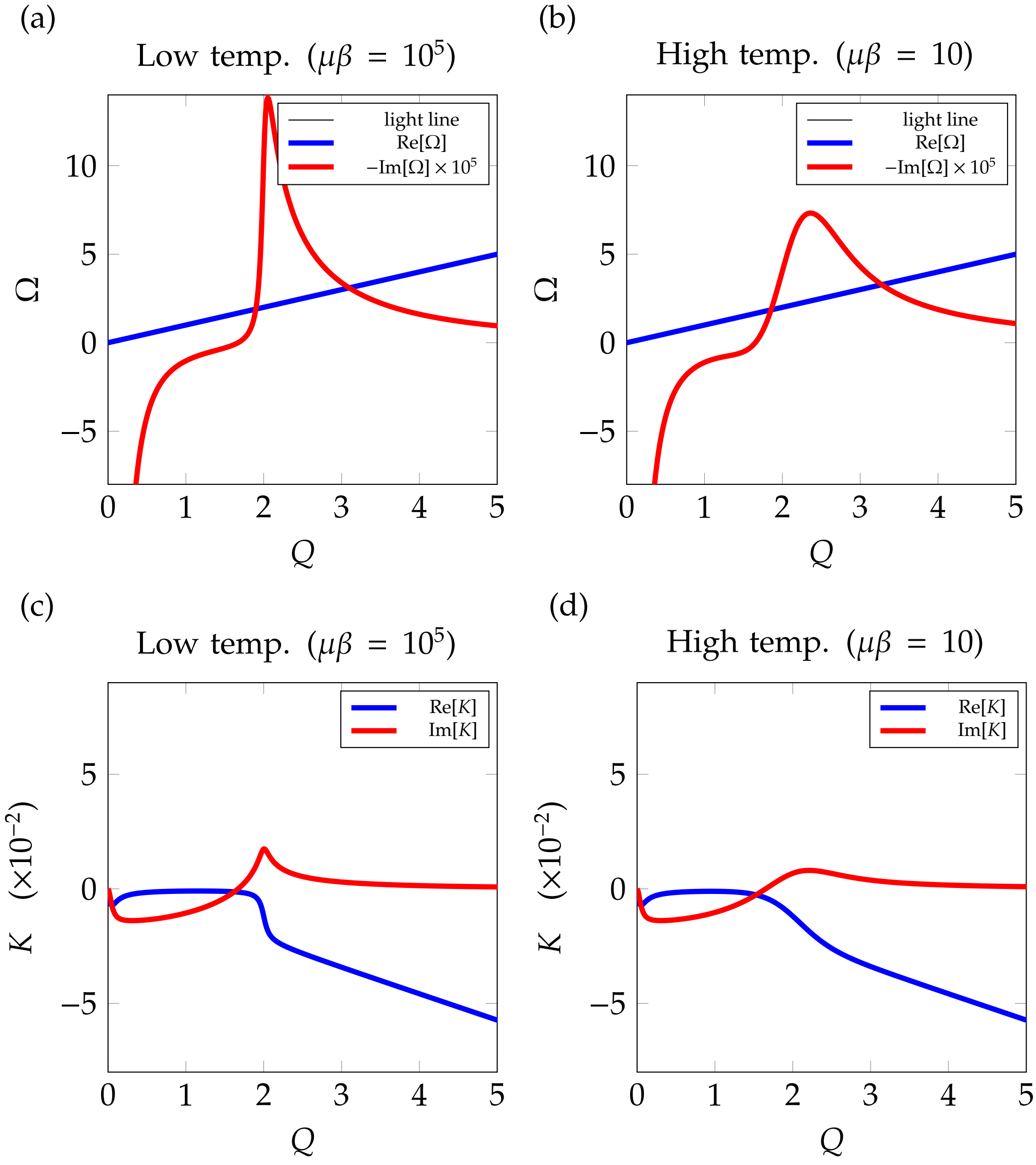

Figure 5.10: Solutions to TE secular equation as real and imaginary Ω (a), (b) as a function of real in-plane wavenumber Q, with non-zero phenomenological damping $\Gamma = 0.05$. The normal component of wavenumber K (c), (d) vs Q with $\Gamma = 0.05$. Left column panels (a), (c) are for low temperature setting, and right column panels (b), (d) are for high temperature setting. Im[Ω] is scaled by $\times 10^5$ as stated in the legend. Curves are calculated using Eq. (5.10).

5.3.3 SPP with phenomenological damping included

We also present, the TE mode with $\Gamma \neq 0$ as shown in Figs. 5.10(a)–5.10(b) demonstrating more changes in Im[Ω]. In comparison with the dispersion for zero Γ (Fig. 5.7), the TE mode now has smoother dependencies of Im[Ω] and K.

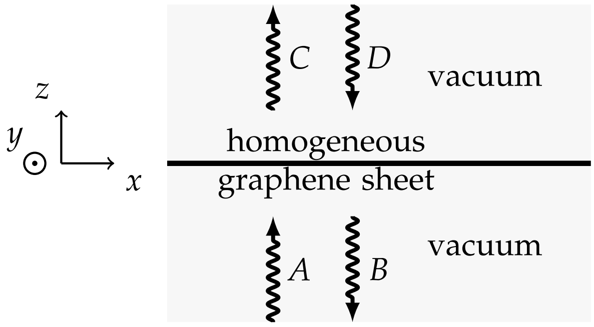

Figure 5.11: Incoming and outgoing coefficients in TE polarisation

Im[K], shown in Figs. 5.10(c) and 5.10(d), starts from zero value at $Q = 0$, and the TE mode frequency still has a positive imaginary part in the range below the threshold frequency $\Omega^{\mathrm{TE}}_{\mathrm{low}}$, similar to what we have seen for $\Gamma = 0$. The qualitative features of K are unchanged due to $\Gamma \neq 0$, although a little smoother than the case of $\Gamma = 0$.

5.3.4 Light transmission through graphene

To show the effect of TE modes of light passing through graphene, we calculate and present the transmission spectra through graphene, given as the ratio between the energy of an incoming normal incident wave and the energy of an outgoing diffracted waves,

$$T \equiv \frac{|C|^2}{|A|^2}, \quad A = 1, D = 0, \tag{5.20}$$

where A, B, C, D are the E_y field incoming or outgoing coefficients as illustrated in Fig. 5.11. The energy of the mode can be obtained by considering the normal component of the Poynting vector.

Fig. 5.12 shows the results for the low temperature setting, $\mu\beta = 10^5$, for different values of in-plane wavenumber Q. At $Q = 0$ in Fig. 5.12(a) we have close to full transmission unless $\Omega \lessapprox 0.5$ or $\Omega \geq 2$. Above $\Omega \geq 2$ the transmission has a step-like drop corresponding to the already mentioned interband absorption of graphene. This value of the absorption has already been measured [110] to be 2.3%. The transmission drops to zero as we get closer to the frequency of the TE

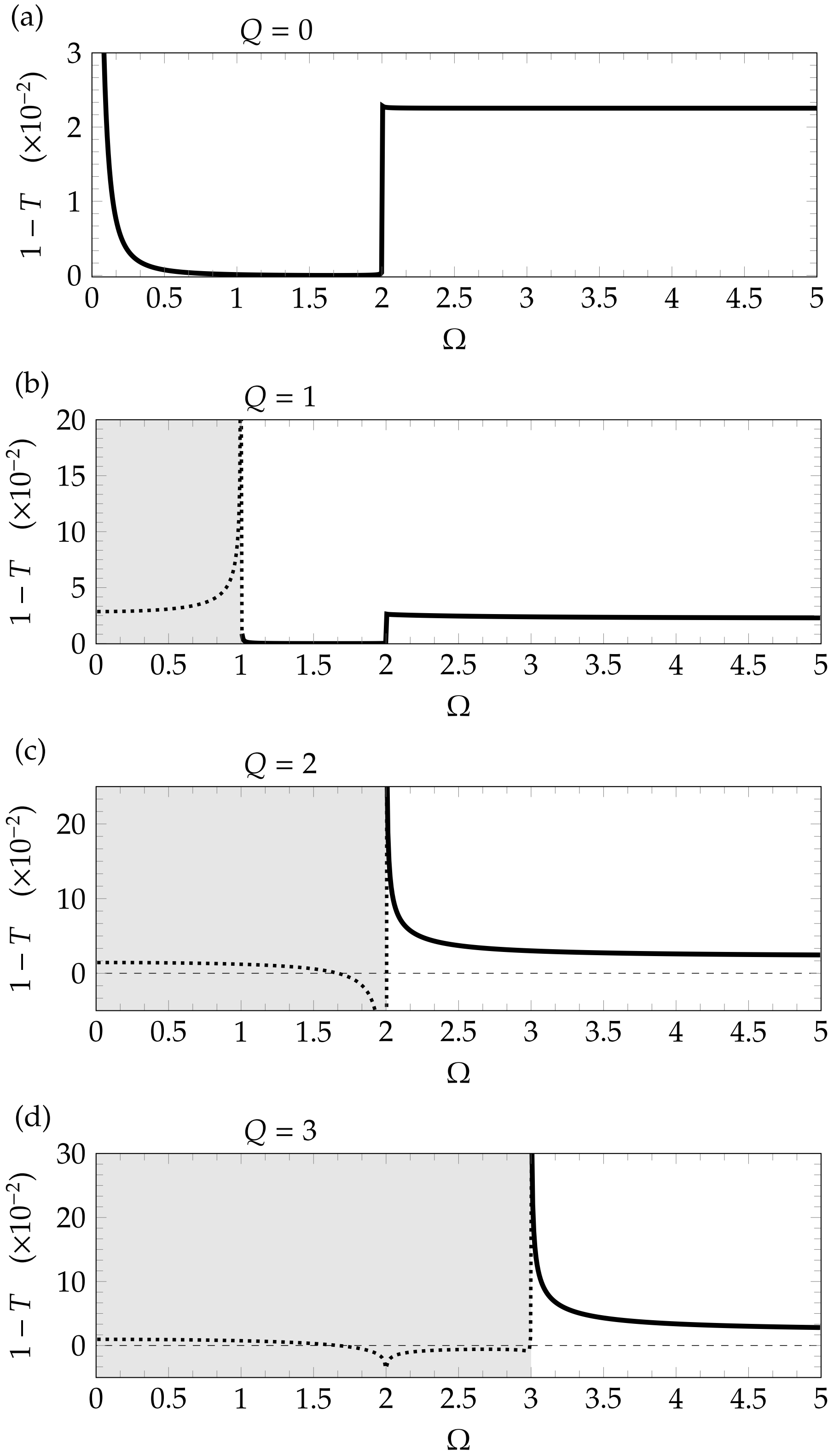

Figure 5.12: Transmission through planar graphene for low temperature $\mu\beta = 10^5$ of TE-polarised light for different Q. Horizontal dashed line indicates zero value.

mode at $Q = 0$.

For $Q \neq 0$, the transmission can be measured only when light can propagate in free space, leading to the condition

$$K \in \mathbb{R} \implies \Omega^2 > Q^2. \tag{5.21}$$

The frequency region not satisfying Eq. (5.21) have been marked with dashed line and grey background in Figs. 5.12 and 5.13 signifying that the value for T does not physically correspond to transmission but is proportional to the near-field. Thus it is possible for the value of $1 - T$ to be negative (or T to exceed 1) in these regions. Actually, the quantity in Eq. (5.20) is measuring the ratio of field amplitude of the light just after leaves to the light just before it enters the graphene sheet. If we were to monitor the transmission far from the graphene in these frequency regions (grey backgroud in Figs. 5.12 and 5.13), the result would be zero amplitude. For low temperature, the TE mode manifests as "half" dips (peaks in $1 - T$) in transmission close to $\Omega = Q$ evident in Fig. 5.12(b)(c)(d). Since the other half of the dips is in the near-field frequency regions, the mode is difficult to be observed as transmission through the graphene. In fact, we have already seen that the frequency dispersion is close to the light line, in Fig. 5.8, where the mode resonance lies in the near-field regions of the transmission spectra for $\Omega \lessapprox 2$. Otherwise, when the mode frequency lies in the range $\Omega \gtrapprox 2$, the energy of the incoming beam is diverted back into the reflected beam. When $Q \geq 2$ in Fig. 5.12(c)(d), we see a peak (dip in $1 - T$) in the near-field corresponding to the effect of interband absorption of the incoming beam.

As we have already observed in other quantities like the conductivity of graphene, and the TE mode dispersion, increasing the temperature has the effect of smearing the features in these quantities due to interband absorption near $\Omega = 2$. We observe similar smearing in the case of transmission as shown in Fig. 5.13, where the step-like feature in Fig. 5.12(a)(b), and also the dip feature in Fig. 5.12(c)(d) at $\Omega = 2$ are smeared in frequency, compared to the low temperature case in Fig. 5.12. The features in Fig. 5.13 related to the TE mode are qualitatively

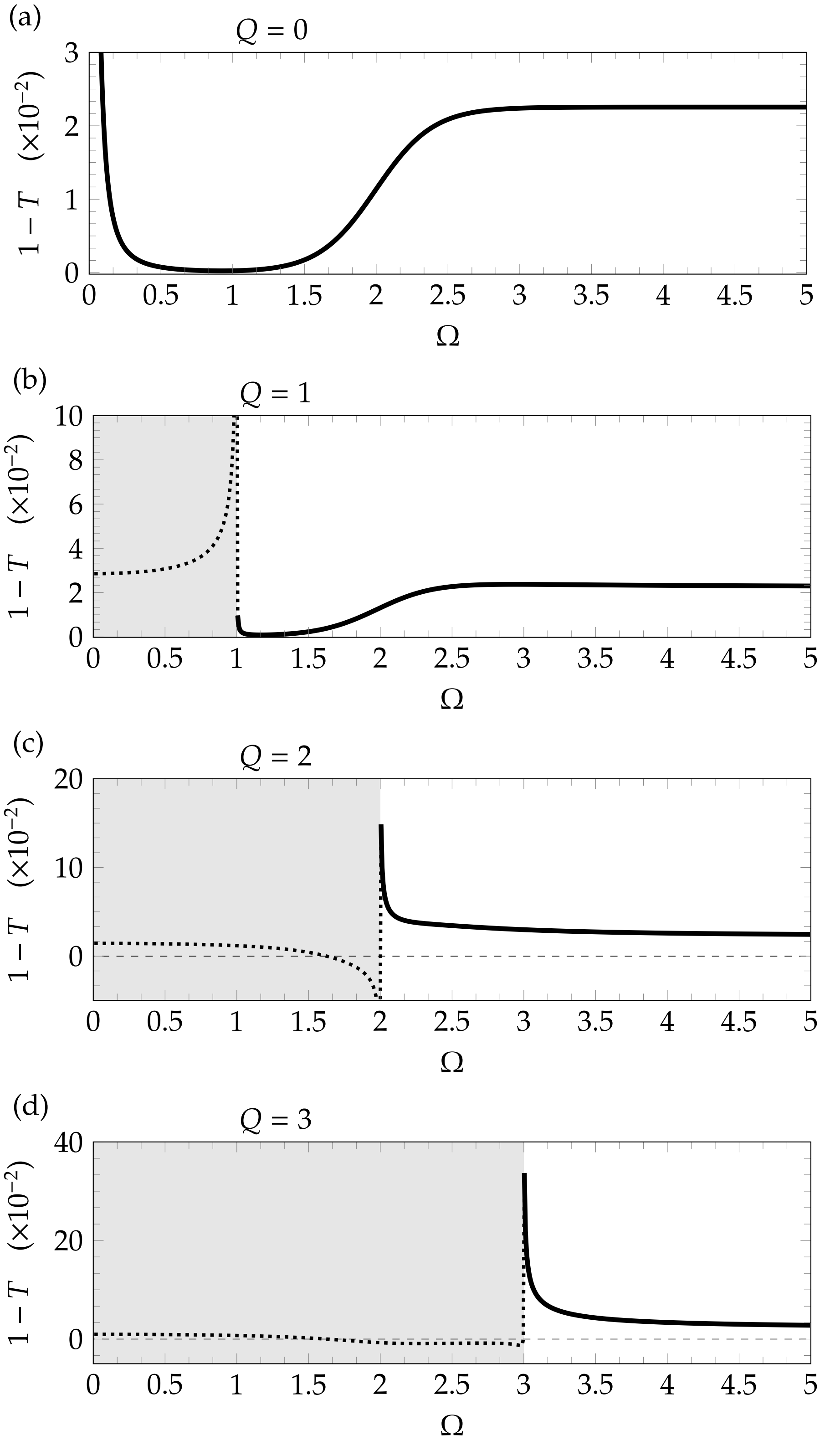

Figure 5.13: Transmission through planar graphene for low temperature $\mu\beta = 10$ of TE-polarised light for different Q. Horizontal dashed line indicates zero value.

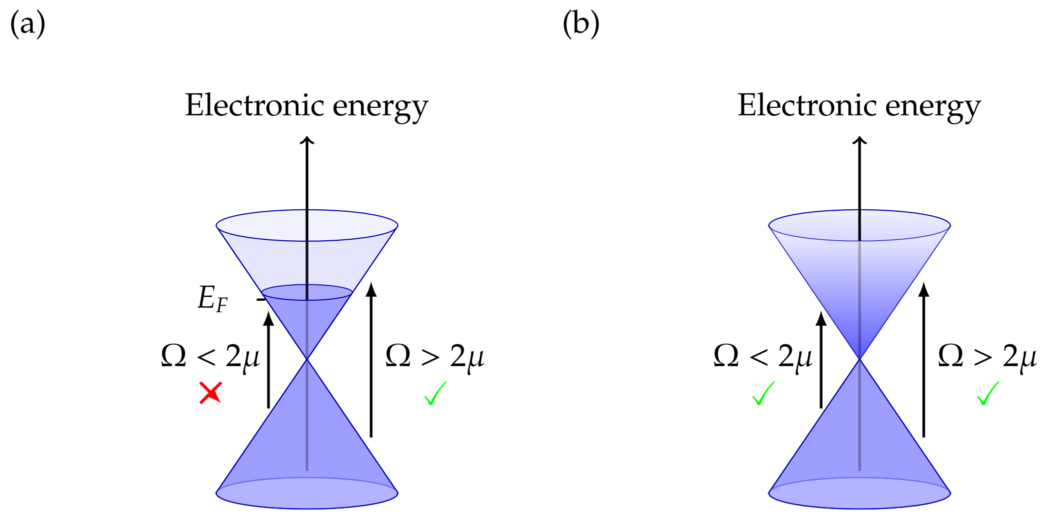

Figure 5.14: Electronic dispersion of graphene near low chemical potential μ, for (a) Low temperature $\mu\beta = 10^5$, and (b) High temperature $\mu\beta = 10$.

unchanged from Fig. 5.12.

5.4 Threshold frequencies

The TE mode in homogeneous graphene in [50] was presented for zero temperature, real frequency and complex in-plane wavenumber with the range of allowed normalised frequency to be $1.667 < \Omega < 2$. The lower limit of $\Omega^{\text{TE}}_{\text{low}} \equiv 1.667$, also defined in Eq. (5.19), was due to the imaginary conductivity becoming positive for $\Omega < \Omega^{\text{TE}}_{\text{low}}$. The upper bound of $\Omega \equiv \Omega^{\text{TE}}_{\text{up}}$ is put there due to the asymptotic behaviour of dispersion due to interband dip in imaginary conductivity at that frequency.

Using complex-frequency analysis reveals dispersion beyond these limits. The effect of interband dip in conductivity on dispersion is evident in Fig. 5.8 for low temperature on the real frequency where asymptotic behaviour is evident approaching $\Omega = \Omega^{\text{TE}}_{\text{up}}$ from $\Omega < \Omega^{\text{TE}}_{\text{up}}$ and also $\Omega > \Omega^{\text{TE}}_{\text{up}}$. The peak in imaginary part of K at $Q \approx \Omega^{\text{TE}}_{\text{up}}$ in Fig. 5.7 is also evidence of this behaviour.

Increasing temperature has an effect of smearing the peak in $|\text{Im}[\Omega]|$ near $Q \approx \Omega^{\text{TE}}_{\text{up}}$, and can be analytically attributed to the smearing effect of the real part of conductivity, and smearing of the Fermi-Dirac function around Fermi level E_F

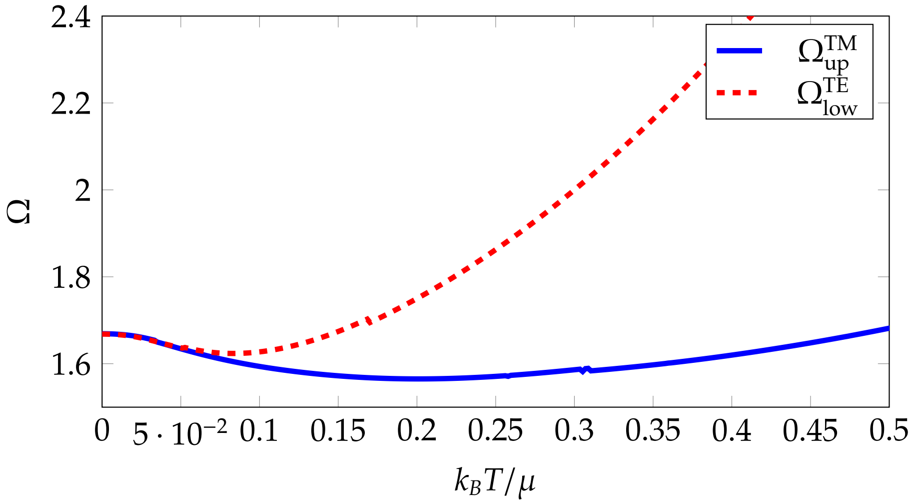

Figure 5.15: Lower threshold frequency for the TE mode (red dashed line), and upper real frequency limit for the TM mode (blue solid line), as functions of the normalised temperature $(\mu\beta)^{-1} = k_B T/\mu$.

which is half of $\Omega = \Omega_{\text{up}}^{\text{TE}} = 2$. Specifically, $|\text{Im}[\Omega]|$ increases with temperature below $\Omega_{\text{up}}^{\text{TE}}$, but decreases otherwise. Physically, for zero temperature interband absorption can only take place for frequencies $\Omega > \Omega_{\text{up}}^{\text{TE}}$ since charge carriers completely occupy energies $E < E_F$, but energies above $E > E_F$ are all vacant, producing the asymmetric sharp peak in $|\text{Im}[\Omega]|$. As the temperature is increased, charge carrier vacancies form for $E < E_F$ increasing interband absorption for $\text{Re}[\Omega] < \Omega_{\text{up}}^{\text{TE}}$, at the same time charge carriers start to occupy $E > E_F$ decreasing interband absorption for $\text{Re}[\Omega] > \Omega_{\text{up}}^{\text{TE}}$. No similar effects are observed for TM polarisation since the dispersion frequency never reaches $\Omega = \Omega_{\text{up}}^{\text{TE}}$.

The effect of increasing temperature on the lower threshold of $\Omega = \Omega_{\text{low}}^{\text{TE}}$ is shown in Fig. 5.15, where it decreases, reaching a minimum at $\Omega_{\text{low}}^{\text{TE}} = 1.6225$, $1/\mu\beta = 0.0824$, then linearly increases with temperature. The physical meaning of this threshold is balance of interband and intraband electronic transitions, mathematically represented by

$$\text{Im}\left[\sigma\left(\Omega = \Omega_{\text{low}}^{\text{TE}}\right)\right] \equiv 0, \tag{5.22}$$

obtained using Eq. (5.10) and the definition Eq. (5.19). Below the threshold frequency $\Omega_{\text{low}}^{\text{TE}}$, we have $\text{Im}[\Omega] > 0$, that is, a field profile that is exponentially growing in amplitude with time at a fixed point in space, implying the existence of some gain, which is not present in this system.

However, from the point of view of energy conservation we find that the SPP mode is physical even for the frequencies below threshold in question. Consider the role of imaginary parts of frequency and normal wavenumber in the field profile, that is,

$$|E(x,z;t)| = |E_0|e^{-K''Z+\Omega''\theta}, \tag{5.23}$$

where $K = K' + iK''$ and $\Omega = \Omega' + i\Omega''$, and θ is unitless time defined by $\omega t \equiv \Omega\theta$. If we look at the Z coordinate of a point sitting on a wavefront, which must satisfy

$$\frac{K'}{Q} = \frac{Z}{X'}, \tag{5.24}$$

given by,

$$Z(\theta) = Z(0) + \frac{K'\Omega'}{Q^2 + K'^2}\theta, \tag{5.25}$$

we find its amplitude, using Eq. (5.23), to be

$$A(\theta) = A(0)e^{-K''Z(t)+\omega''\theta} = \tilde{A}(0)e^{-\gamma\theta} \tag{5.26}$$

where

$$\gamma = \frac{K''K'\Omega'}{Q^2 + K'^2} - \Omega'', \tag{5.27}$$

$$\tilde{A}(0) = A(0)e^{-K''Z(0)}, \tag{5.28}$$

and X is defined by $qx \equiv QX$.

Since the wavefront for TE mode is almost perpendicular to the sheet, that is $|K'| \ll Q$, we conclude using Eqs. (5.17) and (5.18) that

$$\gamma_{\text{TE}} \approx \frac{K''K'\Omega'}{Q^2} - \Omega'' \approx \frac{Q^3\sigma'\sigma''}{Q^2} - \sigma'\sigma''Q = 0, \tag{5.29}$$

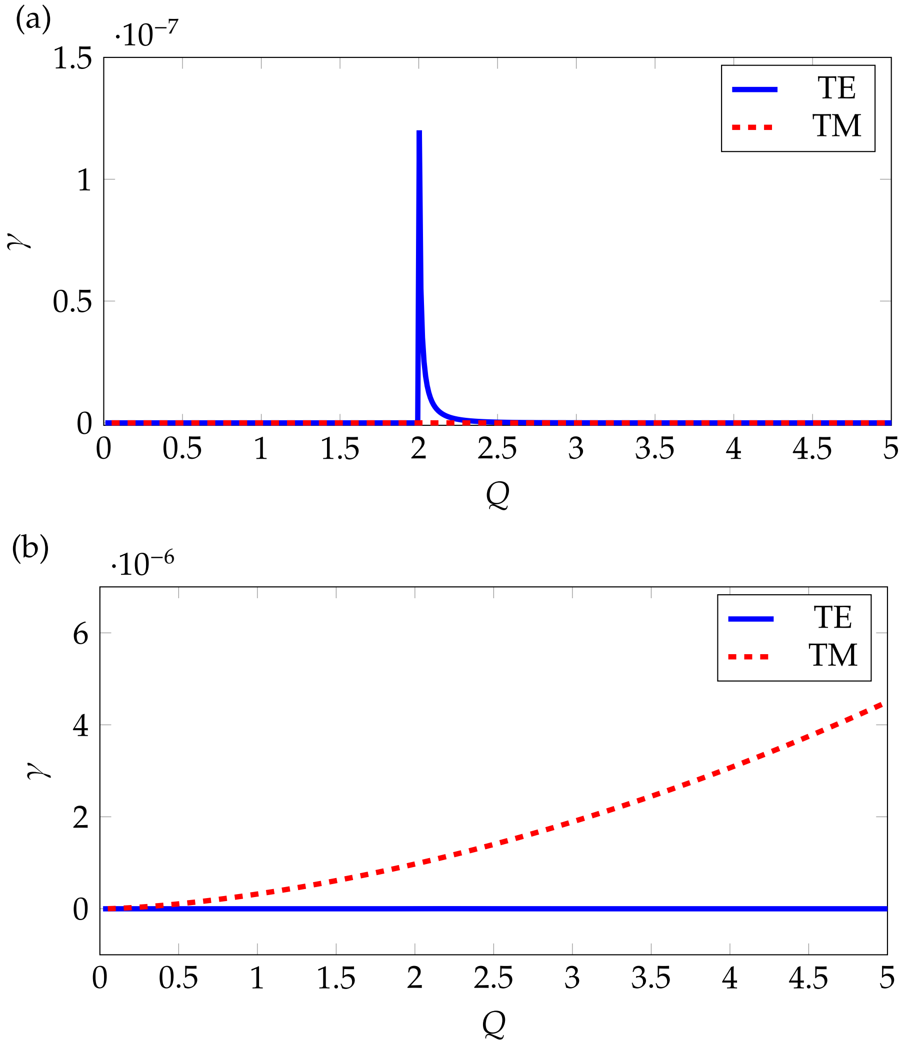

Figure 5.16: The amplitude of wavefront of electromagnetic solution around graphene is not increasing due to lack of any gain source, demonstrated for (a) low temperature $\mu\beta = 10^5$ and (b) high temperature $\mu\beta = 10$.

meaning that no energy is lost and the TE mode is physical both above and below the lower threshold for frequency.

The value for γ is shown as a function of Q in Fig. 5.16 for SPP dispersion in both TE and TM polarisations.

The upper asymptotic threshold of TM dispersion also has a temperature dependence determined by the equation

$$\sigma(\Omega = \Omega_{\mathrm{up}}^{\mathrm{TM}}) = 0, \tag{5.30}$$

obtained from Eq. (5.9) by setting $Q \to \infty$. At zero temperature the threshold for both polarisations are coincident at approximately 1.667.

5.5 Conclusions

In this chapter we have presented numerical calculation of complex frequency dispersion of the SPP modes in a homogeneous graphene layer both in TM and TE polarisations of light. We have further developed a simple analytic approximation which agrees well with the numerically exact solution of the secular equations for the modes in both polarisations. The TM SPP mode is determined by the Drude-like intraband part of the optical conductivity, demonstrating a square-root dispersion of the mode frequency with respect to the propagation wavenumber, asymptotically bounded for large wavenumber. In this polarisation, the temporal decay of the electromagnetic field, which is given by the imaginary part of the mode frequency, monotonously increases with temperature. The TE mode is, on the other hand, determined by both the intraband and the interband part, since the real part of frequency of the mode is not bounded by an asymptote and can coincide with interband features in conductivity spectrum. Unlike the TM mode, its dispersion is close to the light line, and the temporal decay demonstrates a nontrivial dependence on temperature and the propagation wave number. We have observed, in particular, that at finite temperature and chemical potential the TE mode exists above the upper threshold for the normalised frequency $\Omega_{\mathrm{up}}^{\mathrm{TE}} = 2$ posed by an asymptotic behaviour of the dispersion at zero temperature. The temporal decay rate of the TE mode increases below the threshold and decreases otherwise as the temperature increases. This is explained by considering occupation of electronic energy bands in graphene near the K-point at different temperatures. We have also proven that the TE mode exists both above and below the lower threshold $\Omega_{\mathrm{low}}^{\mathrm{TE}}$ (taking the value $\Omega_{\mathrm{low}}^{\mathrm{TE}} \approx 1.667$ at zero temperature) and have studied its behaviour near the threshold. This threshold is caused by a change of the sign of the imaginary part of the graphene conductivity which, in turn, causes a simultaneous change of sign of the imaginary part of the SPP complex eigenfrequency and the normal component of the wave number.

We have looked at the transmission spectra of a TE polarised light passing through graphene for low and high temperatures. Features of the conductivity spectrum show up in the transmission spectra along with the mode peak half of which is near field instead of transmitted energy due to the mode being close to the light line.

By investigating its spatial and temporal evolution, we have shown that the TE in graphene presents a unique optical mode, as it can have below the threshold a positive imaginary part of the eigenfrequency without introducing gain into the material. Furthermore, we have demonstrated that in spite of the positive real part of the conductivity implying the positive imaginary part of the permittivity and hence an absorption, the TE mode propagates along the graphene sheet without losses even at nonzero temperatures. This is correct at least up to second order in the conductivity.

CHAPTER 6

SPPs in periodic graphene

In the previous chapter, TE mode was shown to exist in a homogeneous layer of graphene for an extended frequency range at non-zero temperature [107] using a complex frequency approach with temporal decay. TE modes in a homogeneous graphene layer are tunable via the graphene's chemical potential and temperature. The existence of TE mode in graphene provides exciting prospects for plasmonic systems [111]. In addition, structures with periodic graphene open the possibilities of generating topological plasmonic states [112–115] when magnetic field is applied. Unfortunately, TE mode related features in transmission spectra are not entirely in physical transmission region in frequency, therefore not entirely discernable via transmission, as demonstrated by the transmission spectra in previous chapter.

Periodic plasmonic structures of graphene [116–118], and even multilayer stacks of periodic graphene strips [119–123] have been already studied. The effect of stacking graphene-dielectric on transverse magnetic (TM) SPPs has also been analysed for up to ten graphene layers [124]. It is worth noting that although periodic graphene grating structure has been studied for modes in TM polarisation in Ref. [117], it has not been proposed for excitation of TE mode in graphene to the best of our knowledge.

Although the finite element method has been employed by many studies on plasmonic structures [113, 125–127] to investigate SPPs, this method is suitable for relatively small sizes of plasmonic structure as Maxwell's equations have to be discretised in real space over the whole area. This simulation method is usually suitable for demonstrating electromagnetic modes at the edges of the sample of plasmonic structure, but suffers from an increase in computation time for larger samples. Alternatively, one can approximate structural details by expanding Maxwell's equations' solutions in the Fourier space [128], organising the obtained solutions as coefficients of diffraction Bragg orders, which is more appropriate for an infinite system with discrete translational symmetry. Although studies exist that consider the change from homogeneous graphene in the electronic band structure due to periodic modulation [129], these are suitable for period of the order of nanometers. For a modulation period, of microns order, which is sufficiently large compared to the electronic wavelengths, we may approximate the optical conductivity of graphene as isotropic [130], disregarding electronic effects at the edges of graphene in the modulation.

In this chapter, we theoretically show that the TE modes can be excited by incident light with an angle close to normal incidence with the help of 1D periodic modulation in graphene. We demonstrate the excitation of the TE modes as pronounced dips in the zeroth-order transmission spectra and we show that the in-plane wavenumber of the transmission dips are tunable with the grating period. We further find analytical approximations for the dispersion near the center and edge of the Brillouin zone showing the opening of band gaps controlled by the optical conductivity of graphene.

To obtain transmission spectra showing features of the TE mode, we employ the scattering matrix formalism [131–135] that is commonly used for periodically modulated structures in space. In particular, SPP modes correspond to poles of a scattering matrix for the system [132, 134], equivalent to outgoing wave boundary conditions, manifesting as peaks in transmission spectra.

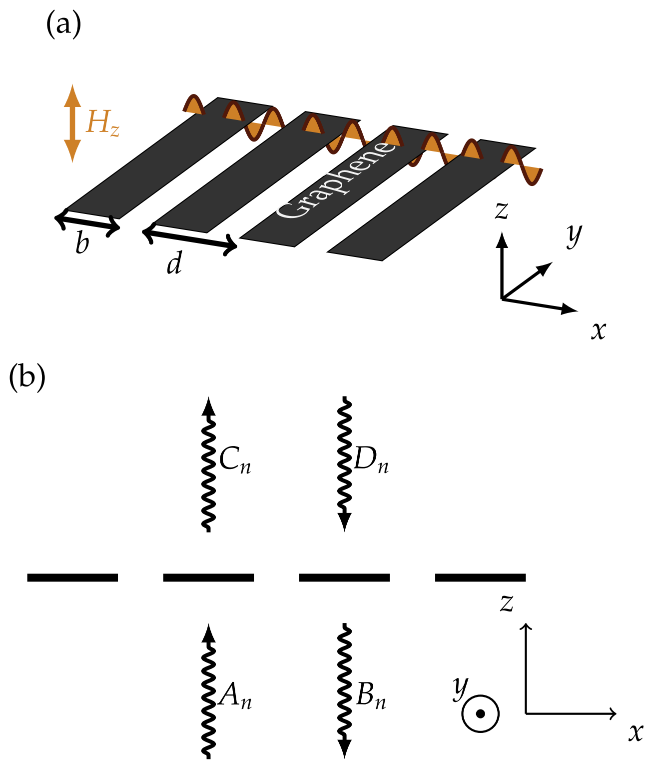

Figure 6.1: Schematic of a graphene grating in a perspective view (a) and in the xz-plane side view (b). An infinitesimally thin graphene sheet at $z = 0$ is periodically modulated along the x axis but homogeneous along the y axis. Arrows labelled A_n, B_n, C_n, D_n schematically represent incoming or outgoing coefficients of diffracted plane-waves with angle of incidence not necessarily normal, where n refers to the nth diffraction order.

6.1 Structure and permittivity model

We consider a graphene grating structure depicted in Fig. 6.1, and mathematically represented by the permittivity tensor given by

$$\varepsilon(\Omega; z) = \begin{pmatrix} \varepsilon_{\parallel}(\Omega; z) & 0 & 0 \\ 0 & \varepsilon_{\parallel}(\Omega; z) & 0 \\ 0 & 0 & 1 \end{pmatrix} \tag{6.1}$$

and the in-plane permittivity

$$\varepsilon_{\parallel}(x, z; \omega) = 1 + \delta(z)\Lambda(x) \cdot \frac{2i\sigma(\Omega)}{\Omega}, \tag{6.2}$$

where $\Lambda(x)$ given by

$$\Lambda(x) = \sum_n \Theta\left(\frac{b}{2} - |x - nd|\right) \tag{6.3}$$

satisfying $\Lambda(x + d) = \Lambda(x)$, $\Theta(x)$ is the Heaviside step function, b is the width of a graphene strip, d is the period, $\sigma(\omega)$ is the complex frequency dependent optical conductivity of graphene in the long-wavelength limit given by Eq. (5.6) (presented in Refs. [40, 50]) and shown in Fig. 6.2(a). The Dirac delta function $\delta(z)$ describes the graphene layer as an infinitesimally thin layer which is justified by the condition that the graphene thickness much smaller than the mode wavelength.

6.2 Scattering matrix approach

The secular equation for SPP modes and their dispersion relations are obtained by solving Maxwell's equations Eqs. (2.1) and (2.2) for the permittivity of the structure and applying boundary conditions across the graphene grating. We will temporarily use ω, k, q which are not unitless to derive secular equations, and for berevity absorb the speed of light with the frequency $\omega/c \to \omega$. For TE polarised waves propagating along the x direction (Fig. 6.1(a)), with $k_y = 0$, we have non-zero magnetic and electric field components in Cartesian coordinates as

$$\mathbf{H} = \begin{pmatrix} H_x \\ 0 \\ H_z \end{pmatrix}, \quad \mathbf{E} = \begin{pmatrix} 0 \\ E_y \\ 0 \end{pmatrix}, \tag{6.4}$$

respectively.

By assuming harmonic solutions in the form of $e^{-i\omega t}$, Maxwell's equations become

$$\begin{pmatrix} -\partial_z E_y \\ 0 \\ \partial_x E_y \end{pmatrix} = +i\omega \begin{pmatrix} H_x \\ 0 \\ H_z \end{pmatrix}, \tag{6.5}$$

$$\begin{pmatrix} \partial_y H_z \\ \partial_z H_x - \partial_x H_z \\ -\partial_y H_x \end{pmatrix} = -i\omega\varepsilon \begin{pmatrix} 0 \\ E_y \\ 0 \end{pmatrix}. \tag{6.6}$$

These can be rewritten as

$$-\partial_z E_y = i\omega H_x, \tag{6.7}$$

$$\partial_x E_y = i\omega H_z, \tag{6.8}$$

$$\partial_z H_x - \partial_x H_z = -i\omega\varepsilon_{\|} E_y, \tag{6.9}$$

$$\partial_y H_y = \partial H_x = 0. \tag{6.10}$$

As defined in Eq. (6.2), the structure of graphene grating is given by $\varepsilon_{\|} \equiv 1 + \alpha\delta(z)\Lambda(x)$, where

$$\alpha \equiv 2i\sigma/\omega, \tag{6.11}$$

in terms of $\omega = \mu\Omega/\hbar$.

If we integrate Eqs. (6.7) and (6.9) around $z = 0$, we have

$$-\left. E_y \right|_{z=0^+} + \left. E_y \right|_{z=0^-} = 0, \tag{6.12}$$

$$\left. H_x \right|_{z=0^+} - \left. H_x \right|_{z=0^-} = -i\omega\alpha\Lambda \left. E_y \right|_{z=0}. \tag{6.13}$$

For the TE polarisation, it is easier to eliminate H_x and write equations in terms of E_y component.

The grating profile $\Lambda(x)$ is expanded over the basis $\{\exp i g_n x\}$,

$$\Lambda(x) = \sum_n V_n e^{i g_n x}, \tag{6.14}$$

where $g_n = 2\pi n/d$ ($n = 0, \pm 1, \pm 2, \ldots$) are the reciprocal lattice vectors, and V_n is the nth Fourier coefficient of $\Lambda(x)$. We can write down the electric field solution to Eqs. (2.1) and (2.2) in the same basis as in the expansion Eq. (6.14),

$$E_y(x,z) = \sum_n e^{i(q+g_n)x} \times \begin{cases} C_n e^{ik_n z} + D_n e^{-ik_n z} & z > 0, \\ A_n e^{ik_n z} + B_n e^{-ik_n z} & z < 0, \end{cases} \tag{6.15}$$

where A_n, B_n, C_n, D_n are the field coefficients of incoming and outgoing waves of the order n as depicted in Fig. 6.1(b), and k_n are given by

$$\omega^2 = (q + g_n)^2 + k_n^2. \tag{6.16}$$

If we substitute Eqs. (6.2) and (6.7) into Eq. (6.13), we have

$$\partial_z E_y\Big|_{z=0^+} - \partial_z E_y\Big|_{z=0^-} = -\omega^2 \alpha \Lambda \, E_y\Big|_{z=0}. \tag{6.17}$$

Then using Eqs. (6.14) and (6.15) yields:

$$\begin{aligned} \sum_n ik_n(C_n - D_n - A_n + B_n)e^{i(q+g_n)x} &= -\omega^2 \alpha \Lambda \sum_n e^{i(q+g_n)x}(A_n + B_n) \\ &= -\omega^2 \alpha \sum_{m,n} e^{i(q+g_n)x} V_m e^{ig_m x}(A_n + B_n) \\ &= -\omega^2 \alpha \sum_{m,n} e^{iqx} e^{ig_{m+n}x} V_m (A_n + B_n) \end{aligned} \tag{6.18}$$

By shifting the indices on the right summation, i.e., $n \to n - m$, we have

$$\sum_n ik_n(C_n - D_n - A_n + B_n)e^{i(q+g_n)x} = -\omega^2 \alpha \sum_{m,n} e^{iqx} e^{ig_n x} V_m (A_{n-m} + B_{n-m}). \tag{6.19}$$

Now we equate the coefficients at $e^{i(q+g_n)x}$ obtaining a matrix equation:

$$ik_n(C_n - D_n - A_n + B_n) = -\omega^2 \alpha \sum_m V_m (A_{n-m} + B_{n-m}). \tag{6.20}$$

Finally, we shift the indices of summation $m \to -m + n$ and we obtain

$$k_n(C_n - D_n - A_n + B_n) - i\omega^2\alpha \sum_m V_{n-m}(A_m + B_m) = 0. \tag{6.21}$$

We get using Eqs. (6.12) and (6.15),

$$C_n + D_n = A_n + B_n. \tag{6.22}$$

A secular equation can then be obtained in matrix form by using Eqs. (6.21) and (6.22),

$$\begin{pmatrix} \mathbf{C} \\ \mathbf{B} \end{pmatrix} = \mathbb{S} \begin{pmatrix} \mathbf{D} \\ \mathbf{A} \end{pmatrix}, \tag{6.23}$$

where $\mathbb{S}$ is the scattering matrix [136] relating the incoming coefficients to outgoing coefficients in Eq. (6.15), and A_n are components of the vector $\mathbf{A}$, etc.

To build a scattering matrix, let us rearrange Eq. (6.21) and Eq. (6.22) in accordance with Eq. (6.23).

$$C_n + B_n + \sum_m \frac{\omega^2\alpha}{ik_n} V_{n-m} B_m = A_n + D_n - \sum_m \frac{\omega^2\alpha}{ik_n} V_{n-m} A_m \tag{6.24}$$

$$C_n - B_n = A_n - D_n \tag{6.25}$$

Thus, in terms of 2 × 2 matrices of diffraction order blocks, the above equations can be expressed as

$$\begin{bmatrix} \mathbf{I} & \mathbf{U}+\mathbf{I} \\ \mathbf{I} & -\mathbf{I} \end{bmatrix} \begin{bmatrix} \mathbf{C} \\ \mathbf{B} \end{bmatrix} = \begin{bmatrix} \mathbf{I} & -\mathbf{U}+\mathbf{I} \\ -\mathbf{I} & \mathbf{I} \end{bmatrix} \begin{bmatrix} \mathbf{D} \\ \mathbf{A} \end{bmatrix}, \tag{6.26}$$

where

$$U_{nm} \equiv \frac{\omega^2\alpha}{2ik_n} V_{n-m} = \frac{\omega\sigma}{k_n} V_{n-m}. \tag{6.27}$$

The scattering matrix is then given by

$$\mathbb{S} = \begin{bmatrix} \mathbf{I} & 2\mathbf{U}+\mathbf{I} \\ \mathbf{I} & -\mathbf{I} \end{bmatrix}^{-1} \begin{bmatrix} \mathbf{I} & -2\mathbf{U}+\mathbf{I} \\ -\mathbf{I} & \mathbf{I} \end{bmatrix}. \tag{6.28}$$

To further simplify the scattering matrix expression, we can write the inverse of a square matrix in terms of its blocks

$$\mathbb{S} = \begin{bmatrix} \tilde{\mathbf{U}}^{-1} & \tilde{\mathbf{U}}^{-1}[2\mathbf{U}+\mathbf{I}] \\ \tilde{\mathbf{U}}^{-1} & -\tilde{\mathbf{U}}^{-1} \end{bmatrix} \begin{bmatrix} \mathbf{I} & -2\mathbf{U}+\mathbf{I} \\ -\mathbf{I} & \mathbf{I} \end{bmatrix}, \tag{6.29}$$

where $\widetilde{\mathbf{U}} = \mathbf{I} + \mathbf{U}$. Finally, after the matrix multiplication, we have

$$\mathbb{S} = \begin{bmatrix} -\tilde{\mathbf{U}}^{-1}\mathbf{U} & \tilde{\mathbf{U}}^{-1} \\ \tilde{\mathbf{U}}^{-1} & -\tilde{\mathbf{U}}^{-1}\mathbf{U} \end{bmatrix}. \tag{6.30}$$

In addition, we find the same result Eq. (6.30) for the TM polarisation, except a different definition for the coupling matrix $\mathbf{U}$,

$$\mathbf{U}_{\mathrm{TM}} \equiv -ik_n \alpha V_{n-m}/2. \tag{6.31}$$

Theoretically, the matrices $\mathbf{U}$ and $\widetilde{\mathbf{U}}$ and thus the scattering matrix $\mathbb{S}$ are of infinite size since their are infinite number of Fourier harmonics in Eq. (6.24). If the basis of matrix $\mathbf{U}$ is ordered by diffraction orders, then the entries in $\mathbf{U}$ for rows and columns near the zeroth diffraction order are the most significant as is the case of small periodic perturbations as less energy transmitted or reflected to higher diffraction orders. Therefore, for numerical purposes we may truncate $\mathbf{U}$ and thus $\mathbb{S}$ to a finite number of diffraction orders. For the transmission, and absorption spectra in Sec. 6.4, we truncate up to tenth diffraction order. The dispersion for SPP modes is given by the poles of $\mathbb{S}$, only allowing outgoing field components to be nonzero [132, 134], giving the secular equation

$$\mathrm{Det}[\mathbb{S}^{-1}] = 0. \tag{6.32}$$

Note that we use the unitless quantities Ω, Q, K for further discussion. Eq. (6.32) is numerically tedious to solve for $\Omega \in \mathbb{C}$ using non-linear root finding methods like the Newton-Raphson method due to the fact that the presence of square-roots in K_n terms produces branch-cuts in $\mathbb{S}$. Instead, we will study transmission spectra of the system and use analytic approximation to find the solution to Eq. (6.32) for $Q = 0$ in Sec. 6.5.

6.3 Tuning of frequency and wavenumber

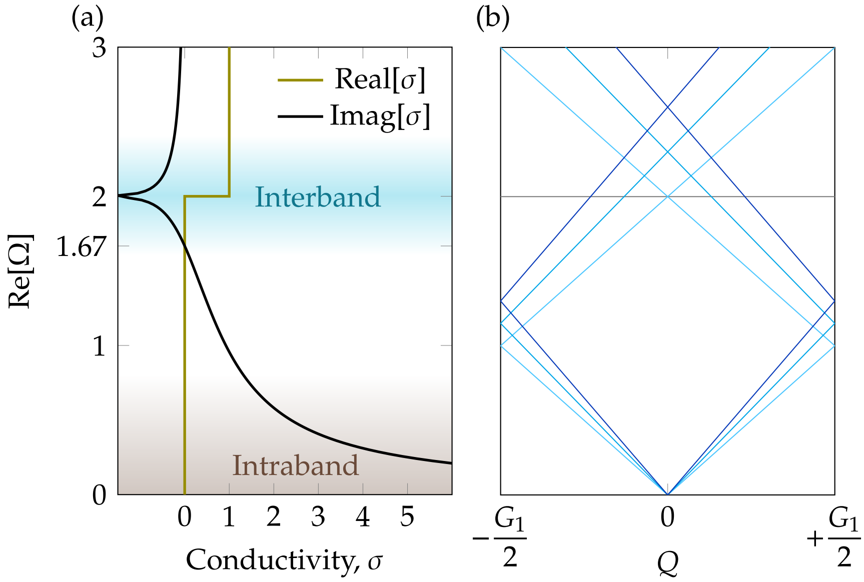

Figure 6.2: (a) Conductivity of graphene at zero temperature $T = 0$, sharing frequency axis with dispersion in panel (b). The frequency of interband dip in conductivity is affected by μ but not d. (b) Real frequency of TE mode dispersion of homogeneous graphene structure manually folded over a hypothetical Brillouin zone, shown for $G_1 = 2$, 2.3 and 2.6. The size of the first Brillouin zone, and consequently the frequency of crossing at $q = 0$, is controlled by μd. Note: TE mode is close to the light line due to small value of fine-structure constant.

The conductivity spectrum of graphene, shown in Fig. 6.2(a), has a key frequency $\mathrm{Re}[\Omega] = 2$ where the interband dip occurs. Since this frequency Ω, also appearing in the scattering matrix in Eq. (6.32), is normalised as multiples of μ, we can control the interband transition frequency in Hz by changing μ. Furthermore, by tuning the grating period d, and thus changing the edge of Brillouin zone $G_1/2$ in Fig. 6.2(b) where the bands are folded, we can change the crossing frequency of the TE bands at $q = 0$. Here, $G_n \equiv \hbar c g_n/\mu$ is the normalised reciprocal lattice wavevectors and normalised normal wavenumbers are $K_n \equiv \hbar c k_n/\mu$, so that $\Omega^2 = (Q + G_n)^2 + K_n^2$, similar to Ω defined in Ch. 5. Since the grating period has no effect on the conductivity spectrum in Fig. 6.2(a), that is, photon wavenumbers are much smaller than electronic wavenumbers, we can independently choose wavenumbers for the desired normalised frequencies of the TE mode. For an effective demonstration of this tuning process, we define the normalised interband detuning

$$\Delta \equiv G_1 - 2, \tag{6.33}$$

between the crossing in dispersion at $\Omega = G_1 = \frac{\hbar c}{\mu}\frac{2\pi}{d}$ and the interband dip in conductivity at $\Omega = 2$ as illustrated in Fig. 6.2(b).

For a chemical potential of $\mu \approx 0.2eV$, zero detuning $\Delta = 0$ would require the grating period to be in the order of micrometers. Since the dispersion of TE mode is close to the light line, we may assume the TE mode dispersion as the light line and estimate the grating period required to tune the TE mode to a desired set of frequency ω and in-plane wavenumber q (not normalised). We find, for example, that, the dependence of grating period d required to achieve the minus first diffraction order of TE mode at $\Omega = 2$, on in-plane wavenumber q, related to incident angle $\phi = \sin^{-1}(cq/\omega)$, is given approximately by

$$d \approx \frac{2\pi}{\frac{\mu\Omega}{\hbar c} + q}. \tag{6.34}$$

Eq. (6.34) is illustrated in Fig. 6.3, for various frequencies in Hz. The sensitivity of the grating period required increases for higher in-plane wavenumber and higher frequencies. This can be useful for applications involving sensors utilising in-plane strain properties [137] of graphene. Similar dependencies of required

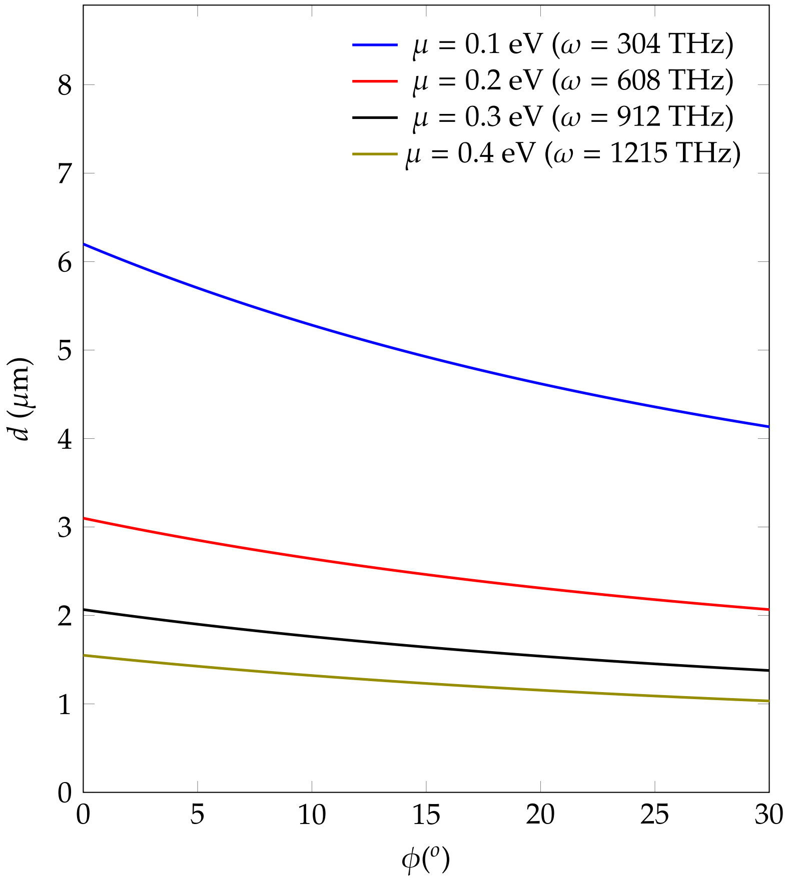

Figure 6.3: The period of grating d required for normalised frequency $\Omega = 2$, various chemical potentials μ and corresponding frequencies ω (legend) as a function of desired incidence angle $\phi = \sin^{-1}(cq/\omega)$ in degrees, using Eq. (6.34).

period can also be found for other non-zero diffraction orders of the TE mode.

6.4 Transmission and absorption spectra

To show that the TE modes can be excited by an incident plane wave, we calculate and present the transmission spectra of the TE modes in the graphene grating structure depicted in Fig. 6.1. The transmission is given as the ratio between the energy of the incident wave and the energy of the outgoing diffracted waves, using Eq. (2.32),

$$T_n \equiv |C_n|^2 \times \left|\frac{K_n}{K_0}\right|, \; A_n = \delta_{n0}, D_n = 0, \tag{6.35}$$

where δ_{n0} is the Kronecker delta. We consider transmission separately for each diffraction order n, not taking into account the interference effects as we are concerned with the surface TE mode along grating rather than the transmission pattern at a distance. The expression for transmission in Eq. (6.35) can be obtained by considering the normal component of the Poynting vector in the TE polarisation. Note that it is different from the transmission expression for homogeneous graphene in Eq. (5.20) by a factor of $\frac{K_n}{K_0}$ for non-zero diffraction order. This factor of $\frac{K_n}{K_0}$ in Eq. (6.35) arises in Eq. (2.32) and is the ratio of normal components of light propagation between the nth diffraction order just after exiting and the incoming beam just before the grating. Therefore this factor accounts for flow of energy normal to the grating as K_n is the normal component of wavenumber of light for nth diffraction order. The transmission can be measured only when the diffracted waves can propagate in free space, which leads to the condition

$$\Omega^2 > (Q + G_n)^2 \tag{6.36}$$

for nth diffraction order.

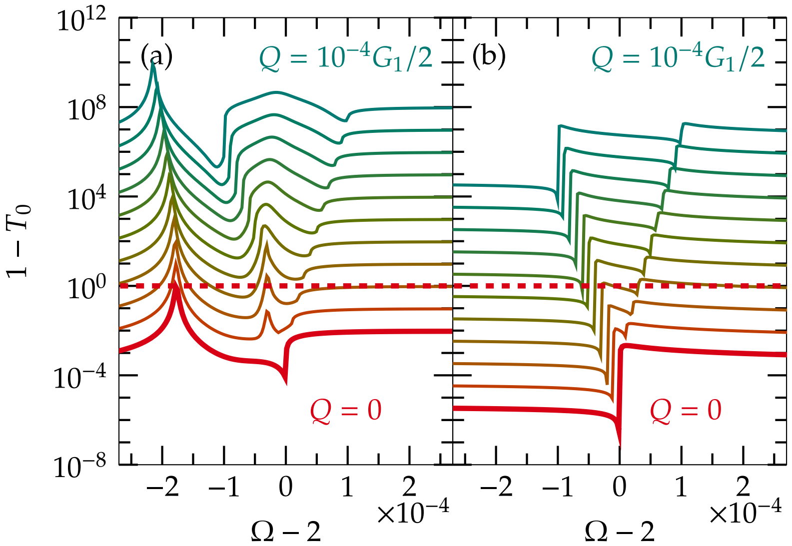

Figure 6.4: Transmission spectra $(1 - T_0)$ for zeroth (normal incidence) diffraction order when a TE polarised light with parallel wavenumber Q, is incident on the grating with $b/d = 0.3$, $\Delta = 0$, for (a) graphene with $\sigma = \sigma_{\text{intra}} + \sigma_{\text{inter}}$, (b) single-layer graphene without interband conductivity $\sigma = \sigma_{\text{intra}}$. The dashed red line indicates $T_0 = 0$. Note that spectra for $Q \neq 0$ are offset by powers of ×10 in increasing value of Q, and $1 - T_0 < 1$ is satisfied. Please note that $\Omega > 0$ in the horizontal axes.

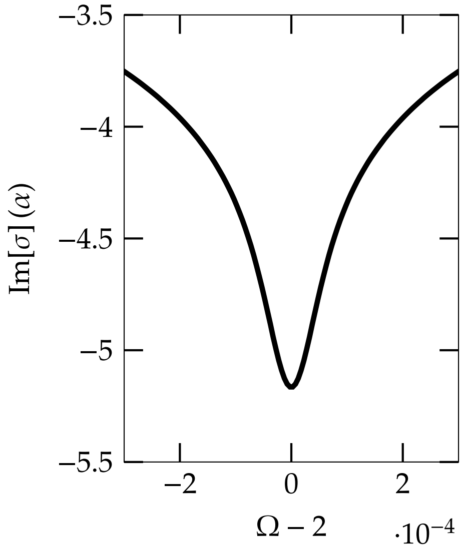

Figure 6.5: Im[σ] shown for low temperature $\mu\beta = 10^5$ for frequencies $\Omega \in [-3 \times 10^{-4}, 3 \times 10^{-4}]$, demonstrating that the width of the rise in conductivity is wider than the TE peak in Fig. 6.4.

We now present the transmission spectra through a graphene grating with 30% filling factor ($b/d = 0.3$), for a normally incident TE-polarised plane wave, where the grating period is set so that $\Delta = 0$. Figure 6.4 shows the transmission spectra for single-layer graphene grating, and graphene grating without interband conductivity σ_{inter}. In all three cases, the signature of the light lines are peaks and dips in $1-T_0$ that start from the dips at $\Omega = 2$ when $Q = 0$, moving apart from each other as Q increases. The TE mode, evident as peaks in $1 - T_0$, is close to the light line, just as in the case of homogeneous graphene in [50, 107]. By choosing grating period such that $\Delta = 0$, we have coincided the frequency of the TE mode at $Q = 0$ with the dip in spectrum of the imaginary part of the conductivity in Fig. 6.2(a) at $\Omega = 2$, and thus enhancing the TE peak at $\Omega - 2 \approx -2 \times 10^{-4}$ in $1 - T_0$ in panel (a) for $Q = 0$. This peak corresponds to the diversion of energy of the incoming TE beam into reflection channel. The origin of this peak is the TE mode, where at the same time it is enhanced by the rise in conductivity for low temperature as shown in Fig. 6.5. The origin is TE mode since it is given by poles of scattering matrix, and as shown in Sec. 6.5 the peak in transmission indeed corresponds to the TE mode. We can see in Fig. 6.5 that the width of rise in conductivity is wider than the TE peak in Fig. 6.4.

At small $Q \neq 0$, an additional peak emerges closer to $\Omega = 2$, that is not present for $Q = 0$, meaning that it is a dark mode. In Sec. 6.5, we will analytically prove the absence of this mode peak, to confirm its absence in Fig. 6.2(a) at $Q = 0$.

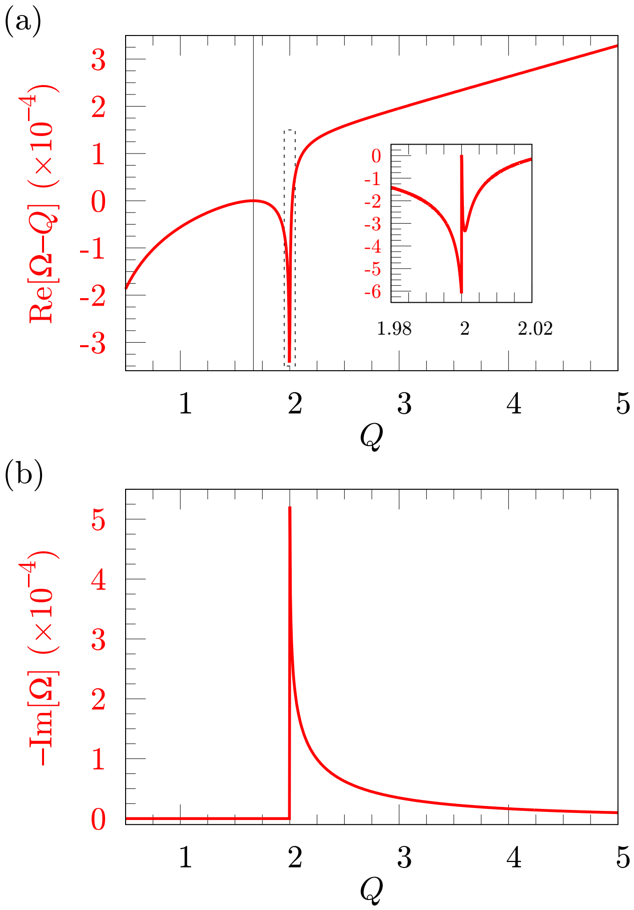

Figure 6.6: Dispersion of the TE mode in a homogeneous graphene with real frequency plotted as multiple of wavenumber to demonstrate that dispersion is below the light line for $Q < 2$ but above the light line for $Q \gtrsim 2$.

To gain insight for the shift of dips and peaks in the transmission spectra, we refer to the complex frequency plasmonic dispersion of a homogeneous graphene sheet shown in Fig. 6.6. Here we use the temperature, $\mu\beta = 10^5$. The dip in dispersion in Fig. 6.6(a) for single layer (red line) showing the difference of about -4×10^{-4} between light line and the real part of frequency $\text{Re}[\Omega - Q]$, approximately corresponds to the order of magnitude of distance of the TE peak in $1 - T_0$ for $Q = 0$ in Fig. 6.4(a) from $\Omega = 2$. Furthermore, $\text{Im}[\Omega]$ Fig. 6.6(a) is also the same order of magnitude corresponding to the linewidth of the TE mode peak in $1 - T_0$ for $Q = 0$.

The distinct TE mode peak in $1 - T_0$ in Fig. 6.4(a) disappears when the interband conductivity σ_{inter} contribution is removed from the conductivity σ, as demonstrated in Fig. 6.4(b), and consequently the TE mode of a homogeneous sheet also disappears. Step-like features are revealed in transmission along the light line at the frequency of whom diffraction channels are opening with increasing frequency in accordance with Eq. (6.36). As frequency increases to the point that Eq. (6.36) is satisfied, transmission of the nth diffraction order increases corresponding to abrupt reduction in T_0.

Note that the TE mode peak has been shifted about by a factor of 40 from the light line from its previous position for the single-layer case (Fig. 6.4(a)).

The effect of change in temperature on the TE mode peak is change in peak width. Fig. 6.7 shows that the mode peak is reaching maximum height at zero temperature. At nonzero temperature, the graphene produces a TE peak less discernable in frequency in Fig. 6.7.

6.4.1 Other diffraction orders of transmission and absorption

Here we present the transmission spectra for grating with the filling factor $b/d = 0.3$ for the first Brillouin zone $Q \in [0, G_1/2]$ and for different grating periods such that $\Delta = -1, -2 + 1.667, 0$, calculated using Eq. (6.35). We also show the absorption spectra using

$$R_n(\Omega) \equiv |B_n|^2 \times \left|\frac{K_n}{K_0}\right|, \tag{6.37}$$

$$A(\Omega) \equiv 1 - \sum_{n \in \{\Omega > Q + G_n\}} (T_n + R_n), \tag{6.38}$$

where R_n is the reflection coefficient describing the ratio between the energy of reflected waves and the energy of the normally incident TE wave.

Fig. 6.8, Fig. 6.9 and Fig. 6.10 show transmission and absorption spectra for single layer ($N = 1$) graphene grating for $\Delta = -1, -2 + 1.667$ and 0, respectively, corresponding to $G_1 = 1, 1.667$ and 2.

The SPP modes manifest as peaks moving with changing Q in transmission

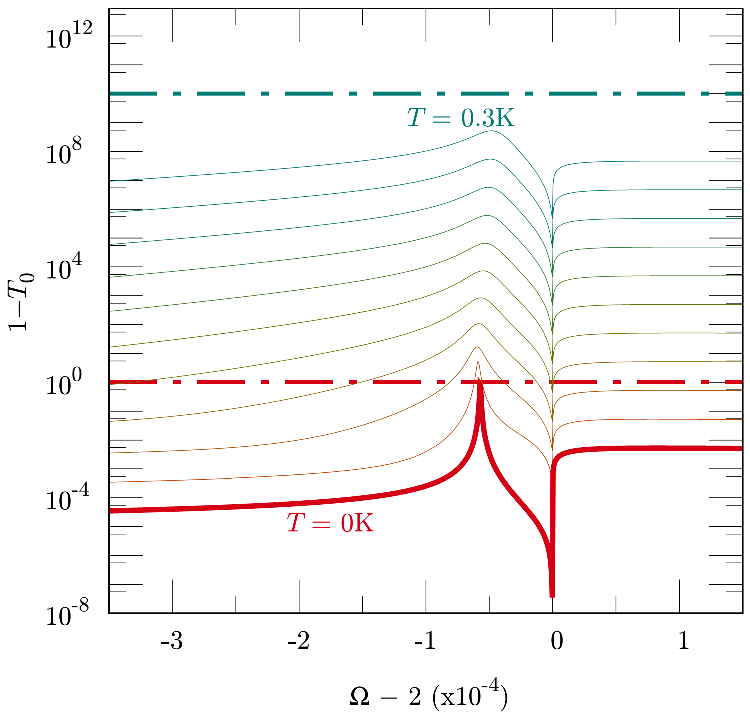

Figure 6.7: Transmission spectra $(1 - T_0)$ for zeroth (normal incidence) diffraction order when a TE polarised light is normally incident $Q = 0$, on grating with $b/d = 0.3$, $\Delta = 0$, shown from zero temperature (red) to finite temperature (green), for graphene. Red and green dashed dotted lines indicate $T_0 = 0$ for zero temperature and $T = 0.3K$, respectively. Note that spectra for $T \neq 0$ are offset by powers of ×10 in increasing value of T, and $1 - T_0 < 1$ is satisfied.

spectra in Fig. 6.8, Fig. 6.9, Fig. 6.10 in panels (a)(c)(e), and as dips in panel (g). The absorption A in panel (g) is zero for $\Omega < 2$ but 10^{-2} otherwise which correlates to interband absorptions with sharp frequency cut-off at $\Omega = 2$ for zero temperature. In zeroth-order transmission $1 - T_0$, the TE mode peaks are lost due to interband absorption for frequencies above $\Omega > 2$, instead appearing as dips in the absorption spectrum A, for such frequencies. Meaning the energy of the incoming TE beam that is diverted to reflection channel due to TE mode is taken out of the absorption. Since the mode features are sharp in frequency, we show zoom in of the TE mode transmission at $Q = 0$ for minus-first (panel (b)), and zeroth (panel (d)) diffraction orders. First-order transmission for small but finite $Q \neq 0$ is shown in panel (f).

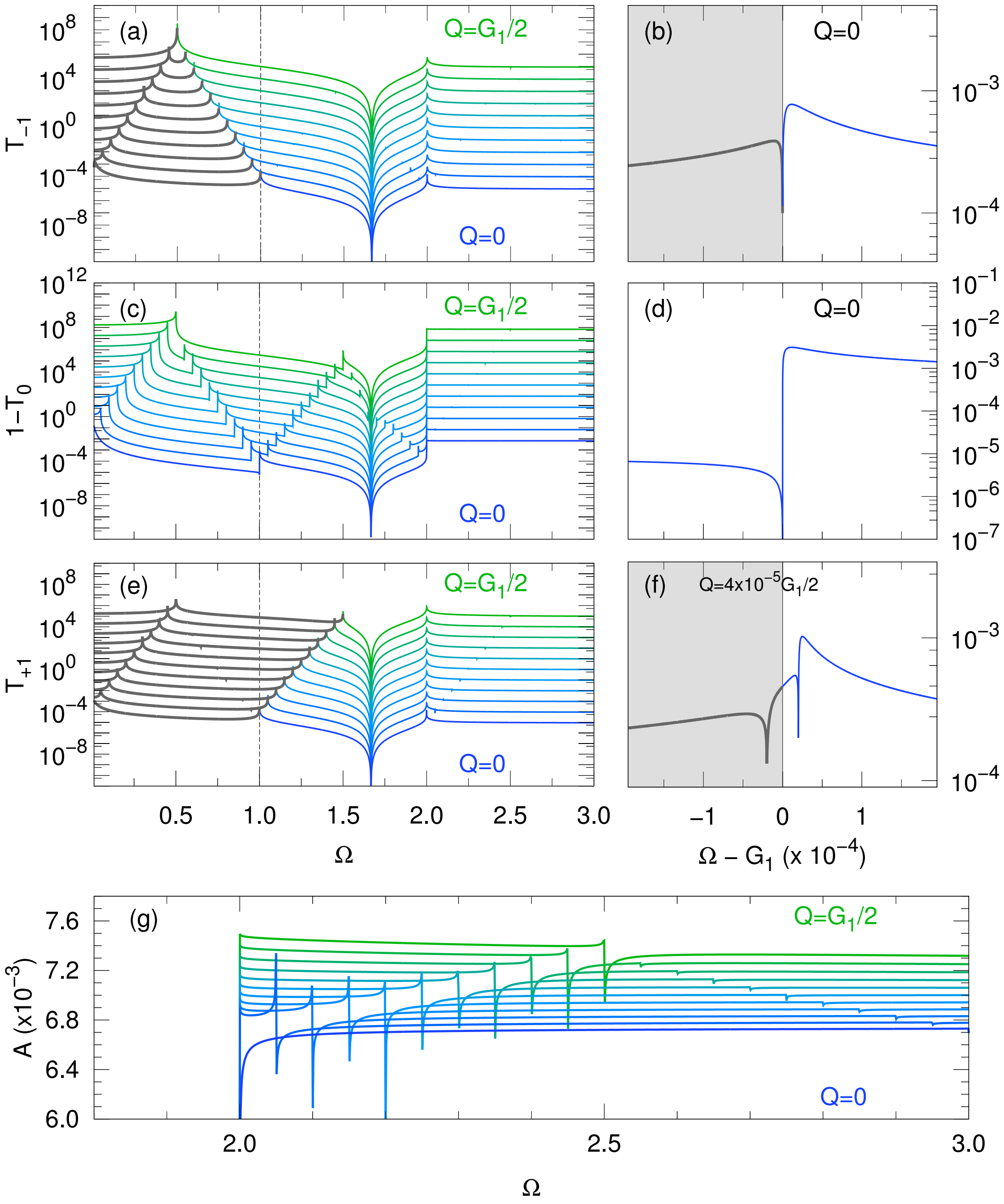

Figure 6.8: Transmission spectra for single layer graphene ($N = 1$), for the -1 diffraction order (a)(b), 0 order (c)(d), and $+1$ order (e)(f), for when period is adjusted so that $\Delta = -1$ ($G_1 = 1$). Panels (b)(d) are zoom in of peaks near $Q = 0, \Omega = G_1$ in (a)(c). Panel (g) is absorption of open channels calculated using Eq. (6.38), with waterfall increment of +0.02. $A(\Omega < 2) = 0$ for zero temperature. The gray solid lines correspond to evanescent frequency range where Eq. (6.36) is not satisfied, and the curve has the meaning of near-field amplitude.

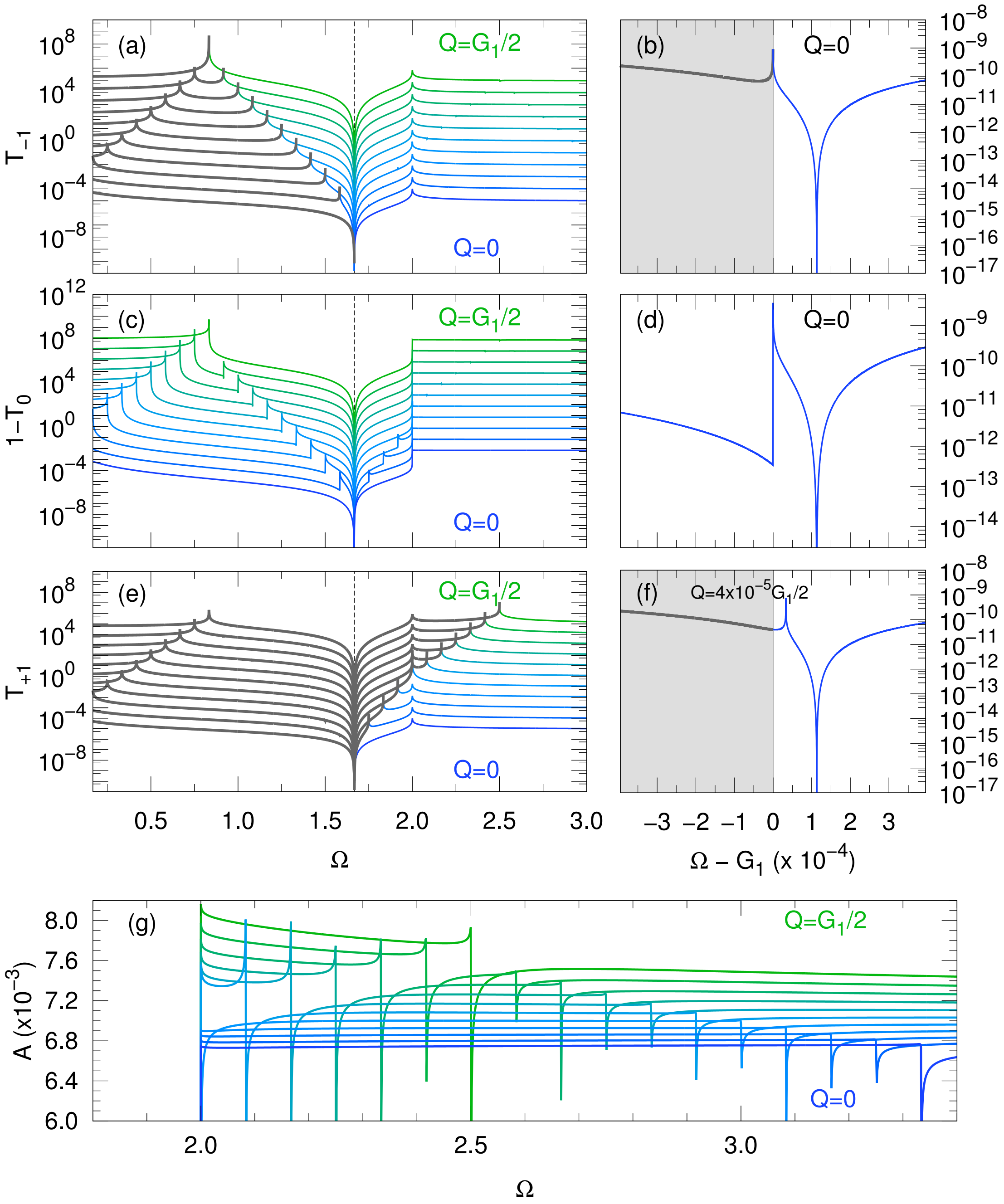

Figure 6.9: Same as Fig. 6.8 but for $\Delta = -2 + 1.667$ ($G_1 = 1.667$), illustrating suppression in amplitudes.

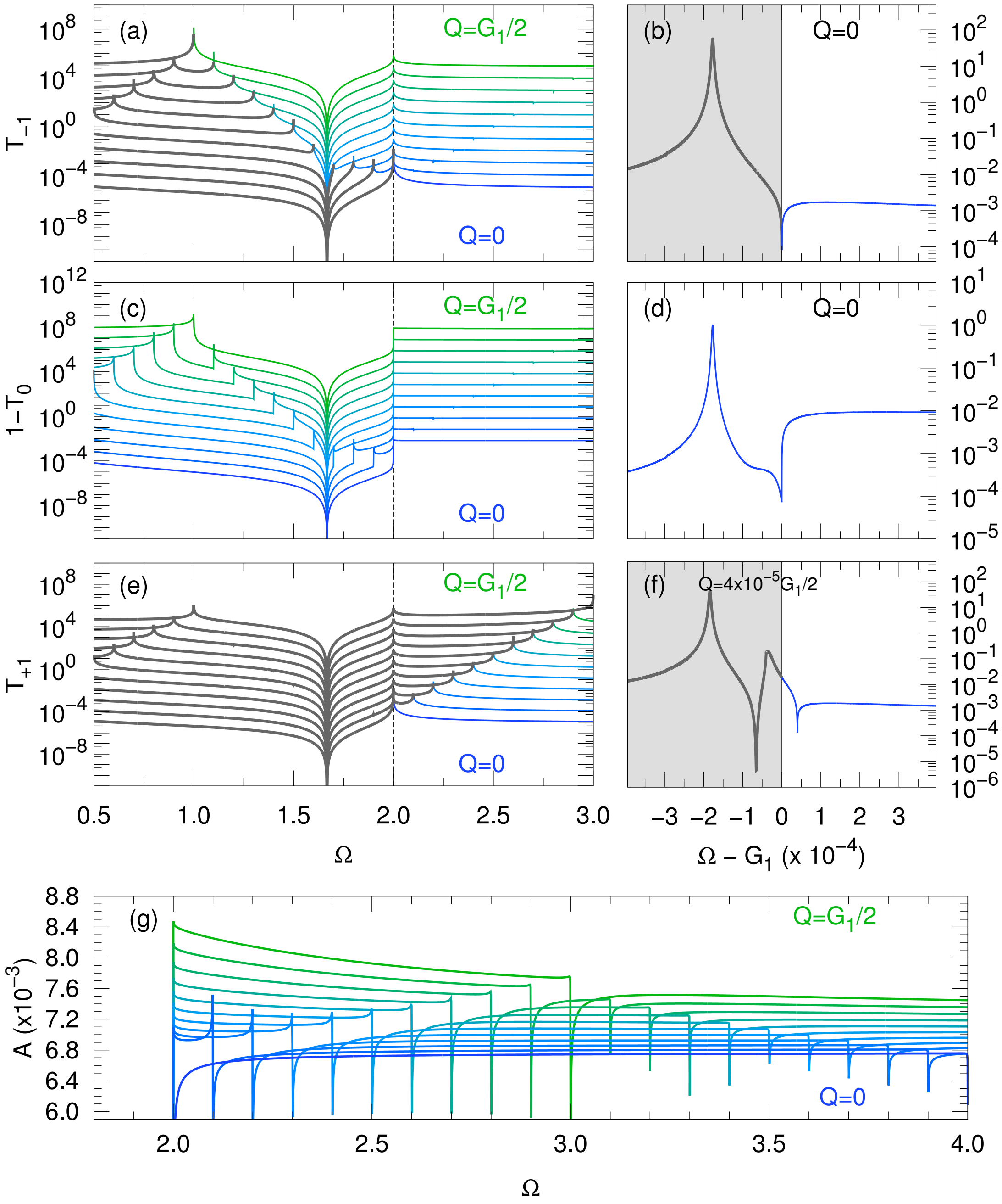

Figure 6.10: Same as Fig. 6.8 but for $\Delta = 0$ ($G_1 = 2$), illustrating the amplification in amplitudes.

For $\Delta = -1$ in Fig. 6.8, the TE mode appears at frequency very close to G_1 in panel (b). When Q is increased slightly in panel (f), the TE mode peak moves away from G_1 increasing in frequency in the open channel region (not gray).

For $\Delta = -2 + 1.667$ in Fig. 6.9, the TE mode peak can be seen moving from panel (b) to panel (f) on slightly increasing Q. The peak size is very small, about 10^{-10} in this case due to vanishing conductivity near this frequency of $G_1 \approx 1.667$. In fact we can even see the dip due to this vanishing conductivity in panels (b)(d)(f). This frequency at $Q = 0$ is when the TE dispersion for homogeneous graphene is exactly on the light line, as demonstrated by the maximum in Fig. 6.6 at $Q \approx 1.667$.

For $\Delta = 0$ in Fig. 6.10, the TE mode peak is clearly enhanced due to dip in imaginary part of the conductivity. The evanescent near-field peak moves further into lower frequency for increasing Q from panel (b) to (f).

6.5 Analysis of transmission spectra in terms of the TE modes

For completeness, in addition to transmission spectra, we calculate explicit frequency values of SPP mode features that could be observed using Eq. (6.35). Since the conductivity $\sigma(\omega)$ in the scattering matrix is frequency-dependent and thus computationally intensive to solve, we present, instead of an exact explicit expression, an approximation of part of dispersion of SPP mode. We specifically provide, as an example, an approximation for dispersion near crossing point $Q = 0, \Omega \approx G_1$. We want to reveal the effects of periodic modulation by focusing on dispersion near a crossing point.

The SPP modes of the system correspond to outgoing boundary conditions, i.e. poles of the scattering matrix in Eq. (6.23). To find an approximation for transmission, we truncate $\widetilde{\mathbf{U}}^{-1}$ in the scattering matrix Eq. (6.30) to the first diffraction order, that is,

$$\widetilde{\mathbf{U}} = \begin{pmatrix} 1+\frac{\Omega}{K_{-1}}\tilde{V}_0 & \frac{\Omega}{K_{-1}}\tilde{V}_{-1} & \frac{\Omega}{K_{-1}}\tilde{V}_{-2} \\ \frac{\Omega}{K_0}\tilde{V}_1 & 1+\frac{\Omega}{K_0}\tilde{V}_0 & \frac{\Omega}{K_0}\tilde{V}_{-1} \\ \frac{\Omega}{K_1}\tilde{V}_2 & \frac{\Omega}{K_1}\tilde{V}_1 & 1+\frac{\Omega}{K_1}\tilde{V}_0 \end{pmatrix}, \tag{6.39}$$

where $\tilde{V}_n \equiv N\sigma(\Omega)V_n$, and $K_n \equiv \sqrt{\Omega^2 - (Q+G_n)^2}$.

The approximate transmission coefficients are then given by the middle column entries of the inverse of Eq. (6.39),

$$T_{-1} = \frac{F_{-1}}{|\widetilde{\mathbf{U}}|}, \quad T_0 = \frac{F_0}{|\widetilde{\mathbf{U}}|}, \quad T_1 = \frac{F_1}{|\widetilde{\mathbf{U}}|}, \tag{6.40}$$

where

$$F_{-1} = \frac{\Omega^2}{K_1 K_{-1}}\tilde{V}_1\tilde{V}_{-2} - \left(1+\frac{\Omega}{K_1}\tilde{V}_0\right)\frac{\Omega}{K_{-1}}\tilde{V}_{-1}, \tag{6.41}$$

$$F_0 = \left(1+\frac{\Omega}{K_{-1}}\tilde{V}_0\right)\left(1+\frac{\Omega}{K_1}\tilde{V}_0\right) - \frac{\Omega^2}{K_1 K_{-1}}\tilde{V}_2\tilde{V}_{-2}, \tag{6.42}$$

$$F_1 = \frac{\Omega^2}{K_1 K_{-1}}\tilde{V}_{-1}\tilde{V}_2 - \left(1+\frac{\Omega}{K_{-1}}\tilde{V}_0\right)\frac{\Omega}{K_1}\tilde{V}_1, \tag{6.43}$$

$$\tag{6.44}$$

and the determinant of Eq. (6.39) is

$$|\widetilde{\mathbf{U}}| = \left(1+\frac{\Omega}{K_0}\tilde{V}_0\right)F_0 + \frac{\Omega}{K_0}\tilde{V}_1F_{-1} + \frac{\Omega}{K_0}\tilde{V}_{-1}F_1. \tag{6.45}$$

For $Q = 0$, the approximate transmission coefficients obtained in Eq. (6.40),

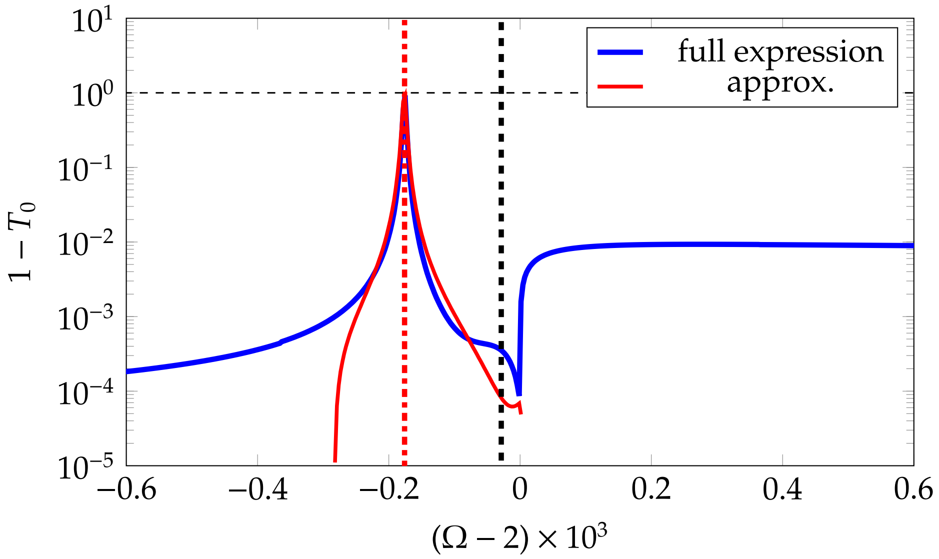

Figure 6.11: Approximation of transmission (red solid line) using Eq. (6.57) showing consistency with TE peak for $Q = 0$ and $\Delta = 0$. Red and black dashed lines indicate the real frequencies of TE mode obtained using Eq. (6.54) and Eq. (6.58), respectively.

can be further simplified by using the facts that $K_0 = \Omega$ and $K_{-1} = K_1 = \sqrt{\Omega^2 - G_1^2}$,

$$F_1 = F_{-1} = -\frac{\Omega\tilde{V}_1}{K_1}\,\mathcal{D}(\Omega) \tag{6.46}$$

$$F_0 = \mathcal{D}(\Omega)\,\mathcal{D}_2(\Omega) \tag{6.47}$$

$$\left|\widetilde{\mathbf{U}}\right| = \mathcal{D}(\Omega)\,\mathcal{B}(\Omega) \tag{6.48}$$

where

$$\mathcal{D}(\Omega) = 1 + \frac{\Omega}{K_1}\left(\tilde{V}_0 - \tilde{V}_2\right), \tag{6.49}$$

$$\mathcal{D}_2(\Omega) = 1 + \frac{\Omega}{K_1}\left(\tilde{V}_0 + \tilde{V}_2\right), \tag{6.50}$$

and

$$\mathcal{B}(\Omega) = 1 + \tilde{V}_0 + \frac{\Omega}{K_1}\left[\tilde{V}_0 + \tilde{V}_2 + \tilde{V}_0\left(\tilde{V}_0 + \tilde{V}_2\right) - 2\tilde{V}_1^2\right]. \tag{6.51}$$

We have made use of the fact that, without loss of generality, the Fourier coefficients of the grating profile function $\Lambda(x)$ are real $V_n \in \mathbb{R}$ if $\Lambda(x)$ is an even function of x, so that $\tilde{V}_n = \tilde{V}_{-n}$. The transmission coefficients in Eq. (6.40) thus reduce for $Q = 0$ to

$$T_0(\Omega, Q = 0) = \frac{\mathcal{D}_2(\Omega)}{\mathcal{B}(\Omega)}, \tag{6.52}$$

$$T_1(\Omega, Q = 0) = T_{-1}(\Omega, Q = 0) = -\frac{\Omega}{K_1}\frac{\tilde{V}_1}{\mathcal{B}(\Omega)}. \tag{6.53}$$

The TE mode peak in Fig. 6.11 (blue solid line) using the full expression of T_0 in Eq. (6.35) with $\mathbb{S}$ truncated up to 21 diffraction orders, occurs at a frequency Ω_b which is a zero of $\mathcal{B}$,

$$\mathcal{B}(\Omega = \Omega_b) = 0, \tag{6.54}$$

giving the equation,

$$\frac{\Omega_b}{G_1} = \frac{1 + \tilde{V}_0}{\sqrt{(1 + \tilde{V}_0)^2 - R^2}}, \tag{6.55}$$

where

$$R = (1 + \tilde{V}_0)(\tilde{V}_0 + \tilde{V}_2) - \tilde{V}_1^2. \tag{6.56}$$

The numerical value of $\mathrm{Re}[\Omega_b]$ for the case shown in Fig. 6.11 (red dashed line) can be obtained by solving Eq. (6.55) using a fixed-point iteration method and is shown in Fig. 6.11 by red dashed vertical line. By Taylor expanding $\mathcal{D}_2(\Omega)$, and $\mathcal{B}(\Omega)$ around its zero at Ω_b,

$$T_0(\Omega) \approx \frac{\mathcal{D}_2(\Omega_b) + (\Omega - \Omega_b)\mathcal{D}_2'(\Omega_b)}{(\Omega - \Omega_b)\mathcal{B}'(\Omega_b)} \tag{6.57}$$

we find the approximation for T_0 shown in Fig. 6.11 (red solid line). The approximation indeed matches scattering matrix calculation near the TE mode peak at Ω_b.

Although, away from Ω_b the Taylor expansions in Eq. (6.57) match poorly with the transmission spectrum, as the numerator becomes larger than the denominator, giving $T_0 > 1$.

In a periodic structure there are expected to be two SPP modes due to band folding, and it is possible that a frequency gap exists in between. Indeed T_0 at $Q = 0$ features only one mode as can be seen in Fig. 6.11. The mode missing in this transmission spectrum is dark which is mathematically evident from the cancellation of $\mathcal{D}(\Omega)$ in Eq. (6.52). The frequency of the dark TE mode $\mathrm{Re}[\Omega_d]$ is obtained by solving,

$$\mathcal{D}(\Omega = \Omega_d) = 0 \implies \frac{\Omega_d}{G_1} = \frac{1}{\sqrt{1 - (\tilde{V}_0 - \tilde{V}_2)^2}}, \tag{6.58}$$

using a fixed-point iteration method, shown in Fig. 6.11 (black dashed line). This dark mode is getting excited at $Q \neq 0$ as can be seen from Fig. 6.4(a).

6.6 Conclusions

In summary, we have shown that the complex frequency TE modes in a graphene grating can be excited. Specifically a significant reduction in the zeroth-order transmission is observed near the interband transition frequency of graphene. This significant reduction can be explained as the reflection of energy of incoming beam. This redistribution is due to the TE mode as we demonstrate by our analysis. In addition, we have shown that we can tune the frequency and in-plane wavenumber for dip in transmission for $\Delta = 0$ by controlling the graphene chemical potential and grating period respectively.

CHAPTER 7

Conclusions and Discussions

The aim of my PhD project was to understand and explore features of surface plasmon polariton (SPP) modes that can be found in graphene due to its unique optical properties, but cannot be found in Drude metals. In Ch. 2 we began by setting the mathematical foundation of the project, namely laying out the Maxwell's equations and their application to obtaining electromagnetic solutions for conducting surfaces. To make discussions and calculations easier the solutions for an interface could be mathematically categorised into two linearly independent polarisations, namely the transverse magnetic (TM) and transverse electric (TE). We highlighted that the conductivity (or permittivity) of plasmonic material is the connection between the electromagnetic solution and the electronic charge carrier current, presenting the relevant constitutive equations. We also set a template for presenting results in latter chapters by considering examples with dielectrics and Drude metal. The key result in a plasmonic system such as a semi-infinite Drude metal is a square-root like dispersion of the TM mode frequency for small wavenumbers and an upper asymptotic frequency bound given by the plasma frequency.

We then moved on to the calculation of SPP modes in thin homogeneous conductor surfaces in Ch. 3, with later application to homogeneous graphene in mind. The TM SPP dispersion for thick Drude metal has two branches corresponding to field solutions that are symmetric and anti-symmetric across the profile of the thick metal slab. For infinitesimally thin conducting surfaces one must realise the distinction between surface conductivity and bulk conductivity. The dispersion relation of TM SPPs in infinitesimally thin Drude conducting sheet with a delta-like conductivity reveals very similar features except only the solutions with anti-symmetric *H*-field survive. TE modes in the same structure have a purely imaginary frequency solutions, so that the electromagnetic fields do not oscillate with time but simply monotonously decay in intensity with time.

To move to graphene plasmonics we needed to establish a valid formula for the conductivity, which as mentioned before is the link between electron motion and electromagnetic fields, and is characteristic to plasmonic materials. The electronic structure of graphene in the tight-binding approximation reveals a Dirac cone at wavenumber *K*-point where the Fermi level lies. The electronic dispersion is linear near this point and thus we may be able to obtain the conductivity for small but non-zero chemical potential. In quantum mechanic theory the Kubo formula can be used to find conductivity from the system Hamiltonian, resulting in two parts of the conductivity related to intraband and interband electronic transitions in the electronic band structure of graphene. This splitting of conductivity into two parts is important in order to understand the properties of the SPPs in graphene as they are adversarial and each dominates the other in different frequency ranges. We identified that $\mu\beta$ is a quotient of the parameters chemical potential and temperature, altering the conductivity spectrum, and in turn the dispersion of SPPs.

We have presented the results for SPPs in graphene in Ch. 5 employing the conductivity formula obtained in the former chapter. The TM polarisation finds the SPP dispersion to be very similar to that of Drude metals, where the asymptote given by Drude model's plasma frequency has been replaced by one given by the chemical potential of graphene. The results are not qualitatively different from Drude metals because the interband features of graphene conductivity, not present in Drude metal, do not occur at frequency range of mode which has upper asymptotic bound. In the TE polarisation, however, we clearly find features from the whole of the conductivity spectrum in the mode dispersion. A higher tunability of graphene plasmons can be achieved by considering a periodic structure of graphene strips, where the period of the profile controls the wavenumber, and chemical potential controls the frequency of the desired feature in conductivity spectrum for TE mode. We have used the scattering matrix formalism to calculate transmission of TE polarised light through the graphene grating, showing enhanced peak of SPP resonance. We further calculated the resonance frequency and analytical approximation of zero order transmission around this frequency by using a Taylor expansion of a factor of the determinant of the scattering matrix truncated to three diffraction orders. We found good agreement between the approximation and the scattering matrix calculation of both the resonant frequency and the transmission spectrum.

There are several avenues of further exploration for the work presented in this thesis. Using a more accurate model of conductivity by including photon wavenumber dependence can improve the accuracy of calculation of TE mode dispersion in graphene. More intraband and interband transitions will be accessible with differing electronic wavenumbers of charge carriers in the graphene. We can speculate that as a result the conductivity might increase in magnitude, reducing the frequency of the surface plasmon dispersion and moving away from light line. An increased difference between dispersion frequency and light line frequency means further normal confinement as out-of-plane wavenumber decays faster. In Ch. 4, we presented a derivation, adapted from existing literature (see references in chapter), of the conductivity response in the long-wavelength limit, meaning that the conductivity formula that was used to calculate SPP dispersion assumed that the photons causing electronic band transitions have much smaller momentum than the electrons in graphene. At finite nonzero temperatures this does not affect the quality of the conductivity spectrum as it is smeared with respect to frequency. However, at near zero temperatures, that is $\mu\beta \to \infty$, when features in the conductivity spectrum are sharp, electronic transitions that change electronic momenta could be of importance when calculating for SPPs in graphene.

Periodic structure with two-dimensional periodicity is yet to be considered for TE mode in graphene. Although we have investigated SPPs in periodic graphene with one-dimensional periodicity, possibilities of structures increase with two-dimensional periodicity. For example, two-dimensional crystals of planar graphene, one with holes arranged in a triangular lattice, and another with graphene square antidot square array are two possible structures. This could increase the parameters of the structure, providing further flexibility in tuning TE mode in graphene.

The lack of confinement of TE mode in graphene can actually be used for enhanced sensitivity of TE mode to the material surrounding graphene. As is evident in Fig. 5.7(c)(d), $|\mathrm{Im}[K]|$ is small for TE mode in graphene, compared to TM, for frequencies away from intraband pole. TE mode is therefore less confined than TM SPPs in graphene. Although this may seem a disadvantage at first sight, TE mode, due to lack of confinement, is also more sensitive to change in permittivity [52] being more applicable for sensing application.

APPENDIX A

TM SPP dispersion relation of metal slab

A.1 Dispersion relation

We provide here a derivation for the dispersion of SPP in TM polarisation of the metal slab structure as depicted in Fig. 3.1, defined by the permittivity

$$\varepsilon = \begin{cases} \varepsilon_1 & \text{for } |z| > d/2, \\ \varepsilon_2 & \text{otherwise,} \end{cases} \tag{A.1}$$

where d is the thickness of the metal slab, ε_1 is permittivity of dielectric (or vacuum), ε_2 is the permittivity of the metal, and the two dielectric-metal interfaces lie at $z = \pm d/2$. The magnetic field in the structure Fig. 3.2 can be described by

$$H_y = e^{iqx} \times \begin{cases} Ae^{ik_1 z} + Be^{-ik_1 z} & z > d/2, \\ Ce^{ik_2 z} + De^{-ik_2 z} & -d/2 < z < d/2, \\ Fe^{ik_1 z} + Ge^{-ik_1 z} & z < -d/2. \end{cases} \tag{A.2}$$

By requiring that the ansatz Eq. (A.2) vanishes for $z \to \pm\infty$, we have $A = G = 0$ simplifying the ansatz to

$$H_y = e^{iqx} \times \begin{cases} Be^{-ik_1 z} & z > d/2, \\ Ce^{ik_2 z} + De^{-ik_2 z} & -d/2 < z < d/2, \\ Fe^{ik_1 z} & z < -d/2. \end{cases} \tag{A.3}$$

The wave equation can be obtained from Eqs. (2.1) and (2.2) as

$$\left(\nabla^2 - \frac{\varepsilon_n}{c}\partial_t^2\right) H_y = 0, \tag{A.4}$$

which together with Eq. (A.3) gives the relationship between the x and z components of the wavenumber as

$$q^2 + k_n^2 = \varepsilon_n \frac{\omega^2}{c^2}, \tag{A.5}$$

where the index n represents the material (dielectric or metal).

Then, using Eqs. (A.3) and (2.2), the x-component of electric field E_x is

$$E_x = \frac{c}{\omega} e^{iqx} \times \begin{cases} \frac{k_1}{\varepsilon_1} \cdot -Be^{-ik_1 z} & z > d/2, \\ \frac{k_1}{\varepsilon_1} \cdot [Ce^{ik_2 z} - De^{-ik_2 z}] & -d/2 < z < d/2, \\ \frac{k_1}{\varepsilon_1} \cdot Fe^{ik_1 z} & z < -d/2. \end{cases} \tag{A.6}$$

The continuity of H_y from the boundary condition Eq. (2.30) across the two interfaces at $z = \pm d/2$ gives the equations

$$Be^{-ik_1 \frac{d}{2}} = Ce^{ik_2 \frac{d}{2}} + De^{-ik_2 \frac{d}{2}}, \tag{A.7}$$

$$Ce^{-ik_2 \frac{d}{2}} + De^{ik_2 \frac{d}{2}} = Fe^{-ik_1 \frac{d}{2}}, \tag{A.8}$$

and similarly the continuity of E_x from Eq. (2.29) gives

$$\frac{k_1}{\varepsilon_1}\left[-Be^{-ik_1\frac{d}{2}}\right] = \frac{k_2}{\varepsilon_2}\left[Ce^{ik_2\frac{d}{2}} - De^{-ik_2\frac{d}{2}}\right], \tag{A.9}$$

$$\frac{k_2}{\varepsilon_2}\left[Ce^{-ik_2\frac{d}{2}} - De^{ik_2\frac{d}{2}}\right] = \frac{k_1}{\varepsilon_1}\left[Fe^{-ik_1\frac{d}{2}}\right]. \tag{A.10}$$

The simultaneous equations Eqs. (A.7)–(A.10) can be written in matrix form as

$$\mathbf{P}\begin{pmatrix} B \\ C \\ D \\ F \end{pmatrix} = 0, \tag{A.11}$$

where

$$\mathbf{P} = \begin{pmatrix} e^{-\kappa_1} & -e^{\kappa_2} & -e^{-\kappa_2} & 0 \\ 0 & e^{-\kappa_2} & e^{\kappa_2} & -e^{-\kappa_1} \\ -\frac{k_1}{\varepsilon_1}e^{-\kappa_1} & -\frac{k_2}{\varepsilon_2}e^{\kappa_2} & \frac{k_2}{\varepsilon_2}e^{-\kappa_2} & 0 \\ 0 & \frac{k_2}{\varepsilon_2}e^{-\kappa_2} & -\frac{k_2}{\varepsilon_2}e^{\kappa_2} & -\frac{k_1}{\varepsilon_1}e^{-\kappa_1} \end{pmatrix}, \tag{A.12}$$

$\kappa_1 = ik_1 d/2$, and $\kappa_2 = ik_2 d/2$. To solve Eq. (A.12) for non-zero B, C, D, F we must have $|\mathbf{P}| = 0$, giving the equation

$$\left(e^{2\kappa_2} - e^{-2\kappa_2}\right)\left[\left(\frac{k_2}{\varepsilon_2}\right)^2 + \left(\frac{k_1}{\varepsilon_1}\right)^2\right] + \left(e^{2\kappa_2} + e^{-2\kappa_2}\right)\cdot 2\frac{k_1 k_2}{\varepsilon_1\varepsilon_2} = 0, \tag{A.13}$$

$$\implies \pm\, e^{2\kappa_2}\left(\frac{k_2}{\varepsilon_2} + \frac{k_1}{\varepsilon_1}\right) = \left(\frac{k_2}{\varepsilon_2} - \frac{k_1}{\varepsilon_1}\right), \tag{A.14}$$

and resulting in the dispersion relations Eqs. (3.2) and (3.3).

A.2 Charge density

By taking divergence of Eq. (2.2) and using Eq. (2.3) we find that

$$4\pi\rho = \frac{c}{-i\omega}\nabla\cdot(\nabla\times\mathbf{H}) \tag{A.15}$$

which for TM polarisation for structure in Fig. 3.1 becomes

$$4\pi\rho = \frac{c}{i\omega}(\varepsilon_n \frac{\omega^2}{c^2} - 2q^2)H_y. \tag{A.16}$$

APPENDIX B

Details of graphene mode approximations

Note: the results presented in this appendix can also be found in the appendices of our paper [107].

B.1 TM SPP approximation

Here we provide the details for deriving the explicit expressions for TM SPP mode dispersion Eqs. (5.13) and (5.14). Please be reminded that the secular equation Eq. (5.9) of the mode reads

$$K\sigma + \Omega = 0. \tag{B.1}$$

As mentioned in Sec. 5.2, the real part of the frequency of the mode has an upper asymptote, so that the intraband conductivity, the first term in Eq. (5.6) is the dominating term. The pole in imaginary part of conductivity at $\Omega = 0$ arises from intraband conductivity and the dip $\Omega = 2$ arises from interband conductivity, see Fig. 5.1(a). So for no phenomenological damping $\Gamma = 0$ we may write the conductivity as approximately

$$\sigma \approx \frac{i\Omega_0}{\Omega}, \tag{B.2}$$

where

$$\Omega_0 = \alpha \frac{\ln(2 + 2\cosh \mu\beta)}{\mu\beta}. \tag{B.3}$$

Then according to the secular equation Eq. (B.1) we find the explicit solutions for Ω and K as

$$\bar{\Omega} = \sqrt{\Omega_0 \kappa},\ \bar{K} = i\kappa, \tag{B.4}$$

where

$$\kappa = \sqrt{Q^2 + \frac{\Omega_0^2}{4}} - \frac{\Omega_0}{2}, \tag{B.5}$$

and we have made use of Eq. (3.20) rewriting here as

$$\Omega^2 = K^2 + Q^2. \tag{B.6}$$

Now treating the interband conductivity in Eq. (5.6) as a correction $\Delta\sigma$ to Eq. (B.2),

$$\sigma \approx \frac{i\Omega_0}{\Omega} + \Delta\sigma, \tag{B.7}$$

results in a refinement of the frequency and wavenumber

$$\Omega = \bar{\Omega} + \Delta\Omega\, K = \bar{K} + \Delta K. \tag{B.8}$$

In particular, by multiplying Eq. (B.1) with Ω and using Eq. (B.6) we find

$$-(i\kappa + \Delta K)(i\Omega_0 + \Omega\Delta\sigma) = \Omega^2 = (i\kappa + \Delta K)^2 + Q^2, \tag{B.9}$$

and keeping in the above equation only terms linear in ΔK and $\Delta\sigma$, obtain

$$\Delta K \approx -\frac{\kappa\bar{\Omega}}{2\kappa + \Omega_0}\Delta\sigma. \tag{B.10}$$

Then, from Eq. (B.6) we find that

$$\bar{\Omega}\Delta\Omega \approx \bar{K}\Delta K, \tag{B.11}$$

giving

$$\Delta\Omega \approx -i\frac{\kappa^2}{2\kappa + \Omega_0}\Delta\sigma. \tag{B.12}$$

Finally, in the limit $Q \gg \Omega_0$, we get the results

$$\kappa \approx Q, \quad \bar{\Omega} \approx \sqrt{\Omega_0 Q}, \tag{B.13}$$

$$\Omega \approx \bar{\Omega} - \frac{iQ}{2}\sigma'(\bar{\Omega}), \tag{B.14}$$

$$K \approx -\frac{\bar{\Omega}}{2}\sigma'(\bar{\Omega}) + iQ, \tag{B.15}$$

where $\sigma = \sigma' + i\sigma''$ and $\sigma', \sigma'' \in \mathbb{R}$.

B.2 TE mode approximation

Here we provide details for derivation of approximations Eqs. (5.17) and (5.18). The secular equation for this mode Eq. (5.10) is

$$K + \Omega\sigma = 0. \tag{B.16}$$

Away from the frequencies near $\Omega = 0$, the conductivity in Eq. (5.6) is small $|\sigma| \ll 1$ due to the small factor of fine-structure constant α. Using this and Eqs. (B.6) and

(5.10) we obtain

$$\Omega \approx Q + \frac{Q}{2}\sigma^2(Q)\,, \qquad K \approx -Q\sigma(Q)\,, \tag{B.17}$$

and expressing separately in terms of real and imaginary parts

$$\Omega \approx Q + iQ\sigma'(Q)\sigma''(Q)\,, \tag{B.18}$$

$$K \approx -Q\sigma'(q) - iQ\sigma''(Q)\,. \tag{B.19}$$

Bibliography

[1] J. D. Joannopoulos, S. G. Johnson, J. N. Winn, and R. D. Meade, *Photonic crystals: molding the flow of light*, 2nd ed. (Princeton University Press, 2008).

[2] J. A. Schuller, E. S. Barnard, W. Cai, Y. C. Jun, J. S. White, and M. L. Brongersma, “Plasmonics for extreme light concentration and manipulation”, Nat. Mater. **9**, 193–204 (2010).

[3] J. C. Knight, “Photonic crystal fibres”, Nature **424**, 847–851 (2003).

[4] M. Skorobogatiy and J. Yang, *Fundamentals of photonic crystal guiding* (Cambridge university press, 2009).

[5] R. V. Nair and R. Vijaya, “Photonic crystal sensors: an overview”, Progress in Quantum Electronics **34**, 89–134 (2010).

[6] E. Yablonovitch, “Photonic crystals”, Journal of Modern Optics **41**, 173–194 (1994).

[7] H. Kosaka, T. Kawashima, A. Tomita, M. Notomi, T. Tamamura, T. Sato, and S. Kawakami, “Superprism phenomena in photonic crystals”, Phys. Rev. B **58**, R10096–R10099 (1998).

[8] X. Yang, A. Ishikawa, X. Yin, and X. Zhang, “Hybrid photonic-plasmonic crystal nanocavities”, ACS Nano **5**, PMID: 21384850, 2831–2838 (2011).

[9] C.-p. Huang, X.-g. Yin, Q.-j. Wang, H. Huang, and Y.-y. Zhu, “Long-wavelength optical properties of a plasmonic crystal”, Phys. Rev. Lett. **104**, 016402 (2010).

[10] D. Chanda, K. Shigeta, T. Truong, E. Lui, A. Mihi, M. Schulmerich, P. V. Braun, R. Bhargava, and J. A. Rogers, “Coupling of plasmonic and optical cavity modes in quasi-three-dimensional plasmonic crystals”, Nat. Commun. **2**, 479 (2011).

[11] Z. Fang and C. Z. Zhao, “Recent progress in silicon photonics: a review”, International Scholarly Research Notices **2012** (2012).

[12] H. A. Atwater, “The promise of plasmonics”, Sci. Am. **296**, 56–63 (2007).

[13] M. G. Hudedmani and B. S. Pagad, “Plasmonics: a path to replace electronics and photonics by scalable ultra-fast technology”, Advanced Journal of Graduate Research **7**, 37–44 (2019).

[14] E. Ozbay, “Plasmonics: merging photonics and electronics at nanoscale dimensions”, Science **311**, 189–193 (2006).

[15] B. J. Shastri, A. N. Tait, T. Ferreira de Lima, W. H. P. Pernice, H. Bhaskaran, C. D. Wright, and P. R. Prucnal, “Photonics for artificial intelligence and neuromorphic computing”, Nature Photonics **15**, 102–114 (2021).

[16] S. Noda, in *Comprehensive microsystems*, edited by Y. B. Gianchandani, O. Tabata, and H. Zappe (Elsevier, Oxford, 2008), pp. 101–112.

[17] E. Yablonovitch, “Inhibited spontaneous emission in solid-state physics and electronics”, Phys. Rev. Lett. **58**, 2059–2062 (1987).

[18] E. Yablonovitch, “Photonic band-gap structures”, J. Opt. Soc. Am. B **10**, 283–295 (1993).

[19] J. Pendry, “Playing tricks with light”, Science **285**, 1687–1688 (1999).

[20] E. Yablonovitch, T. J. Gmitter, and K. M. Leung, “Photonic band structure: the face-centered-cubic case employing nonspherical atoms”, Phys. Rev. Lett. **67**, 2295–2298 (1991).

[21] J. B. Pendry, “Calculating photonic band structure”, J. Phys.: Condens. Matter **8**, 1085–1108 (1996).

[22] K. M. Ho, C. T. Chan, and C. M. Soukoulis, “Existence of a photonic gap in periodic dielectric structures”, Phys. Rev. Lett. **65**, 3152–3155 (1990).

[23] M. Butt, S. Khonina, and N. Kazanskiy, “Recent advances in photonic crystal optical devices: a review”, Opt. Laser Technol. **142**, 107265 (2021).

[24] D. R. Solli, C. F. McCormick, R. Y. Chiao, and J. M. Hickmann, “Photonic crystal polarizers and polarizing beam splitters”, J. Appl. Phys. **93**, 9429–9431 (2003).

[25] E. N. Economou, “Surface plasmons in thin films”, Phys. Rev. **182**, 539–554 (1969).

[26] R. F. Oulton, V. J. Sorger, D. A. Genov, D. F. P. Pile, and X. Zhang, “A hybrid plasmonic waveguide for subwavelength confinement and long-range propagation”, Nat. Photonics **2**, 496–500 (2008).

[27] X. He, T. Ning, S. Lu, J. Zheng, J. Li, R. Li, and L. Pei, “Ultralow loss graphene-based hybrid plasmonic waveguide with deep-subwavelength confinement”, Opt. Express **26**, 10109 (2018).

[28] W. L. Barnes, A. Dereux, and T. W. Ebbesen, “Surface plasmon subwavelength optics”, Nature **424**, 824–830 (2003).

[29] T. W. Ebbesen, H. J. Lezec, H. F. Ghaemi, T. Thio, and P. A. Wolff, “Extraordinary optical transmission through sub-wavelength hole arrays”, Nature **391**, 667–669 (1998).

[30] R. Wood, “Xlii. on a remarkable case of uneven distribution of light in a diffraction grating spectrum”, Philos. Mag. **4**, 396–402 (1902).

[31] H. Raether, *Surface plasmons on smooth and rough surfaces and on gratings*, Vol. 111, Springer Tracts in Modern Physics (Springer Berlin Heidelberg, Berlin, Heidelberg, 1988).

[32] D. Barchiesi and A. Otto, “Excitations of surface plasmon polaritons by attenuated total reflection, revisited”, La Rivista del Nuovo Cimento **36**, 173–209 (2013).

[33] A. Otto, “Excitation of nonradiative surface plasma waves in silver by the method of frustrated total reflection”, Z. Phys. A **216**, 398–410 (1968).

[34] A. Krishnan, T. Thio, T. Kim, H. Lezec, T. Ebbesen, P. Wolff, J. Pendry, L. Martin-Moreno, and F. Garcia-Vidal, “Evanescently coupled resonance in surface plasmon enhanced transmission”, Opt. Commun. **200**, 1–7 (2001).

[35] T.-B. Wang, X.-W. Wen, C.-P. Yin, and H.-Z. Wang, “The transmission characteristics of surface plasmon polaritons in ring resonator”, Opt. Express **17**, 24096–24101 (2009).

[36] G. Gupta and J. Kondoh, “Tuning and sensitivity enhancement of surface plasmon resonance sensor”, Sens. Actuators B **122**, 381–388 (2007).

[37] E. Gerstner, “Nobel prize 2010: andre geim & konstantin novoselov”, Nat. Phys. **6**, 836–836 (2010).

[38] C. L. Kane, “Erasing electron mass”, Nature **438**, 168–170 (2005).

[39] D. Zhan, J. Yan, L. Lai, Z. Ni, L. Liu, and Z. Shen, “Engineering the electronic structure of graphene”, Adv. Mater. **24**, 4055–4069 (2012).

[40] L. A. Falkovsky, “Optical properties of graphene”, J. Phys. Conf. Ser. **129**, 012004 (2008).

[41] A. H. Castro Neto, F. Guinea, N. M. R. Peres, K. S. Novoselov, and A. K. Geim, “The electronic properties of graphene”, Rev. Mod. Phys. **81**, 109–162 (2009).

[42] F. J. García de Abajo, “Graphene plasmonics: challenges and opportunities”, ACS Photonics **1**, 135–152 (2014).

[43] F. Aguillon, D. C. Marinica, and A. G. Borisov, “Plasmons in graphene nanostructures with point defects and impurities”, The Journal of Physical Chemistry C **125**, 21503–21510 (2021).

[44] S. H. Lee, M. Choi, T.-T. Kim, S. Lee, M. Liu, X. Yin, H. K. Choi, S. S. Lee, C.-G. Choi, S.-Y. Choi, X. Zhang, and B. Min, “Switching terahertz waves with gate-controlled active graphene metamaterials”, Nat. Mater. **11**, 936–941 (2012).

[45] S. Bahadori-Haghighi, R. Ghayour, and A. Zarifkar, “Tunable graphene–dielectric metasurfaces for terahertz all-optical modulation”, J. Appl. Phys. **128**, 044506 (2020).

[46] Q. Bao, H. Zhang, B. Wang, Z. Ni, C. H. Y. X. Lim, Y. Wang, D. Y. Tang, and K. P. Loh, “Broadband graphene polarizer”, Nat. Photonics **5**, 411–415 (2011).

[47] Q. Bao, H. Zhang, B. Wang, Z. Ni, C. H. Y. X. Lim, Y. Wang, D. Y. Tang, and K. P. Loh, “Broadband graphene polarizer”, Nat. Photon. **5**, 411–415 (2011).

[48] J. T. Kim and S.-Y. Choi, “Graphene-based plasmonic waveguides for photonic integrated circuits”, Opt. Express **19**, 24557 (2011).

[49] Y. Gutiérrez, A. S. Brown, F. Moreno, and M. Losurdo, “Plasmonics beyond noble metals: exploiting phase and compositional changes for manipulating plasmonic performance”, J. Appl. Phys. **128**, 080901 (2020).

[50] S. A. Mikhailov and K. Ziegler, “New electromagnetic mode in graphene”, Phys. Rev. Lett. **99**, 016803 (2007).

[51] C. H. Gan, H. S. Chu, and E. P. Li, “Synthesis of highly confined surface plasmon modes with doped graphene sheets in the midinfrared and terahertz frequencies”, Phys. Rev. B **85**, 125431 (2012).

[52] O. Kotov, M. Kol’chenko, and Y. E. Lozovik, “Ultrahigh refractive index sensitivity of te-polarized electromagnetic waves in graphene at the interface between two dielectric media”, Opt. Express **21**, 13533–13546 (2013).

[53] D. R. Mason, S. G. Menabde, and N. Park, “Unusual otto excitation dynamics and enhanced coupling of light to te plasmons in graphene”, Opt. Express **22**, 847–858 (2014).

[54] I. Degli-Eredi, J. E. Sipe, and N. Vermeulen, “Te-polarized graphene modes sustained by photonic crystal structures”, Opt. Lett. **40**, 2076–2079 (2015).

[55] S. G. Menabde, D. R. Mason, E. E. Kornev, C. Lee, and N. Park, “Direct optical probing of transverse electric mode in graphene”, Scientific Reports **6**, 21523 (2016).

[56] F. Jabbarzadeh and A. Habibzadeh-Sharif, “Double v-groove dielectric loaded plasmonic waveguide for sensing applications”, J. Opt. Soc. Am. B **36**, 690–696 (2019).

[57] E. N. Economou, “Surface plasmons in thin films”, Phys. Rev. **182**, 539–554 (1969).

[58] X. Luo, T. Qiu, W. Lu, and Z. Ni, “Plasmons in graphene: recent progress and applications”, Mater. Sci. Eng. R **74**, 351–376 (2013).

[59] Y. Li, Z. Li, C. Chi, H. Shan, L. Zheng, and Z. Fang, “Plasmonics of 2d nanomaterials: properties and applications”, Adv. Sci. **4**, 1600430 (2017).

[60] D. J. Griffiths, *Introduction to electrodynamics*, 4th ed. (Cambridge University Press, 2017).

[61] J. D. Jackson, *Classical electrodynamics*, 3rd edition (John Wiley & Sons, New York, 1998), 832 pp.

[62] M. Mitolo and R. Araneo, “A brief history of electromagnetism [history]”, IEEE Ind. Appl. Mag. **25**, 7–11 (2019).

[63] E. Gibney, "Quantum cloud simulates magnetic monopole", Nature, 14612 (2014).

[64] P. A. M. Dirac, "Quantised singularities in the electromagnetic field," Proceedings of the Royal Society of London. Series A, Containing Papers of a Mathematical and Physical Character **133**, 60–72 (1931).

[65] H. Bruus and K. Flensberg, *Many-body Quantum Theory in Condensed Matter Physics* (Oxford University Press, 2004).

[66] S. A. Maier, *Plasmonics: fundamentals and applications*, 2007 edition (Springer, New York, 2007).

[67] S. J. Colley, *Vector calculus*, 4th ed. (Pearson, 2012).

[68] S. C. Gupta, "Delta function", IEEE Transactions on Education **E-7**, 16–22 (1964).

[69] K. Lu, "The future of metals", Science **328**, 319–320 (2010).

[70] R. Wilson, "The use of gold nanoparticles in diagnostics and detection", Chem. Soc. Rev. **37**, 2028–2045 (2008).

[71] P. Drude, "Zur elektronentheorie der metalle", Annalen der Physik **306**, 566–613 (1900).

[72] N. Ashcroft and N. Mermin, *Solid state physics*, New edition edition (Brooks Cole, New York, 1976), 848 pp.

[73] R. L. M. Gieseking, "Plasmons: untangling the classical, experimental, and quantum mechanical definitions", Mater. Horiz. **9**, 25–42 (2022).

[74] M. G. Blaber, M. D. Arnold, and M. J. Ford, "Search for the ideal plasmonic nanoshell: the effects of surface scattering and alternatives to gold and silver", J. Phys. Chem. C **113**, 3041–3045 (2009).

[75] J. J. Burke, G. I. Stegeman, and T. Tamir, "Surface-polariton-like waves guided by thin, lossy metal films", Phys. Rev. B **33**, 5186–5201 (1986).

[76] P. Berini, "Long-range surface plasmon polaritons", Adv. Opt. Photon. **1**, 484–588 (2009).

[77] R. Zia, J. A. Schuller, A. Chandran, and M. L. Brongersma, "Plasmonics: the next chip-scale technology", Mater. Today **9**, 20–27 (2006).

[78] P. Berini, "Plasmon-polariton waves guided by thin lossy metal films of finite width: bound modes of symmetric structures", Phys. Rev. B **61**, 10484–10503 (2000).

[79] A. V. Zayats and I. I. Smolyaninov, "Near-field photonics: surface plasmon polaritons and localized surface plasmons", J. Opt. A: Pure Appl. Opt. **5**, S16 (2003).

[80] J. A. Dionne, L. A. Sweatlock, H. A. Atwater, and A. Polman, "Planar metal plasmon waveguides: frequency-dependent dispersion, propagation, localization, and loss beyond the free electron model", Phys. Rev. B **72**, 075405 (2005).

[81] Z. Han and S. I. Bozhevolnyi, "Radiation guiding with surface plasmon polaritons", Rep. Prog. Phys. **76**, 016402 (2012).

[82] S. I. Bozhevolnyi and T. Søndergaard, "General properties of slow-plasmon resonant nanostructures: nano-antennas and resonators", Opt. Express **15**, 10869–10877 (2007).

[83] P. Kowalczyk, "On root finding algorithms for complex functions with branch cuts", J. Comput. Appl. Math. **314**, 1–9 (2017).

[84] B. Kelly, *Physics of graphite* (Springer Netherlands, 1981).

[85] L. J. Armitage, M. B. Doost, W. Langbein, and E. A. Muljarov, "Resonant-state expansion applied to planar waveguides", Phys. Rev. A **89**, 053832 (2014).

[86] S. Neale and E. A. Muljarov, "Resonant-state expansion for planar photonic crystal structures", Phys. Rev. B **101**, 155128 (2020).

[87] L. A. Falkovsky, "Optical properties of graphene and IV–VI semiconductors", **51**, 887–897 (2008).

[88] K. Ziegler, "Minimal conductivity of graphene: nonuniversal values from the kubo formula", Phys. Rev. B **75**, 233407 (2007).

[89] H. Ehrenreich and M. H. Cohen, "Self-consistent field approach to the many-electron problem", Phys. Rev. **115**, 786–790 (1959).

[90] R. Kubo, "A general expression for the conductivity tensor", Canadian Journal of Physics **34**, 1274–1277 (1956).

[91] R. Kubo, "Statistical-mechanical theory of irreversible processes. i. general theory and simple applications to magnetic and conduction problems", J. Phys. Soc. Jpn. **12**, 570–586 (1957).

[92] R. Kubo, "The fluctuation-dissipation theorem", Reports on Progress in Physics **29**, 255 (1966).

[93] D. K. Ferry, "The kubo formula and linear response", in *Quantum transport in semiconductors*, edited by D. K. Ferry and C. Jacoboni (Springer US, Boston, MA, 1992), pp. 17–36.

[94] G. D. Mahan, *Many-Particle Physics*, Third Ed. (Kluwer Academic / Plenum Publishers, 2000).

[95] F. Jabbarzadeh, M. Heydari, and A. Habibzadeh-Sharif, "A comparative analysis of the accuracy of kubo formulations for graphene plasmonics", Mater. Res. Express **6**, 086209 (2019).

[96] K. Ziegler, A. Hill, and A. Sinner, "Electronic transport and optical properties of graphene", in *Graphene optoelectronics* (John Wiley & Sons, Ltd, 2014) Chap. 1, pp. 1–16.

[97] K. Ziegler, "Robust transport properties in graphene", Phys. Rev. Lett. **97**, 266802 (2006).

[98] T. Zhu, M. Antezza, and J.-S. Wang, "Dynamical polarizability of graphene with spatial dispersion", Phys. Rev. B **103**, 125421 (2021).

[99] N. M. R. Peres, F. Guinea, and A. H. Castro Neto, “Electronic properties of disordered two-dimensional carbon”, Phys. Rev. B **73**, 125411 (2006).

[100] M. I. Katsnelson, “The electronic structure of ideal graphene”, in *The physics of graphene*, 2nd ed. (Cambridge University Press, 2020).

[101] B.-S. Lu, “The casimir effect in topological matter”, Universe **7**, 237 (2021).

[102] D. R. Cooper, B. D’Anjou, N. Ghattamaneni, B. Harack, M. Hilke, A. Horth, N. Majlis, M. Massicotte, L. Vandsburger, E. Whiteway, and V. Yu, “Experimental review of graphene”, ISRN Cond. Matt. Phys. **2012**, 501686 (2012).

[103] D. W. Boukhvalov, M. I. Katsnelson, and A. I. Lichtenstein, “Hydrogen on graphene: electronic structure, total energy, structural distortions and magnetism from first-principles calculations”, Phys. Rev. B **77**, 035427 (2008).

[104] L. A. Falkovsky and A. A. Varlamov, “Space-time dispersion of graphene conductivity”, Eur. Phys. J. B **56**, 281–284 (2007).

[105] L. Susskind and A. Friedman, *Quantum mechanics: the theoretical minimum* (Penguin Books, 2015).

[106] Z. Fang, Y. Wang, Z. Liu, A. Schlather, P. M. Ajayan, F. H. L. Koppens, P. Nordlander, and N. J. Halas, “Plasmon-induced doping of graphene”, ACS Nano **6**, 10222–10228 (2012).

[107] Z. Ahmad, E. A. Muljarov, and S. S. Oh, “Extended frequency range of transverse-electric surface plasmon polaritons in graphene”, Phys. Rev. B **104**, 085426 (2021).

[108] S. Fallah, K. Rouhi, and A. Abdolali, “Optimized chemical potential graphene-based coding metasurface approach for dynamic manipulation of terahertz wavefront”, J. Phys. D: Appl. Phys. **53**, 085102 (2019).

[109] T. Gu, N. Petrone, J. F. McMillan, A. van der Zande, M. Yu, G. Q. Lo, D. L. Kwong, J. Hone, and C. W. Wong, “Regenerative oscillation and four-wave mixing in graphene optoelectronics”, Nature Photonics **6**, 554–559 (2012).

[110] R. R. Nair, P. Blake, A. N. Grigorenko, K. S. Novoselov, T. J. Booth, T. Stauber, N. M. R. Peres, and A. K. Geim, “Fine structure constant defines visual transparency of graphene”, Science **320**, 1308–1308 (2008).

[111] X. Y. He, J. Tao, and B. Meng, “Analysis of graphene te surface plasmons in the terahertz regime”, Nanotechnology **24**, 345203 (2013).

[112] D. A. Kuzmin, I. V. Bychkov, V. G. Shavrov, and V. V. Temnov, “Plasmonics of magnetic and topological graphene-based nanostructures”, Nanophotonics **7**, 597–611 (2018).

[113] D. Jin, T. Christensen, M. Soljačić, N. X. Fang, L. Lu, and X. Zhang, “Infrared topological plasmons in graphene”, Phys. Rev. Lett. **118**, 245301 (2017).

[114] T. M. Slipchenko, J.-M. Poumirol, A. B. Kuzmenko, A. Y. Nikitin, and L. Martín-Moreno, “Interband plasmon polaritons in magnetized charge-neutral graphene”, Commun. Phys. **4**, 110 (2021).

[115] M. Taillefumier, V. K. Dugaev, B. Canals, C. Lacroix, and P. Bruno, “Graphene in a periodically alternating magnetic field: an unusual quantization of the anomalous hall effect”, Phys. Rev. B **84**, 085427 (2011).

[116] L. Cui, J. Wang, and M. Sun, “Graphene plasmon for optoelectronics”, Rev. Phys. **6**, 100054 (2021).

[117] M. B. Rhouma, B. Guizal, P. Bonnet, F. Paladian, and K. Edee, “Semi-analytical model for the analysis of a magnetically biased 1d subwavelength graphene-strip-grating”, Opt. Continuum **1**, 1144–1156 (2022).

[118] L. Xiong, C. Forsythe, M. Jung, A. S. McLeod, S. S. Sunku, Y. M. Shao, G. X. Ni, A. J. Sternbach, S. Liu, J. H. Edgar, E. J. Mele, M. M. Fogler, G. Shvets, C. R. Dean, and D. N. Basov, “Photonic crystal for graphene plasmons”, Nat. Commun. **10**, 4780 (2019).

[119] N. K. Emani, D. Wang, T.-F. Chung, L. J. Prokopeva, A. V. Kildishev, V. M. Shalaev, Y. P. Chen, and A. Boltasseva, “Plasmon resonance in multilayer graphene nanoribbons”, Laser Photon. Rev. **9**, 650–655 (2015).

[120] G. Li, V. Semenenko, V. Perebeinos, and P. Q. Liu, “Multilayer graphene terahertz plasmonic structures for enhanced frequency tuning range”, ACS Photon. **6**, 3180–3185 (2019).

[121] D. Rodrigo, A. Tittl, O. Limaj, F. J. G. de Abajo, V. Pruneri, and H. Altug, “Double-layer graphene for enhanced tunable infrared plasmonics”, Light. Sci. Appl. **6**, e16277 (2017).

[122] H. Yan, X. Li, B. Chandra, G. Tulevski, Y. Wu, M. Freitag, W. Zhu, P. Avouris, and F. Xia, “Tunable infrared plasmonic devices using graphene/insulator stacks”, Nat. Nanotechnol. **7**, 330–334 (2012).

[123] M.-D. He, G. Zhang, J.-Q. Liu, J.-B. Li, X.-J. Wang, Z.-R. Huang, L. Wang, and X. Chen, “Plasmon resonances in a stacked pair of graphene ribbon arrays with a lateral displacement”, Opt. Express **22**, 6680 (2014).

[124] S. Gong, L. Wang, Y. Zhang, Z. Yang, X. Li, Q. Wen, Z. He, S. Liang, L. Yuan, C. Yu, Z. Feng, Z. Yang, and X. Zhang, “Ultra-extraordinary optical transmission induced by cascade coupling of surface plasmon polaritons in composite graphene–dielectric stack”, Opt. Express **28**, 30502 (2020).

[125] I. Haddouche and L. Cherbi, “Comparison of finite element and transfer matrix methods for numerical investigation of surface plasmon waveguides”, Opt. Commun. **382**, 132–137 (2017).

[126] M. Maier, D. Margetis, and M. Luskin, “Dipole excitation of surface plasmon on a conducting sheet: finite element approximation and validation”, J. Comput. Phys. **339**, 126–145 (2017).

[127] J. Jung, T. Søndergaard, and S. I. Bozhevolnyi, “Theoretical analysis of square surface plasmon-polariton waveguides for long-range polarization-independent waveguiding”, Phys. Rev. B **76**, 035434 (2007).

[128] N. Anttu and H. Q. Xu, “Scattering matrix method for optical excitation of surface plasmons in metal films with periodic arrays of subwavelength holes”, Phys. Rev. B **83**, 165431 (2011).

[129] G. M. Maksimova, E. S. Azarova, A. V. Telezhnikov, and V. A. Burdov, "Graphene superlattice with periodically modulated dirac gap", Phys. Rev. B **86**, 205422 (2012).

[130] A. Y. Nikitin, F. Guinea, and L. Martin-Moreno, "Resonant plasmonic effects in periodic graphene antidot arrays", Appl. Phys. Lett. **101**, 151119 (2012).

[131] A. A. Shcherbakov, L. Y. Pogorelskaya, and A. A. Bogdanov, "Calculation of the 1d grating scattering matrix frequency derivatives", J. Phys. Conf. Ser. **1461**, 012159 (2020).

[132] I. Yaremchuk, T. Tamulevičius, V. Fitio, I. Gražulevičiūte, Y. Bobitski, and S. Tamulevičius, "Numerical implementation of the s-matrix algorithm for modeling of relief diffraction gratings", J. Mod. Opt. **60**, 1781–1788 (2013).

[133] I. H. Baek, J. M. Hamm, K. J. Ahn, B. J. Kang, S. S. Oh, S. Bae, S. Y. Choi, B. H. Hong, D.-I. Yeom, B. Min, O. Hess, Y. U. Jeong, and F. Rotermund, "Boosting the terahertz nonlinearity of graphene by orientation disorder", 2D Mater. **4**, 025035 (2017).

[134] D. A. Bykov and L. L. Doskolovich, "Numerical methods for calculating poles of the scattering matrix with applications in grating theory", J. Lightw. Technol. **31**, 793–801 (2013).

[135] L. C. Botten, N. A. Nicorovici, R. C. McPhedran, C. M. d. Sterke, and A. A. Asatryan, "Photonic band structure calculations using scattering matrices", Phys. Rev. E **64**, 046603 (2001).

[136] S. G. Tikhodeev, A. L. Yablonskii, E. A. Muljarov, N. A. Gippius, and T. Ishihara, "Quasiguided modes and optical properties of photonic crystal slabs", Phys. Rev. B **66**, 045102 (2002).

[137] F. S. Irani, A. H. Shafaghi, M. C. Tasdelen, T. Delipinar, C. E. Kaya, G. G. Yapici, and M. K. Yapici, "Graphene as a piezoresistive material in strain sensing applications", Micromachines **13**, 119 (2022).